# Development of an Inductively Coupled Impulse Sputtering Source for Coating Deposition

Daniel Alexander Llewellyn Loch

A thesis submitted in partial fulfilment of the requirements of
Sheffield Hallam University
for the degree of
Doctor of Philosophy

July 2015

## Declaration

I hereby declare that this thesis is my own work and effort and that it has not been submitted anywhere for any award apart from that of
Doctor of Philosophy at Sheffield Hallam University.
Where other sources of information have been used, they have been acknowledged.

.....
Daniel A. L. Loch

.....
Date

## Abstract

In recent years, highly ionised pulsed plasma processes have had a great impact on improving the coating performance of various applications, such as for cutting tools and ITO coatings, allowing for a longer service life and improved defect densities. These improvements stem from the higher ionisation degree of the sputtered material in these processes and with this the possibility of controlling the flux of sputtered material, allowing the regulation of the hardness and density of coatings and the ability to sputter onto complex contoured substrates. The development of Inductively Coupled Impulse Sputtering (ICIS) is aimed at the potential of utilising the advantages of highly ionised plasma for the sputtering of ferromagnetic material. In traditional magnetron based sputter processes ferromagnetic materials would shunt the magnetic field of the magnetron, thus reducing the sputter yield and ionisation efficiency. By generating the plasma within a high power pulsed radio frequency (RF) driven coil in front of the cathode, it is possible to remove the need for a magnetron by applying a high voltage pulsed direct current to the cathode attracting argon ions from the plasma to initiate sputtering. This is the first time that ICIS technology has been deployed in a sputter coating system. To study the characteristics of ICIS, current and voltage waveforms have been measured to examine the effect of increasing RF-power. Plasma analysis has been conducted by optical emission spectroscopy to investigate the excitation mechanisms and the emission intensity. These are correlated to the set RF-power by modelling assumptions based on electron collisions. Mass spectroscopy is used to measure the plasma potential and ion energy distribution function. Pure copper, titanium and nickel coatings have been deposited on silicon with high aspect ratio via to measure the deposition rate and characterise the microstructure. For titanium and nickel the emission modelling results are in good agreement with the model expectations showing that electron collisions are the main excitation mechanism. The plasma potential was measured as 20 eV, this is an ideal level for good adatom mobility with reduced lattice defects. All surfaces in the via were coated, perpendicular column growth on the sidewalls indicates a predominantly ionised metal flux to the substrate and the deposition rates agree with the literature value of the sputter yield of the materials. The results of the studies show that ICIS is a viable process for the deposition of magnetic coatings with high ionisation in the plasma.

# Acknowledgements

First and foremost, I would like to express my most sincere gratitude to my Director of Studies Professor Arutiun P. Ehiasarian, for the opportunity of undertaking this research work in the National HIPIMS Technology Centre.
Your advice, guidance and patience in the lab answering all my questions have helped me immensely in becoming a better scientist. Thanks Harry!!

I would also like to thank my second supervisor Professor Papken Eh. Hovsepian for his encouragement and support.

For the technical support in making the vacuum feedthrough cover, the RF coils, SEM cross-section holders and for his help solving all other lab nags, I would like to thank Mr. Gary Robinson.

For the support and training on the new HIDEN PSM mass spectrometer and the support in the analysis of the data, I would like to thank Dr. Yolanda A. Gonzalvo.

For opening the doors to the fascinating world of highly ionised pulsed plasma processes for me in the first place, I would like to thank Dr. Ralf Bandorf and Dipl.-Phys. Holger Gerdes of the Fraunhofer IST in Braunschweig, Germany.

Anna, Tom, Sampan, Steve, Arun, Itai, Trinh, Chinh, Yash and all the other students and staff of MERI, thank you for the banter and good times in- and outside of the office; we have had a great run!

To keep things in balance, I have also been fortunate to meet many new friends at the Sheffield Hallam University Sub-Aqua Club, for the times that called for experiments in the 1-6 bar range. Thanks Matt, Dave, Jamie, Amy, Luke, Noel and Justin!

Andreas, Britta, Frank and Maik thank you for being the best friends I can imagine and the long phone conversations, it is always as if we had just met yesterday.

For the support that I have received all my life and the encouragement to follow my interests, I would like to thank my mother Marion.

Last but not least, Max we don't see each other or speak often, but I am proud to have a brother like you!

## Advanced Studies

The following conferences and workshops were attended during the studies for this thesis:

- 1st International Conference on Fundamentals and Industrial Applications of HIPIMS (HIPIMS), July 2010, Sheffield, UK
- 2nd HIPIMS Conference, June 2011, Braunschweig, Germany
- COST Workshop 2011 HIPP Processes (MP0804), June 2011, Braunschweig, Germany
- Institute of Physics Postgraduate Magnetism Workshop 2012 (IOP), April 2012, York, UK
- SVC Course 323 High Power Impulse Magnetron Sputtering, June 2012, Sheffield, UK
- 3rd HIPIMS Conference, June 2012, Sheffield, UK
- 12th International Conference on Plasma Surface Engineering (PSE), September 2012, Garmisch-Partenkirchen, Germany
- COST HIPIMS Training School 2012, December 2012, Sheffield, UK
- 4th HIPIMS Conference, June 2013, Braunschweig, Germany
- 11th Technological Plasma Workshop, December 2013, York, UK
- 57th Society of Vacuum Coaters Annual Technical Conference (SVC TechCon), May 2014, Chicago, USA
- 5th HIPIMS Conference, June 2014, Sheffield, UK
- 42nd International Conference on Metallurgical Coatings and Thin Films (ICMCTF), April 2015, San Diego, USA

# Publications

## Refereed Scientific Publications

- Loch, D A L; Ehiasarian, A P (2012). A novel sputtering technique: Inductively Coupled Impulse Sputtering (ICIS). *IOP Conf. Ser.: Mater. Sci. Eng.*, 39, 012006
- Loch, D. A. L.; Gonzalvo, Y. A.; Ehiasarian, A. P. (2015). Nickel coatings by Inductively Coupled Impulse Sputtering (ICIS). *Surface and Coatings Technology*, 267, 98 - 104
- Loch, D. A. L.; Gonzalvo, Y. A.; Ehiasarian, A. P. Plasma Analysis of Inductively Coupled Impulse Sputtering by Investigation of Cu, Ti and Ni Species. *(To be submitted to Plasma Sources Science and Technology)*

## Publications not Directly Related to this Thesis

- Erik Lewin, Daniel Loch, Alex Montagne, Arutiun P. Ehiasarian, Jörg Patscheider (2013) Comparison of Al–Si–N nanocomposite coatings deposited by HIPIMS and DC magnetron sputtering. *Surface and Coatings Technology*, 232, 680-689
- Papken Eh. Hovsepian, Arunprabhu A. Sugumaran, Yashodhan Purandare, Daniel A.L. Loch, Arutiun P. Ehiasarian (2014). Effect of the degree of high power impulse magnetron sputtering utilisation on the structure and properties of TiN films. *Thin Solid Films*, 562, 132–139

# Contents

# List of Abbreviations

| | |
|---|---|
| AC | alternating current |
| Al | aluminium |
| AR | aspect ratio |
| BNC | Bayonet Neill - Concelman |
| CCD | charge-coupled device |
| CR | collisional-radiative model |
| Cr | chromium |
| Cu | copper |
| DC | direct current |
| ECR | electron cyclotron resonance |
| EDX | energy dispersive x-ray spectroscopy |
| ETD | Everhart - Thornley detector |
| Fe | iron |
| HIPIMS | high power impulse magnetron sputtering |
| ICIS | inductively coupled impulse sputtering |
| ICP-AES | inductively coupled plasma atomic emission spectroscopy |
| ICP-MS | inductively coupled magnetron sputtering |

| | |
|---|---|
| ICP-ms | inductively coupled mass spectroscopy |
| ICP-OES | inductively coupled plasma optical emission spectroscopy |
| IEDF | ion energy distribution function |
| IGBT | insulated gate bipolar transistor |
| IMPVD | ionised metal physical vapour deposition |
| In | indium |
| IPVD | ionised physical vapour deposition |
| LTE | local thermal equilibrium |
| magMEMS | magnetic microelectromechanical systems |
| MEMS | microelectromechanical systems |
| Mo | molybdenum |
| MOKE | magneto optical Kerr-effect |
| MOSFET | metal-oxide-semiconductor field-effect transistor |
| MRAM | magnetoresistive random access memory |
| MS | Mass spectrometry |
| Ni | nickel |
| OES | optical emission spectroscopy |
| PET | polyethylene terephthalate |
| PMT | photomultiplier tube |
| PVD | physical vapour deposition |
| Py | permalloy |
| RF | radio frequency |
| RGA | residual gas analysis |
| SEM | scanning electron microscope |
| sem | continuous dynode secondary electron multiplier |
| Si | silicon |

| | |
|---|---|
| $SiO_2$ | silicon dioxide |
| TE | thermal equilibrium |
| Ti | titanium |
| TLD | Through - Lens - Detector |
| UBM | unbalanced magnetron |
| UHV | ultra high vacuum |
| V | vanadium |

# List of Figures

# List of Tables

# CHAPTER 1

## Introduction

The advances of physical vapour deposition (PVD) technology towards ionised physical vapour deposition (IPVD), where the portion of the sputtered material that is ionised is higher than the neutral species, have been quite substantial over the last two decades. From complex ionisation methods such as the auxiliary electron cyclotron resonance (ECR) discharge [1] or the secondary internal or external inductively coupled magnetron sputtering (ICP-MS) discharges [2], where the deposition systems need to be modified or redesigned to incorporate the technology, to the less complex ionisation techniques where there are no or only minimal changes required such as high power impulse magnetron sputtering (HIPIMS) [3–5]. With HIPIMS the power supply can be connected to a conventional magnetron system, as the thermal load on the target is comparable to conventional sputtering due to the low duty-cycles. The desire to reduce the size of interconnects in integrated circuits [6]

meant that metallic thin films needed to be deposited on high aspect ratio features requiring the ability to control the incoming deposition flux. Ionised atoms can be controlled by altering the bias voltage to the substrate where the increased metal ionisation is visible due to perpendicular film growth on the side walls of trenches [7]. Further improvements are densification [8] leading to increased hardness, enhanced adhesion [9] and lower deposition temperatures allowing for deposition on heat sensitive substrate materials such as polyethylene terephthalate (PET) substrates [10]. Magnetic thin films are of great interest for microelectromechanical systems (MEMS), allowing the development of magnetic actuators [11, 12] or sensors [13], recording heads or magnetoresistive random access memory (MRAM) [14–16]. For the sputtering of ferromagnetic materials by magnetron technique, adaptations need to be made as the target material would shunt the magnetic field from the target surface [17–19]. Strong magnets saturate the target material allowing the magnetic field to pass through the target material and support sputtering, or the target is designed to pass the magnetic field through holes in the target [20]. By bonding thin layers of ferromagnetic material onto copper backplates, it is possible to increase the sputtering rate [21]. The copper backplate allows the magnetic field from the magnetron to pass through to the sputter material and is machined to a thickness to allow it to be fitted into existing cathode assemblies. Below the Curie point, ferromagnetic materials loose their magnetic properties [22]. By producing alloys of ferromagnetic material with materials such as vanadium (V), chromium

(Cr), aluminium (Al), silicon (Si), titanium (Ti) or molybdenum (Mo), the Curie temperature can be reduced to temperatures below the sputtering temperature [23–25]. Drawbacks of these approaches are expensive adjustments to the design of the magnetron, short run times for thin targets and film contamination due to the undesirable alloying agents.

The aim of this work is to study an alternative approach to the sputtering of magnetic materials to incorporate the advantages of highly ionised pulse plasma generation and produce high quality magnetic coatings.

Yukimura and Ehiasarian [26] have proposed a method to produce a highly ionised pulse plasma. By applying synchronised pulsed high direct current (DC) voltage to the cathode and pulsed radio frequency (RF) power to a coil in front of the cathode to generate plasma, the E-fields that are established by the voltages applied to the cathode and coil confine electrons close to the target surface. The magnetic field induced by the current flowing through the coil acts perpendicular to the target and forces electrons onto cycloidal paths eliminating the need for a magnetron. By having a perpendicular magnetic field that is established above the target surface, it is possible to sputter from pure ferromagnetic targets, as the magnetic field cannot be shunted by the target material. A further effect is a more uniform erosion of the target, allowing for higher target utilisation and longer deposition run times. The knowledge gained by pulsed plasma processes is utilised to increase the peak power input to the plasma and increase the ionisation of the sputtered material.

The objective of this thesis is to setup the ICIS system inside a vacuum deposition system and analyse the plasma by examining the current and voltage waveforms, plasma sampling mass spectrometry and optical emission spectroscopy (OES). This will make it possible to gain an understanding of the effects of increasing RF-power on the plasma, the plasma potential and ion energy distribution function as these are not known for this process and by correlating the OES results to model calculations establish the main ionisation mechanism for this process. Coatings of copper (Cu), Ti and nickel (Ni) are produced and the microstructure and magnetic properties of the Ni films are characterised.

### Present Work

This thesis is divided into five chapters. In chapter 2, an overview of the development of plasma modelling for the different states of plasma - from thermal equilibrium to the collisional-radiative model briefly explaining the principle and theory of the models, is given. Further, the advancement of PVD from basic diode sputtering to so called ionised PVD, with the basic principles of HIPIMS and ICP-MS are discussed, as plasma effects found in these types of processes will be utilised in this thesis. A brief overview of the current state of the experimental inductively coupled impulse sputtering (ICIS) technology setup is given, to acquire an understanding of the working principle and the adaptations that are needed to use ICIS in a deposition system. Finally, the evaluation of thin film properties is discussed by describing

the historic evolution of thin film microstructure modelling. The challenges of sputtering of magnetic or ferromagnetic materials and an overview of sputtering onto high aspect ratio features, such as vias, holes and trenches are given. In chapter 3, the experimental setup inside the ultra high vacuum (UHV) deposition system, the configuration of the power supplies and pulse synchronising, as well as the internal RF-coil setup is given. Further, an overview of the utilised plasma diagnostic techniques and their working principles are shown. The next section explains how modelling calculations are applied to correlate the emission intensity to the applied RF-power and the steepness of the slope graph in a log-log graph as an effect of charge and excitation of the observed species. In the final section, the characterisation of the deposited thin films for microstructure and magnetic properties is explained. Chapter 4 contains the experimental results and discussions. In section 4.1 a detailed description of the initial ICIS setup inside the UHV system is given. For section 4.2 the current and voltage waveforms on the RF-coil, the plasma optical emission and ion energy distribution function (IEDF) are measured to analyse the influence of increasing set applied RF-power on the plasma properties for Ni, Ti and Cu sputtered by ICIS. Section 4.3 describes the effect of increasing RF-power on the microstructure at a constant pressure of 13 Pa and the effect of changing the pressure at a constant RF-power of 4000 W for Cu and Ti. Section 4.4 is dedicated to the first plasma and coating analysis of pure Ni coatings deposited by ICIS. In chapter 5 the most important conclusions are drawn and the scope for

# CHAPTER 2

# Literature Review

## 2.1 Plasma States and Modelling

Spectrography of a plasma depends on the state it possesses or that it can be described by. In this section a brief overview of models for different plasma states are given to get an understanding of why the corona and the collisional-radiative models are applied to technological plasmas for coating deposition.

### 2.1.1 Thermal Equilibrium

Plasma in thermal equilibrium (TE) can be described by its temperature, density and the concentration of its elements, where each atomic interaction is in equilibrium. This means that the production rate of ions is in balance with its re-combination rate, this is also known as *detailed balance.* As a result, a plasma in TE for a specific temperature can be described by the Boltzmann equation for excited atoms and

the Saha equation for ionised atoms. The radiation from the atomic interactions is described by Plank's radiation law. While this makes it relatively easy to describe plasma in TE due to the emission being equivalent to blackbody radiation, in this state optical spectroscopy cannot be effectively applied to analyse the composition, as the radiation is self-absorbed by the plasma [27]. This kind of plasma is denoted as optically thick.

### 2.1.2 Local Thermal Equilibrium

A commonly occurring state that is very close to TE is the local thermal equilibrium (LTE) state. Assuming the non-equilibrium plasma to be homogeneous and the electron velocities to satisfy the Maxwell distribution, it is possible to describe the plasma by a local state model [27]. The more atomic interactions that are taking place, the closer collisional processes are to *detailed balance.* Assuming that the electron temperature has a Maxwellian distribution, the glow discharge can be described by the Boltzmann formula (equation 2.1) and Saha Equations (equation 2.2) as in TE. However, the radiation originating from the inside of the plasma is emitted. As the TE requirements are not met for the radiative processes, the plasma can no longer simply be described by its temperature, density and the concentration of its elements.

$$\frac{n_i}{n} = \frac{g_i}{U(T)} exp\left(-\frac{E_i}{kT}\right) \tag{2.1}$$

$$n_e \frac{n_z}{n_{z-1}} = S_{z-1}(T) = 2\frac{U_z(T)}{U_{z-1(T)}} \frac{(2\pi m_0 kT)^{\frac{3}{2}}}{h^3} exp\left(-\frac{X_{z-1} - \delta X_{z-1}}{kT}\right) \tag{2.2}$$

For sufficiently high electron densities, electron collisions support the collisional distribution functions to become very close to the TE state. In this collision dominated state the excitation rates are in *detailed balance* with the photo absorption rates [27].

These plasmas are denoted as optically thin and optical spectrometry can be applied to examine their chemical composition.

### 2.1.3 Corona Model

For low atomic and electron densities, atom interactions are not balanced. In this state collisional excitation or de-excitation is limited and three body recombinations do not occur. The electron density in this case is so low, that atoms that have been excited will decay spontaneously and ions will recombine by photorecombination [27]. The transition from LTE to corona model has been measured to be at electron densities of 1-3 $\times$ $10^{23}$ $m^{-3}$ [28]. If these prerequisites exist, the plasma is in the so-called corona state, named after the solar corona, as this is the state that dominates the corona. This is a very simplistic model where the ground-state density, excited-state levels, electron densities, transition probabilities between excitation levels and rate coefficients need to be known experimentally or by assuming certain conditions.

### 2.1.4 Collisional-Radiative Model

In principle, the corona model is a special case of the collisional-radiative model (CR), where relaxation by collision processes has a minor role. CR models are widely used to study the distribution functions in plasmas and aid in relating these to acquired experimental data. To achieve this, the atomic interactions are described as a function of the relevant values such as the electron temperature and density [29]. An important aspect of plasma diagnostics is that it is possible to determine a factor, e.g. the electron temperature, by applying rate equations to the measured spectral intensity. However, as most plasmas can not be described by the LTE state, several suitable assumptions such as Maxwellian electron velocity distribution and exclusion of molecular species need to be made [29]. In the following sections, the most important processes and parameters that are included in CR models will be introduced. Apart from the density, the temperature and the velocity of species involved in the individual excitation or decay processes, as well as the process pressure, an important factor for determining the necessary rate coefficients are the collision cross-sections $\sigma$ of the specific species. The collision cross-section are the areas of individual atoms summed ($\sigma = \pi \cdot (A_1 + A_2)^2$), where $A_1$ and $A_2$ are the radii of the atoms. For electron-atom collisions, the size of the electron can be omitted due to the large size difference, compared to the atom. While in the following sections the principle equations are given as an interaction of electrons

with argon, these interactions can also be applied to the metal species emitted by sputtering of the target material.

### Electron Impact Excitation

Electron impact excitation occurs when an incident electron (e) transfers enough energy to an electron which is bound by an atom (Ar) to enable it to move to a higher energy level. This excited state ($Ar^*$) is unstable and the electron returns to the ground state emitting the excess energy as photons. In optical emission spectroscopy, this mechanism enables the quantitative detection of the composition of a material (ICP-MS) or heated gas/plasma (OES).

$$Ar + e \rightarrow Ar^* + e \tag{2.3}$$

The excitation mechanism can also be applied to the ionised states. When electron collision is assumed to be the main excitation process, the ground state neutral atom in equation 2.3 can be replaced by an ionised atom. This is also called two-step excitation [30].

### Electron Impact Ionisation

The most important collision type for glow discharge processes is electron impact ionisation. Hereby, an electron with sufficiently high energy (15.76 eV for Ar) collides

with a ground state atom, releasing an electron from the atom (equation 2.4).

$$Ar + e \rightarrow Ar^{+} + 2e \tag{2.4}$$

A further ionisation mechanism is the collision of excited atoms with electrons (equation 2.5). So called metastable atoms ($Ar^{*}$) have a longer lifetime than resonant transitions and cannot directly decay to the ground state as they occupy a quantum number that prohibits this, because electrons can only decay to another level according to the dipole selection rules [31].

$$Ar^{*} + e \rightarrow Ar^{+} + 2e \tag{2.5}$$

These metastable states already have a high energy level (11.55 eV for Ar). The probability of an electron impact ionisation increases as many more electrons will possess the energy needed. In the case of argon, this would be the metastable energy of 11.55 eV subtracted from the ionisation energy of 15.76 eV, resulting in a required energy of only 4.21 eV to ionise the metastable atom [32].

### Penning Ionisation

Penning ionisation describes the collisional transfer of charge from a metastable atom to a neutral atom. If the ionisation energy of the neutral atom is below that of the excited atom, the neutral atom is ionised and the excited atom returns to the

ground state with a free electron remaining as in equation 2.6

$$Me + Ar^* \rightarrow Me^+ + Ar + e \tag{2.6}$$

Where Me is the neutral metal atom, $Ar^*$ is an excited metastable argon atom, $Me^+$ is a metal ion and e is an electron. It has been shown, that with increasing RF-power on the coil the gas and metal ion density rises linearly, saturating at higher powers and pressures.

## 2.2 Physical Vapour Deposition

Processes that transform solid or liquid material into the gas phase by means of physical interactions are described as PVD. The first PVD coatings can be traced back to Sir W.R. Grove in 1852 and Prof. A. W. Wright in 1877, who were the first to report deposition by glow discharge [33]. Interestingly, these were already an early version of pulsed plasma as they had utilised an alternating current (AC) source to generate the plasma. PVD can be divided into two groups of processes, thermal evaporation and vaporising by ion bombardment (sputtering). To reduce collisions of the vaporised material with other gas atoms or molecules, a vacuum or an atmosphere with a sufficiently low working pressure is needed [34]. In the current work only the technologies related to sputtering will be discussed. For this, a short outline of the technologies that are adapted for use in ICIS or have lead to

the development of ICIS is given in the following sections.

### 2.2.1 Magnetron Sputtering

The simplest sputtering technique is conventional DC sputtering, where only two electrodes are used to generate a plasma. In between two electrodes (anode and cathode) in an inert gas atmosphere, usually argon, a plasma is ignited by applying a voltage. The applied voltage accelerates free electrons from the gas or background radiation along the created electric field lines towards the anode. The atoms of the inert gas are ionised by collisions with the accelerated electrons as described earlier in section 2.1.4.

Due to the cathode potential, the inert gas ions in the plasma are accelerated to the cathode (target) and eject secondary electrons and material atoms from the target surface on impact. The electrons diffuse to the chamber walls or recombine with the ions. The rapid drainage of the electrons reduces the probability that they ionise further inert gas atoms. This effect reduces the deposition rate and therefore is not economically viable for most applications.

To increase the deposition rate and to increase the operating pressure range, the ionisation efficiency needs to be improved [32]. This can be achieved by increasing the path an electron takes before recombination by adding a magnetic field, using of RF excitation, or using a hot filament as an additional electron source [32].

The most commonly used type of an additional magnet assembly is the planar

magnetron, first described by Chapin in 1974 [35]. The force acting on an electron is given as:

$$\vec{F} = q(\vec{E} + \vec{v} \times \vec{B}) \tag{2.7}$$

Where $q$ is the charge, $E$ the electric field, $v$ the particle velocity and $B$ is the magnetic field strength.

The radius of the electron trajectory can be determined by equating the centripetal force (equation 2.8) and the Lorenz force.

$$F = \frac{m \cdot v_{\perp}^2}{r_g} \tag{2.8}$$

$$\frac{m \cdot v_{\perp}^2}{r_g} = q(v_{\perp} \cdot B) \tag{2.9}$$

$$r_g = \frac{m \cdot v_{\perp}}{qB} \tag{2.10}$$

Where $m$ is the mass of the charged particle, $v_{\perp}$ is the vertical velocity and $r_g$ is the radius of the cycloidic path, the so called Larmor radius.

Equations 2.9 and 2.10 show the relation between the Lorentz force, the Centripetal force and the Larmor radius [36]. The effect of the Larmor radius is an increase of the distance that the electrons travel and thus the collision probability with inert gas atoms, which in turn increases the electron density.

A characteristic feature of magnetron sputtering is the erosion trench in the cathode

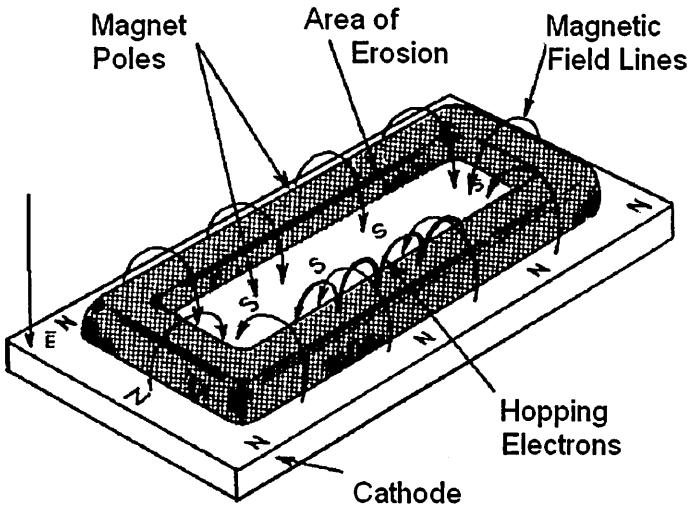


**Figure 2.1:** Planar Magnetron Schematic [32].

that indicates the area of the highest electron density and mirrors the magnet setup, the so called "racetrack", as can be seen in figure 2.1. Due to the confinement of the erosion area, the target usability is reduced and has been reported to be as low as approximately 30 % for planar magnetron sputtering.

Conventionally, magnetrons are built with magnets of equal magnetic force in the centre and in the outer parts, the so called balanced magnetron. This configuration allows the magnetic field lines to close across the target surface and as such "force" electrons and ions near to the target. While this is good to achieve a dense plasma, it reduces the ion flux from the target to the substrate. To overcome this, in 1986 Window and Savvides began to study the effects of different magnet configurations and magnet forces [37]. This work was the basis for the development of the unbalanced magnetron (UBM).

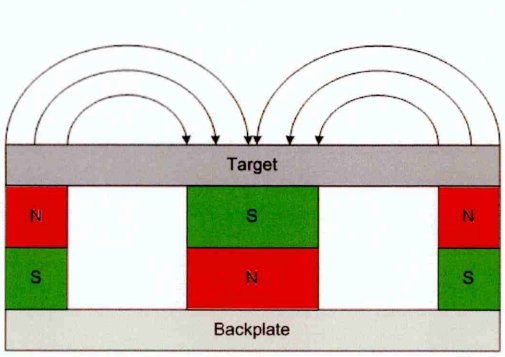


**(a)** Schematic of a balanced magnetron configuration.

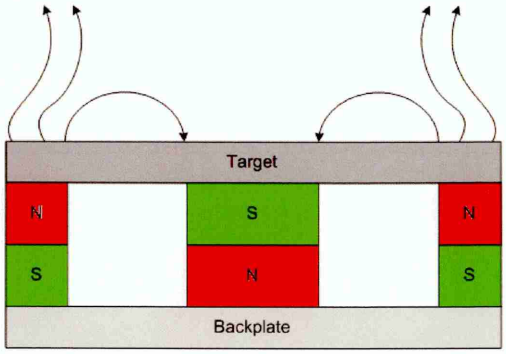


**(b)** Schematic of a type II unbalanced magnetron configuration.

**Figure 2.2:** Comparison of balanced and unbalanced magnetron configurations.

In contrast to a type I UBM setup where the centre magnets are stronger, in a type II UBM setup the magnets in the outer sides are stronger than in the centre. This causes the magnetic field lines to be extended further away from the target, as can be seen in fig. 2.2. The extended field lines enable the plasma to extend towards the substrate and enhance the ion flux on the substrate by up to an order of magnitude [37]. To raise the plasma density in UBM processes the use of multiple magnetrons with the correct opposing magnetic pole setup can be used to close the field lines across the chamber [38]. Closed field UBM systems reduce the probability of electron diffusion to the chamber walls and being lost for the ionisation process.

A further factor in the mobility of electrons and ions is the ambipolar diffusion. Due to the higher mobility of electrons there would be potential differences in the plasma, but due to their opposing charges ions and electrons cannot be separated. As electrons diffuse away a restraining electric field is induced by the slightly positive

plasma; this field is large enough to equalise the diffusion of the charged particles. This is the basis for one of the most fundamental rules of plasma: the rule that the plasma is quasi-neutral. This also shows that electrons and ions diffuse at the same rate despite their different mobilities [32].

$$j_i = j_e = \left( \frac{D_e \mu_i + D_i \mu_e}{\mu_i + \mu_e} \right) \frac{dn_e}{dx} \tag{2.11}$$

The current flow of ions and electrons is described by equation 2.11 where $D_e$ and $D_i$ are the diffusion constants for electrons and ions; $\frac{dn_e}{dx}$ is the electron density when a diffusion gradient is present; $\mu_i$ and $\mu_e$ are the mobilities and $j_i$ and $j_e$ are the diffusion rates [32]. From this it follows that the ambipolar diffusion constant $D_A$ is defined as in equation 2.12:

$$D_A = \left( \frac{D_e \mu_i + D_i \mu_e}{\mu_i + \mu_e} \right) \tag{2.12}$$

It is reasonable to assume that the value of $D_A$ would be in between the values of $D_e$ and $D_i$.

### 2.2.2 Inductively Coupled Radio Frequency Plasma Sources

Inductively coupled discharges have been studied since 1884 when J.H. Hittorf first reported a discharge inside an evacuated tube wrapped with a coil driven by a Layden jar [39, 40]. Inductively coupled RF plasma sources are being used extensively in

analytical techniques such as inductively coupled mass spectroscopy (ICP-ms) or inductively coupled plasma optical emission spectroscopy (ICP-OES), also known as inductively coupled plasma atomic emission spectroscopy (ICP-AES). In the late 1980s, with the development of planar and cylindrical coil configuration [40–42], interest grew in the plasma deposition field. ICP sputtering offers the ability to control the flux of sputtered material and opens up possibilities to influence the coating properties by changing the ion-to-neutral ratio or the ion energy of the impeding flux. Inductively coupled RF discharges utilise a secondary plasma that is generated by applying an RF source to an external or an internal immersed antenna assembly to ionise the sputtered flux. For the external configuration, a coil is wound around a dielectric chamber or a planar coil is used with a quartz window (fig. 2.3).

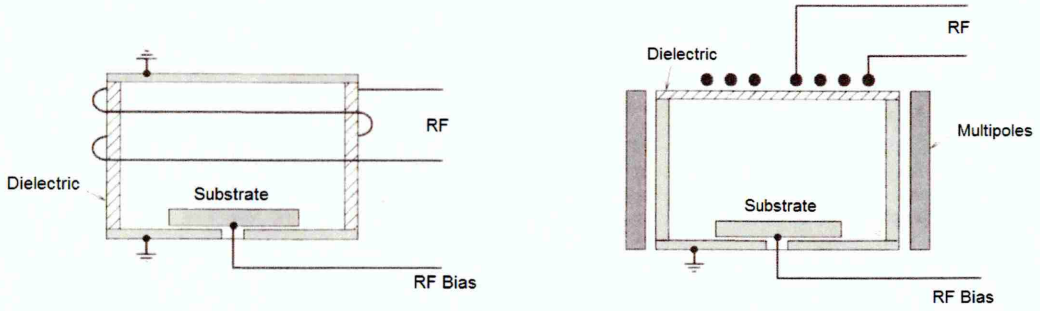


**(a)** Schematic of external cylindrical ICP coil. **(b)** Schematic of external planar ICP coil.

**Figure 2.3:** Comparison of external cylindrical and planar coil configurations [40].

For conductive material processing, this configuration is challenging as sputtered material is deposited on the dielectric which can suppress the plasma, because the coating acts as a short-cut to the inductance [41].

The principle of immersed inductor ICP-MS to achieve highly ionised metal plasmas was first published by Yamashita in 1989 [43]. In 1993 Rossnagel and Hopwood described an ICP-MS system which is usable for the semiconductor industry [44]. As can be seen in figure 2.4, an induction coil is positioned between the magnetron and substrate immersed in the plasma. Utilising the high metal ion flux with moderate ion energies allows for the deposition of high aspect-ratio features [44].

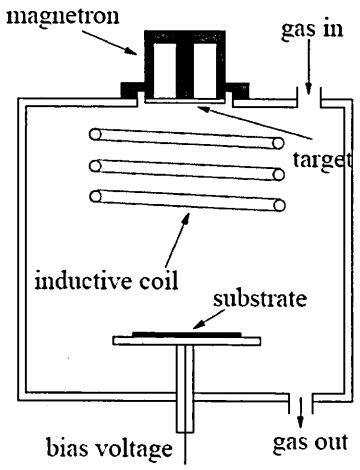


**Figure 2.4:** Schematic of an ICP-MS setup with an internal coil [45].

Inductively coupled discharges with an internal coil typically have two operation modes. The E-discharge, which is a capacitive discharge normally observed at low power settings, changing to the inductive H-discharge at higher power.
This change is also often observable by the eye, as the light emission is increased for H-mode [41, 42].

RF plasma sources are typically operated at a frequency of 13.56 MHz [32]. A

capacitive and inductive matching network is used to match the immersed antenna to the 50 Ω output of the power supply to allow the maximum RF current to flow through the winding. As described by the differential Maxwell-Faraday equation:

$$\nabla \times \vec{\mathbf{E}} = -\partial \vec{\mathbf{B}} / \partial t \tag{2.13}$$

the magnetic field $\mathbf{B}$ that is induced by the time varying RF current in the coil, creates the electric field $\mathbf{E}$, which can accelerate free electrons and create or maintain the discharge. Due to the high frequency, the lighter electrons can oscillate in the electric field and the heavier ions are not influenced and can traverse the coil area. As a result, argon ions that are ionised in the coil are accelerated to the target and sputtered target material is ionised as it passes through the dense plasma area. Typically ICP discharges are operated at 0.2-7 Pa [46]; at these pressures the main ionisation mechanism is Penning ionisation [44].

### 2.2.3 High Power Impulse Magnetron Sputtering

In DC magnetron sputtering, electron collision is the main excitation mechanism. In order to achieve a high degree of metal ionisation at low pressures, a high electron density in the range of $10^{19}$-$10^{20}$ $m^{-3}$ is necessary. The power needed to achieve this would require extensive cooling to prevent the material from melting. Additionally, with increasing power, the temperature also increases and with it the probability of arcing. Arcs cause macro-particles of the target material to deposit on the substrate,

which would make e.g. isolating coatings unusable. However, cooling is limited only by the average power and not the peak power. First reports from Khodachenko and Mozgrin [47] on HIPIMS were later described in a seminal paper by Kouznetsov et.al. in 1999 [3].

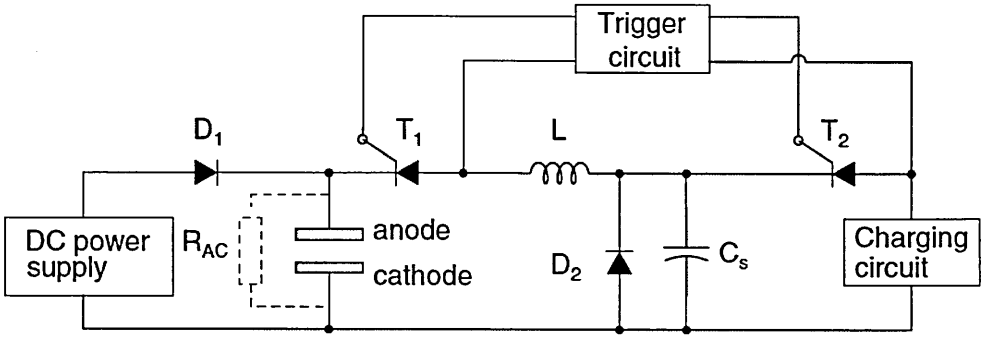


**Figure 2.5:** Schematic of an HIPIMS Power Supply according to Kouznetsov [3].

By pulsing with a low duty-cycle the power that is applied to the cathode can be kept at a level which is comparable with DC sputtering, while allowing the peak power to be increased extensively [4, 5, 48]. This enables current densities in the A $cm^{-2}$ range, while maintaining a thermal load compared to conventional sputtering [46]. As a result, the cooling system does not have to be enhanced. Depending on the size of the system, HIPIMS generators are able to supply peak powers of approximately 10 kW up to 8 MW (Trumpf Hüttinger Electronic, Poland) to achieve the necessary high electron densities. HIPIMS processes produce a dense, highly ionised, particle free plasma, which combines the advantages of arc evaporation and magnetron sputtering [9, 49].

In the scope of this work, the HIPIMS power supply will be used to bias the target

to attract Ar ions and initiate sputtering. Further detail of this will be given in Chapter 3.1.

### 2.2.4 Magnet Free RF Assisted High Power Pulsed Sputtering

RF assisted high power pulsed sputtering is an experimental setup by Yukimura and Ehiasarian [26, 50, 51], adapted for high power pulsed sputtering without a magnet assembly, from initial work by Malkin [52], which uses RF pulses to pre-ionise the gas before a current pulse is applied to the cathode. This process technology has been named ICIS.

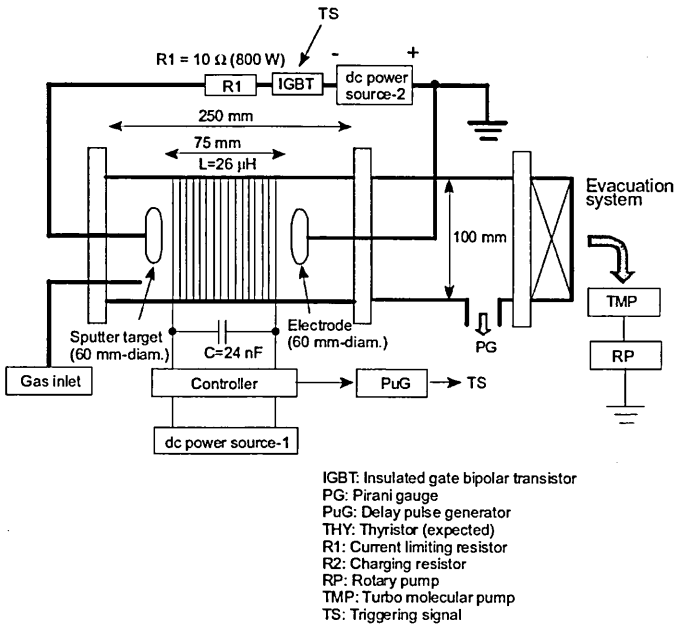


**Figure 2.6:** Schematic of an RF assisted high power pulsed sputtering setup [26].

Figure 2.6 shows the setup inside a glass chamber. The RF plasma is ignited in an argon atmosphere by applying a 200 kHz RF current and voltage signal to a wire, which is wound around the outside of the chamber forming an inductance. Two

electrodes inside the chamber are connected to a DC power supply which is pulsed by a trigger signal controlling an insulated gate bipolar transistor (IGBT). A pulse delay generator sends out the trigger signal to the IGBT to operate the cathode at various times during the RF plasma pulse. The repetition rate is the pulsing frequency of the power supplies - in this setup it was 80 Hz. It was shown that the plasma current is dependant on the cathode pulse on-time and RF plasma on-time synchronisation. If the cathode pulse is applied after the RF plasma is off, the plasma current is significantly smaller than during the cathode on-time [26]. In this thesis, we will be adapting the working principle of ICIS to work with an immersed coil assembly inside a deposition system.

## 2.3 Thin Film Properties and Models

The development of thin films is astounding! Today thin films are being used in all aspects of modern life from space exploration to the morning shave, mostly unknown to the actual end user. Originally used for decorative applications, thin films are now the centre point of technological development. This versatility is possible due to the various properties of the films that can be influenced by plasma assisted PVD technology such as film thickness, material composition, structure and density. Deposition of evaporated or sputtered material is divided into several phases, from nucleation to continuous film growth, and these interactions cause the structure of the coating to be columnar [53].

### 2.3.1 Microstructure of Thin Films

Important parameters for the description of the microstructure are the morphology and texture. Movchan and Demchishin [54] were the first to develop a model for high rate deposition of film, describing the influence of substrate temperature on the morphology. For metal coatings, they found that the ratio of the substrate temperature $T_s$ and the melting temperature $T_m$ of the sputtered material, $(\frac{T_s}{T_m})$, the homologous temperature, can be divided into 3 zones. Zone 1 (fig. 2.7) has a $\frac{T_s}{T_m}$ ratio up to 0.3 and exhibits a porous, tapered columnar structure with unclear boundaries. With increasing substrate temperature the adatom mobility increases and allows the formation of well defined columnar structures, this has been designated zone 2 and is valid for $T_s$ to be between 0.3 and 0.5 $T_m$. In zone 3 the high temperatures allow the recrystallisation with random grain bounderies [55].

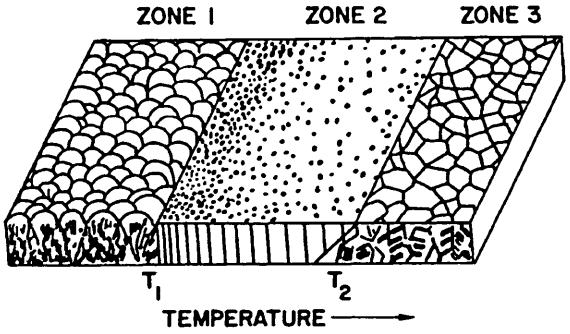


**Figure 2.7:** Structure Zone Model according to Movchan and Demchishin for evaporated films, showing the 3 zones in relation to the ratio of substrate temperature ($T_s$) vs. melting temperature of the material ($T_m$) [55].

In 1974, Thornton [56] extended the model by Movchan and Demchishin for the

sputtering process by adding the influence of argon pressure on the morphology. It was found that the same 3 zones apply to the sputter process as have been found by Movchan and Demchishin, however for low argon pressures a wide transition zone T appeared between zone 1 and 2 (fig. 2.8). With increasing Ar pressure this zone narrows. This zone is dominated by a denser, smoother film and due to the higher adatom mobility shadowing effects are reduced.

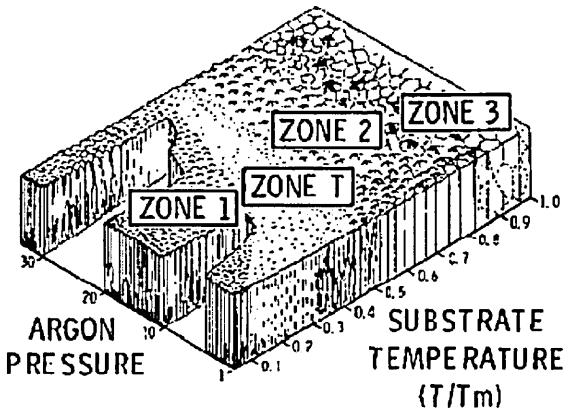


**Figure 2.8:** Structure Zone Model according to Thornton for sputtered films showing the added zone T and the influence of argon pressure [56, 57].

A further refinement of the above models was proposed by Messier et.al. [58], adding the effect of bias voltage on the structure zones. Figure 2.9 shows that for increasing bias on the substrate and with that an increasing ion energy for the bombarding ions, the transition from zone 1 to zone T starts at a lower homologous temperature. Several investigations have been conducted [9, 60, 61] that have shown that ion energies over 100 eV show lattice defects.

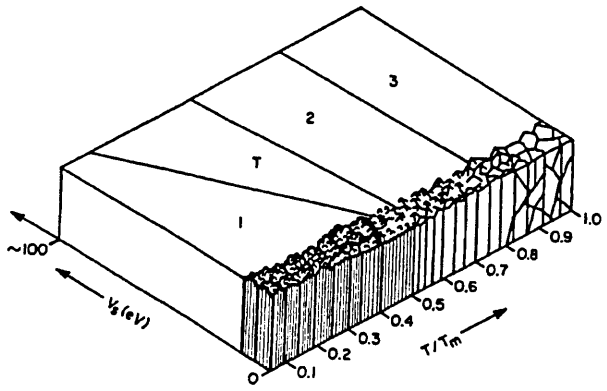


**Figure 2.9:** Structure Zone Model according to Messier for sputtered films, showing the effect of ion bombardment energy on the transition from zone 1 to zone T [58, 59].

Development of the closed-field magnetron process, where in systems with more than one magnetron the magnetic field lines of the individual magnetron join and shield the plasma from the chamber walls, the field lines suppress the ionic losses due to the recombination effects [62, 63]. This leads to an increase of the ion to neutral ratio which has been found to have an effect on the film morphology. Kelly and Arnell [64] have developed a model which refines previous models and adds the ion to neutral ratio.

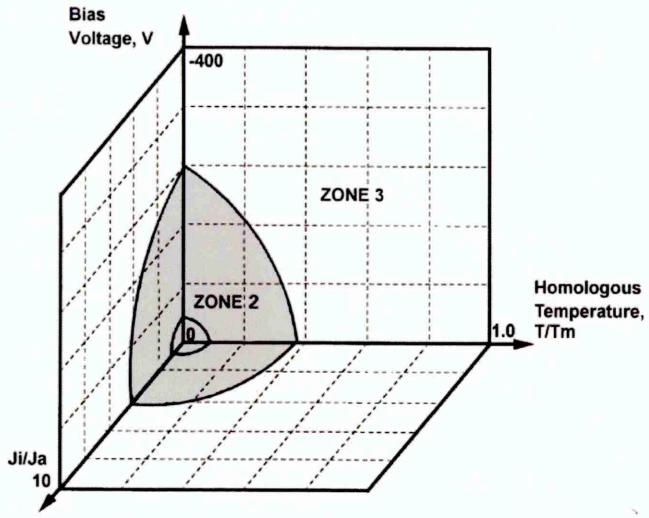


**Figure 2.10:** Structure Zone Model according to Kelly and Arnell showing the effect of the ion to neutral ratio on the morpthology [63].

This model, described by fig. 2.10, does not describe the zones in as much detail as earlier models. In order to include the now most important parameters, the homologous temperature, the substrate bias voltage and the ion to neutral ratio, the model now has 3 dimensions. Here the zone boundaries are displayed as a spherical segment indicating the boundary. Zone 0 is the lowest boundary for normal operating conditions and not the transition from zone 1 to 2 as in earlier models [63].

### 2.3.2 Thin Films of Magnetic Materials

Thin film magnetic materials are used in a variety of applications, from magnetic recording for data storage to magnetic microelectromechanical systems (magMEMS) [11, 15]. For these applications the magnetic properties of the magnetic films need

to be very precise, i.e. sensors need defined switching points to produce reliable measurements. The properties that are important are the magnetic permeability ($\mu$), loss tangent ($tan\delta$), anisotropic field ($H_a$), ferromagnetic resonance frequency ($f_0$) and the line width ($\Delta H$) [65]. In practice, the properties of the thin film differ from the bulk material. It was first shown by Neel in 1955, that the domain wall energy is not only influenced by the material, but also by the thickness of the film [66]. To understand this it is necessary to look at some of the principles of magnetisation.

There are several variables that can change the form of the magnetic field in thin films, one of these is the domain size. As described by Harsha [65], the domain size defines the size of the particle with a north and south pole. For permanent magnetic material it is estimated that the domain size is about 100 µm and the domain wall thickness e.g. of iron (Fe) is about 3 µm. The domain wall thickness describes the thickness of the barrier between two domains with different orientation. As can be seen from these numbers, with thin films in the range of a few µm, magnetic thin films only have one domain.

A feature of permanent magnets is the ability to magnetise the material in one direction with an external magnetic field. When the external field is removed the permanent magnet material will stay magnetised. To reverse the magnetisation it is necessary to apply a reversed magnetic field. Due to the complex mechanisms that take place to magnetise the domains, the magnetisation and demagnetisation curve follows a hysteresis as can be seen in 2.11.

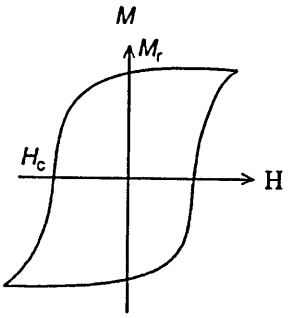


**Figure 2.11:** Hysteresis loop for magnetising and demagnetising a hard magnetic material. Here the magnetic remanence $M_r$ is large when the magnetic field is reversed and a large coercive field $H_c$ is needed to demagnetise the material [65].

To achieve a high energy density, permanent magnetic films must grow in a preferred orientation. The preferred orientation can be controlled by the energy and momentum of the sputtered material flux. One way of doing this, is to increase the pressure so that the sputtered species have many collisions before arriving at the substrate [65].

### 2.3.3 Bottom Coverage in High Aspect Ratio Structures

In conventional physical vapour deposition techniques, the neutral metal atoms are emitted from close to the bombarded surface with a mostly cosine emission profile from the surface normal. Additionally, the shape of the plasma on the target surface, e.g. racetrack, creates an uneven deposition flux to the substrate. While this is less of an issue for depositing a film on low aspect structures, it does pose a problem for high aspect ratio structures. Because of the uneven deposition, the opening of trenches and vias could be blocked leaving voids in the coating [44].

Sputtering on high aspect ratio structures plays an ever increasing role in the

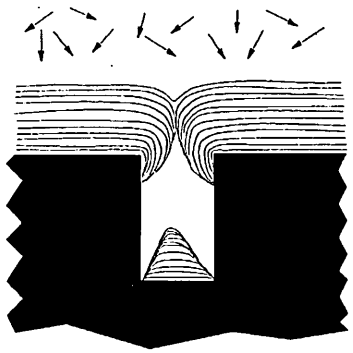

**Figure 2.12:** Void-building on high aspect ratio structures [44].

continuous effort to reduce the size of microelectronic components. For these applications it is important to prevent voids forming in the coating.

As has been shown by Holber 1993 and Rossnagel and Hopwood 1994, ionised metal physical vapour deposition (IMPVD) has proven to be the technology of choice for this [44, 67, 68].

In figure 2.12 the effect of preferential sputtering can be seen. In IPVD this can be reduced as the ionised species follow the electric field lines and by applying a bias voltage to the substrate, the energy of the bombardment flux can be modelled as such that the effect of resputtering works against the deposition rate helping to keep vias and trenches open [69, 70]. This can be seen in fig. 2.13.

The main disadvantage of this technology is the reduced deposition rate due to the many collisions that are necessary to ionise the metal vapour. One of the reasons for the reduced sputter rate at higher pressures is the diffusion of metal atoms to other surfaces than the substrate [68]. The main advantage is that with ionised metal atoms it is possible to achieve higher bombardment energy as they can be

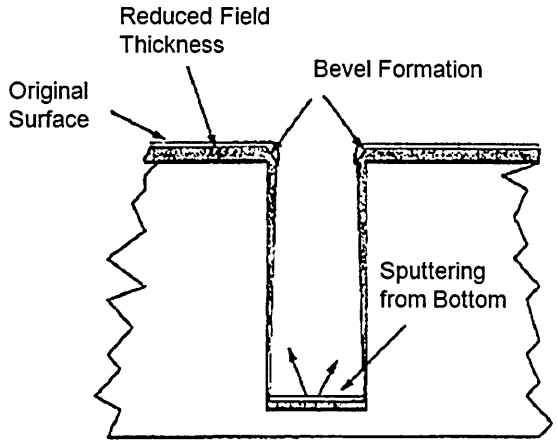


**Figure 2.13:** I-PVD deposition showing sputtering of field region by energetic ions, bevelling of corners and sputtering from the bottom of features [71].

accelerated along the electric field lines by applying a bias voltage to the substrate. This is beneficial for the densification of the column structures in the coating.

# CHAPTER 3

# Experimental & Methodology

## 3.1 Experimental Setup

### 3.1.1 K. J. Lesker UHV System

The vacuum system consists of an ultra high vacuum vessel (Kurt J. Lesker), that is evacuated by a pumping network of one rotary pump and two turbomolecular pumps to a base pressure of $< 10^{-5}$ Pa. This system enables the introduction of various plasma and deposition analytical instruments to simultaneously take measurements.

As can be seen in fig. 3.1, the assembly of the sample holder is at an angle to the cathode; due to this, the species in the plasma have to undergo a number of collisions to reach the substrate. The sample holder can rotate to coat more evenly, can be heated to modify the microstructure and can be biased to modify the impinging energy of the metal ions. In the current work, the substrate bias is at

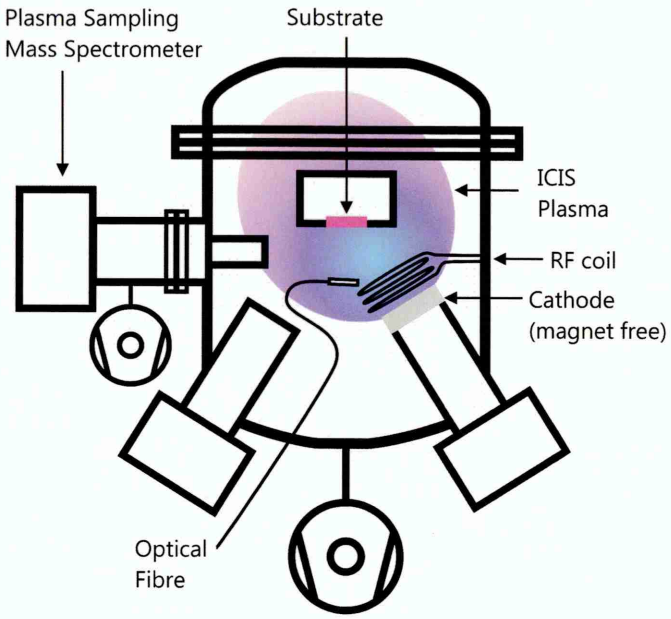


**Figure 3.1:** Schematic of the vacuum system at the HIPIMS Technology Centre with an ICIS coil assembly.

floating potential as the electrical connection to the substrate holder is isolated. The cathodes are 75 mm in diameter and outfitted with the relevant target material for sputtering. The magnet assembly has been removed from behind the ICIS cathode.

### 3.1.2 Power Supply Configuration

#### RF Power Supply

An RF power supply (Trumpf Hüttinger PFG 5000 RF) powers a copper RF-coil at 13.56 MHz, that is attached in front of the cathode and ignites the plasma. Between the power supply and the coil a matching unit prevents high currents flowing through the circuit and protects the generator. Industry standard for power supplies is an output resistance of 50 Ω. During the RF discharge the impedance of the plasma

can vary, the impedance of the ICIS discharge has been measured to be approx. 4 Ω during the pulse on-time and can reach up to 400 Ω during the pulse off-time. The matching network consisting of inductors and capacitors and is used to adapt the load in the discharge to the output impedance of the power supply [32]. The RF signal is applied in pulse mode, the maximum power is 5 kW.

#### HIPIMS Power Supply

To attract ions to the target in absence of a magnetron, the target is biased by a pulsed DC voltage. The DC voltage is provided by an HIPIMS power supply (Trumpf Hüttinger HMP 6/16). The voltage to the cathode is kept constant at 1900 V. The repetition frequency is variable to 500 Hz, the pulse is variable up to 500 µs. In 2.2.4 it was described that to achieve the highest ion currents, it is necessary to synchronise the pulses applied to the anode and cathode. The pulsing unit of the HIPIMS power supply is used to trigger a pulse generator, which can be used to delay the RF pulse to coincide with the next HIPIMS pulse.

### 3.1.3 RF-Coil Setup

The coils used as immersed RF antennae are made of solid copper rod with 2 or 7 turns. Two turn coils are 80 mm in diameter and therefore slightly larger than the cathode to utilise the whole target surface. To increase the magnetic field strength, some initial experiments were conducted with a 7-turn coil with a diameter of 50 mm. A power feedthrough consisting of two solid Cu rods allows for the coil to

be assembled and positioned in front of the target and 3-5 mm above the cathode ring. On the atmospheric side the connection to a coaxial socket is made to attach the RF power supply and matching network.

### 3.1.4 Sample Preparation

Samples were prepared by selectively fragmenting an ATDF Si Q-Cleave-E reticle coated with silicon dioxide ($SiO_2$). As the reticle features via with various aspect ratios ordered at different densities, choosing the optimal direction of cleaving allows analysis of several different feature variations.

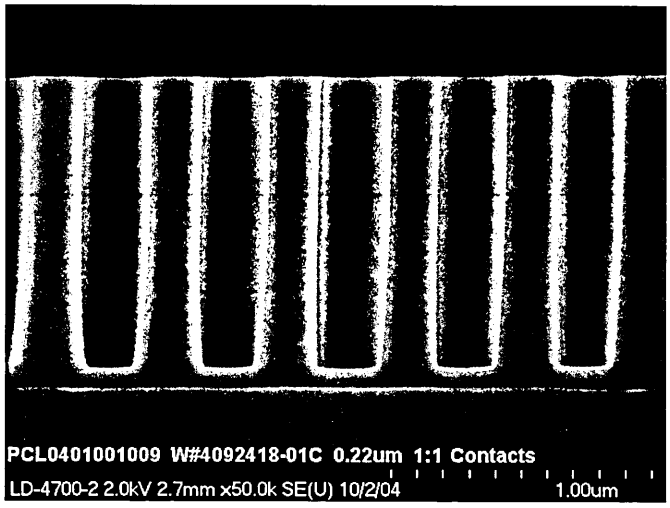


**Figure 3.2:** Cross-section of the uncoated substrate containing high aspect ratio via [72].

Figure 3.2 shows an scanning electron microscope (SEM) cross-section of the uncoated substrate. The via are cylindrical with a depth of 1 µm and widths of 160-600 nm and spacings of 1:1, 1:1.5, 1:3 and 1:6 in relation to the contact width [72].

The coated samples are cleaved by careful scratching of the silicon by diamond pen and broken over a sharp edge.

## 3.2 Plasma Characterisation Techniques

### 3.2.1 Current and Voltage Measurement

Current and voltage measurements for the RF-coil were taken at a location between the matching network and the vacuum feed-through by a Tektronix P5100 voltage probe and a Tektronix P6021 AC current probe. The current and voltage measurement for the target was taken at the HIPIMS power supply by voltage readout of the power supply and Person Current Monitor Model 110. All 4 channels were measured simultaneously by a Tektronix DPO 7054 4-channel oscilloscope. The probes were not calibrated for time response and delay times [73] and we could not obtain the absolute phase or instantaneous peak power; however, the measurements obtained were proportionally related to the actual values. With the current and voltage signals measured between the matching network of the RF power supply and the coil, it is possible to determine the current and voltage waveforms of the discharge and calculate the resistivity and charge. When increasing the power set-point for the power that is applied to the RF-coil at the power supply, the charge can be used as an indication of the linearity of the actual increase of power applied to the RF-coil. The charge ($Q$) is defined as the current ($I$) per time ($t$) that passes through the

circuit:

$$Q = I \times t \tag{3.1}$$

As in this work the applied power is pulsed, the equation needs to be adapted to:

$$Q_p = \sum_{0}^{t_{on}} I_s \times t_s \tag{3.2}$$

where $I_s$ is the current for the measurement step and $t_s$ is the step size of the oscilloscope measurement. These values need to be summed up for the duration of the pulse on-time.

The resistivity in the coil can be used as an indicator for the influence of increasing applied power on the impedance of the plasma. The resistivity can be calculated by Ohm's law; additionally, the calculation results for each measurement step are summed up resulting in:

$$R_{t_{on}} = \sum_{0}^{t_{on}} U_s/I_s \tag{3.3}$$

Where $R_{t_{on}}$ is the resistivity during the pulse on-time; $U_s$ and $I_s$ are the voltage and current for the individual oscilloscope measurement step respectively.

To gain information on the phase and impedance, measurements were conducted with an Impedans OCTIV VI probe for Ti ICIS with a pulse width of 500 µs. This

probe was also setup between the matching network and the vacuum feed through. Current, voltage, impedance, phase (represented as current in relation to voltage) and instantaneous power were measured simultaneously.

### 3.2.2 Optical Emission Spectroscopy

One of the features of plasmas is that they glow. The source of the glow are photons that are emitted when electrons from higher energy states fill up lower energy electron shells of the atom that are not completely filled [32]. To be able to fill up the empty spaces, the electrons must loose energy which they do by the emission of photons. Because the lifetime of the excited electron configuration is limited and also, for every step back to the ground state photons with a specific energy are emitted with a specific wavelength, it is possible to detect the individual species. These are excited atoms, metastable atoms and ions of various charge states [32]. The released energy can be calculated by:

$$dE = hc\lambda^{-1} \tag{3.4}$$

Where $dE$ is the released energy, $\lambda$ is the wavelength, $h$ is Plank's constant ($h = 6.626 \times 10^{-34}$) and c is the speed of light ($\mathrm{c} = 3 \times 10^{8}\ \mathrm{m\,s^{-1}}$).

For optical emission spectroscopy the Jobin-Yvon TRIAX320 system will be used. This is a Czerny-Turner type analyser. As can be seen in figure 3.3, this type of analyser consists of two focusing mirrors and a turret with the grating. When the

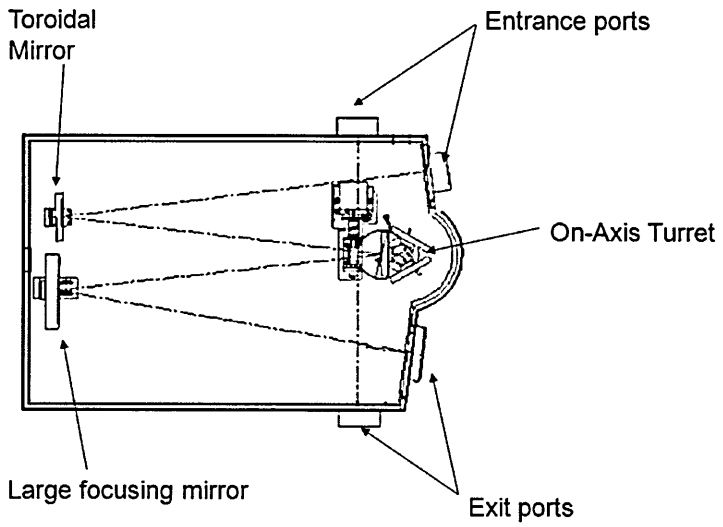


**Figure 3.3:** Schematic of Jobin-Yvon TRIAX320 monochromator [74].

light enters the analyser from the *in vacuo* fibre-optic cable, the light is collimated by the first mirror before reaching the grating. The second mirror then focuses the light, which arrives from the grating, to the exit point [75]. The emission intensity at the various wavelengths is then detected by charge-coupled device (CCD) detector or photomultiplier tube (PMT). Collected data is displayed in the supplied SynerJY® software.

The grating is a set of grooves with a reflective coating that diffracts the light making each groove a source of diffracted light. For certain spacing between grooves and discrete angles, the diffracted light is in phase with light from all other diffraction grooves, creating a constructive interference [76].

Essentially, as can be seen in figure 3.4, the light arrives at the grating at an angle $\alpha$ and, depending on its wavelength, is diffracted at an angle of $\beta$ according to

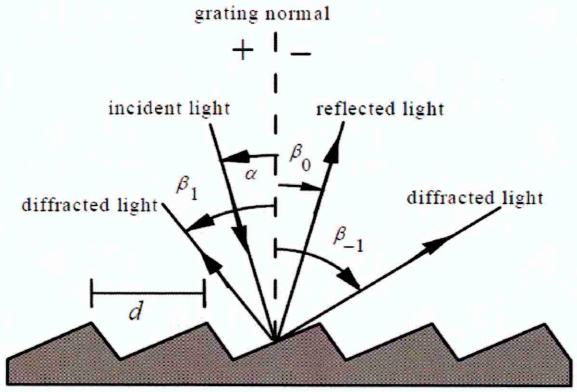


**Figure 3.4:** Schematic of the diffraction of light on a grating [76].

equation 3.5.

$$m\lambda = d(\sin\alpha + \sin\beta) \tag{3.5}$$

where $m$ is the diffraction order, $\lambda$ is the wavelength and d is the groove spacing.

### 3.2.3 Plasma Sampling Mass-Spectroscopy

Mass spectrometry (MS) is a very precise technique for measuring the composition of a substance. Typically, material from a sample is evaporated and ionised and as such is a destructive analytical analysis. The destructive element of plasma sampling MS relates to the change in plasma composition when extracting ions from the plasma, resulting in an inaccurate measurement of the actual plasma. Due to plasma sampling MS only requiring a small number of ions for analysis, the influence on the plasma is minimal. Further, it is possible to analyse low density plasma where the

density is too low for optical diagnostics [27]. With modern mass spectrometers it is possible to analyse positive and negative ions as well as neutrals. The used Hiden Analytical PSM 003 (schematic in fig.3.5) uses a 200 µm sampling orifice to extract species from the plasma. An electron impact ioniser ionises neutral species. The Bessel-type filter selects ions by energy and a quadrupole selects the required ions by mass. To detect ions, a secondary electron multiplier, constructed as a continuous dynode, is used.

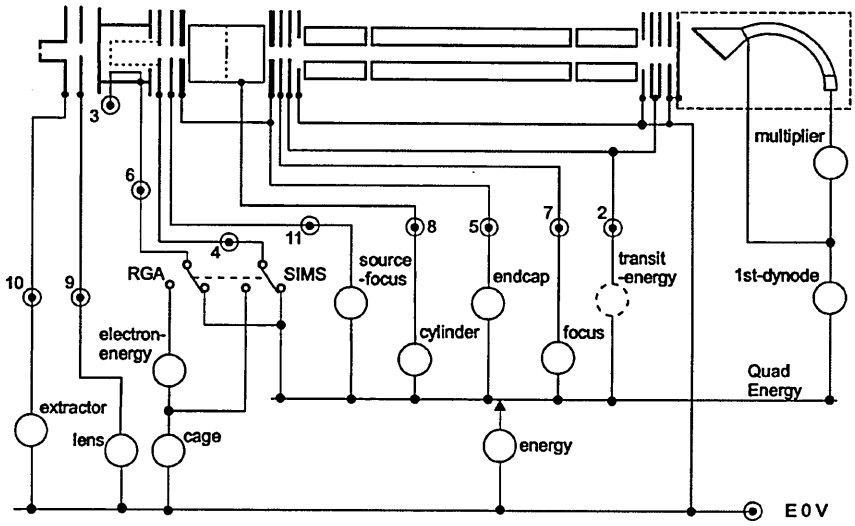


**Figure 3.5:** Hiden Analytical PSM 003 mass spectrometer setup of ion lenses, Bessel box energy analyser, quadrupole mass analyser and secondary electron multiplier [77].

As the individual monitored species have different masses and charges, it is possible to select them by their flight path through a series of electric fields. These can be adjusted to filter out species, which do not have the required mass or charge. MS measurements need to be conducted in a secondary vacuum environment to

minimise collisions with other gaseous species [78]. Due to the influx of species at various angles, up to 5° acceptance angle in PSM 003, ion lenses are used to focus the ions into the Bessel box type energy analyser. To observe neutral species, the flux can be ionised by electron impact ionisation before entering the ion lenses. This measurement is also called residual gas analysis (RGA). The Bessel box was first reported by Allen et.al. [79] as an alternative to more complex energy filters. The name originates from the modified Bessel functions which are applied. The Bessel box is a simple cylindrical electrode with orifices in the end caps on either side of the cylinder. Particles with high energy on a line-of-sight path are blocked by a blocking plate in the centre of the cylinder. By applying a potential to the cylinder and the end caps, it is possible to influence the trajectory of the ions which allows only ions with a specific energy to pass through the second end cap. Mass filtering is conducted by a quadrupole mass analyser. Paul and Steinwedel [80] first presented the quadrupole as a mass filter in 1953. Alternating DC and RF potentials are applied to two sets of two opposing connected rods to create an electric field along the z-axis. Ions injected into the quadrupole in z direction are then deflected by the x and y potentials onto a cycloidic path with a specific radius (r) for the individual mass ($m$) and charge ($z$) of the ion. For low radii the ions will pass the mass filter; higher radii than the distance of two opposing rods will result in the ions colliding with the rods [81].

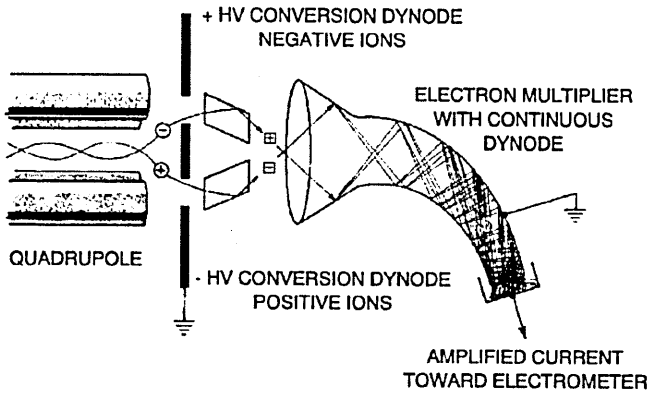


**Figure 3.6:** Working principle of a dynode electron multiplier [81].

After the ions are selected according to their $m/z$-ratio, the ions are accelerated towards a conversion dynode (fig. 3.6). When striking the dynode, secondary electrons are emitted. These secondary electrons are then channelled into a continuous dynode secondary electron multiplier (sem) further colliding with the walls. With each strike the number of secondary electrons are increased. The resulting flux of secondary electrons is related to the amount of secondary particles which are emitted by the conversion dynode per striking ion and the multiplication factor of the SEM. The energy resolved mass spectrometer was used to sample a volume near the substrate as shown in figure 3.1. Mass and energy of Ar, Cu, Ti and Ni single and double-charged ions, as well as the $^{36}$Ar isotope were measured. The energy spectra resolution of the instrument is better than 0.5 eV. IEDF are measured for increasing RF power from 1000-4000 W to gain an understanding of the effect of power on the ion energy.

The integral of the MS intensity is calculated to correlate it to the applied RF-power

in a log-log graph, analogue to the slope for the OES emission.

## 3.3 Modelling of the Excitation Properties

To get an understanding of the excitation mechanisms in a given plasma, a model can be applied to the measurement data. To solve the model equations, assumptions e.g. the distribution function of the electron energy, need to be made. In this thesis the neutral atoms, single- and double-charged ions of the gas and metal species are analysed and compared to a collisional-radiative model by Guiamares et.al. [82, 83] modified by Dony et.al.[84] to correlate the optical emission to the applied DC voltage or RF-power in a log-log graph and the corona models of Rossnagel et.al.[85] and Pintaske et.al. [86], which were developed for DC and RF magnetron plasma processes and explain the correlation of power applied to the cathode to the plasma density, optical emission from Ar neutrals, metal neutrals and metal ions emission. The model predicts the emission intensity of the element ($I_{El}$) to be related to the applied power ($P$) by a power law in which the exponent ($\beta$) varies for different species depending on the number of collisions required to achieve the excited state that produced the emission.

$$I_{El} = P^{\beta} \tag{3.6}$$

For example, the exponent for metal neutrals and metal ions would be two and three times the value for the Ar neutrals respectively. The model assumes electron collision from the ground state to be the main excitation and ionisation mechanism. It neglects population from upper lying states due to their short life time. It assumes Corona equilibrium conditions considering a balance between collisional excitation and radiative decay.

In the following paragraphs, a description is given on how the approach by Dony [84] for correlating the plasma emission intensity to the power applied to the cathode in a log-log graph is applied to ICIS. In the case of ICIS, the plasma intensity is related to the increasing set power applied to the RF-coil. Generally, the relation between emission intensity of the element ($I_{El}$) and RF-power ($P$) in the coil is expressed by a power law with an exponent $\beta$, of which the value is specific to each excitation or ionisation level. In a log-log scale graph, $\beta$ represents the slope of the line in the graph.

For the intensity of argon neutrals and metastables the following relation is experimentally obtained:

$$log(I_{Ar}) = \beta \cdot logP \tag{3.7}$$

where $I_{Ar}$ is the intensity of Ar for a chosen wavelength, $P$ is the power applied to the RF-coil and $\beta$ is the slope of the line obtained for $Ar^0$ in a log-log graph.

For electron collision dominated processes and optical emission measurements the equation can be expanded to

$$I_{El} = K_{El} \cdot n_{El} \cdot n_e \cdot C^{El} \tag{3.8}$$

Where $K_{El}$ is a function of the spectral response of the spectrometer and the radiative frequency and can be considered constant for a given line, $n_{El}$ is the examined species density and $n_e$ is the electron density. $C^{El}$ is the production rate by electron collisions which depends on electron temperature ($T_e$). $T_e$ is assumed to be constant for constant pressure and invariant to applied power.

To determine the effect of increasing power on the electron temperature, it is possible to use the emission line ratio method. The line ratio method is a widely used method to determine the electron temperature from emission lines and is used for species of the same excitation state. When the upper energy levels of two spectral lines are close to partial LTE and thus can be described by the Boltzmann distribution [87]. From equation 3.9 it can be deduced that the ratio of the emission lines is solely a function of the electron temperature $T_e$, from this follows that estimation of the electron temperature is possible by determining the ratio of the emission lines.

$$\frac{I_z(p \rightarrow q)}{I_z(p' \rightarrow q')} = \frac{\lambda_{p'q'}}{\lambda_{pq}} \frac{A_z(p \rightarrow q)}{A_z(p' \rightarrow q')} \frac{g_z(p)}{g_z(p')} exp\left[-\frac{E_z(p) - E_z(p')}{k_B T_e}\right] \tag{3.9}$$

In equation 3.9 $I_z(p \rightarrow q)$ and $I_z(p' \rightarrow q')$ represent the line intensities, $p$ and $q$ represent the lower and upper levels of the respective line, $\lambda$ are the wavelengths, $A_z$ are the respective transitions probabilities, $g_z$ are the respective statistical weights, $E_z$ the energy of the lines, $k_B$ is the Boltzmann constant and $T_e$ is the electron temperature.

To assess the temperature shift as a function of power, the emission line ratio of Ni neutral excitation at different energy levels 310.54 nm (34408 $cm^{-1}$) and 373.68 nm (57789 $cm^{-1}$) was compared to 373.92 nm (28086 $cm^{-1}$). These ratios are sensitive to changes in electron temperature similar to the differences in energy levels. The results (fig. 3.7) indicated changes in ratio for the lower temperatures which increased for powers up to 3000 W and were constant thereafter. The ratio was constant for the higher temperatures, which indicates that the fluctuations in temperature were small and can be neglected. This could be attributed to the high operating pressures of the process, inducing a high frequency of collisions during which electrons are thermalised efficiently.

As the excitation of Ar is predominantly by electron collision the emission intensity

$$I_{Ar} = K_{Ar} \cdot n_{Ar} \cdot n_e \cdot C^{Ar} \tag{3.10}$$

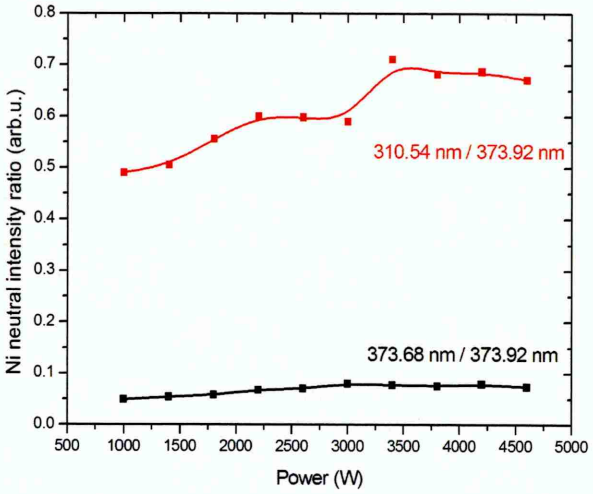


**Figure 3.7:** Electron temperature estimation by calculation of the Ni neutral intensity ratio.

can be assumed as proportional to the electron density $n_e$; from this follows:

$$I_{Ar} \propto n_e \tag{3.11}$$

From equation 3.6 and 3.8 it can be concluded that

$$n_e \propto P^{\beta} \tag{3.12}$$

For the excitation of metal neutrals the intensity is

$$I_{Me} = K_{Me} \cdot n_{Me} \cdot n_e \cdot C^{Me} \tag{3.13}$$

The definition of the sputtering yield is

$$n_{Me} = \varepsilon\gamma_e(n_{Ar^+} + n_{Me^+}) \tag{3.14}$$

where $\varepsilon$ is a constant and $\gamma_e$ is the weighted sputtering coefficient for gas and metal sputtering. As plasma can be considered to be quasineutral, the Ar and metal ion density is equivalent to the electron density

$$(n_{Ar^+} + n_{Me^+}) \approx n_e \tag{3.15}$$

By substituting $(n_{Ar^+} + n_{Me^+})$ with $n_e$ in equation 3.14 and inserting the resulting factor into equation 3.13, it can be concluded that

$$I_{Me} \propto {n_e}^2 \tag{3.16}$$

Following from equations 3.12 and 3.16 for metal neutrals, we can further conclude that

$$I_{Me} \sim (P^\beta)^2 \tag{3.17}$$

From this follows that for Ni neutrals in a logarithmic scale the slope $\beta$ is twice as

steep as for Ar neutrals:

$$log(I_{Ni^0}) \sim 2\beta \cdot logP \tag{3.18}$$

Assuming electron collisions to be the main ionisation mechanism we can assume the metal ion density ($n_{Me^{1+}}$) to be

$$n_{Me^{1+}} \sim n_{Me} \cdot n_e \tag{3.19}$$

From equations 3.12, 3.14 and 3.15 we also know that:

$$n_{Me} \sim {n_e}^2 \tag{3.20}$$

By combining equations 3.12, 3.16, 3.19 and 3.20, we obtain:

$$log(I_{Ni^{1+}}) \sim 3\beta \cdot logP \tag{3.21}$$

for Ni ions. The coefficient of proportionality is higher because a further electron collision is necessary to ionise the metal atoms. This means that the slope of Ni ions is expected to be three times steeper than that of excited Ar neutrals. This is consistent with the findings for conventional DC magnetron sputtering by Rossnagel and Saenger [85]. Furthermore, Penning ionisation of the metal vapour by collisions

with Ar metastables (Ar*) needs to be taken into account due to the high operating pressures of the discharge, which increase the collision cross-section for these types of collisions to be similar to that of electron collision processes. In analogy with the electron collision process, in Penning ionisation the densities of sputtered metal are proportional to the density of electrons,

$$n_{Me+} \approx n_e \tag{3.22}$$

see equations 3.14 and 3.15.

The ionisation of neutral species can also be facilitated by collisions with metastable Ar*, as the metastable potential energy of 11.55 V exceeds the ionisation potential of the analysed metal.

Rossnagel and Saenger [85] have described the density of sputtered material ionised by electron collision to be

$$n_{ion} = \alpha n_e^2 SY \int \sigma_s' \rho_e(E) v dE \tag{3.23}$$

where the $SY$ is the sputter yield, $\sigma_s'$ is the velocity dependant cross-section for the species, $\rho_e(E)$ is the electron energy distribution, $v$ is the electron velocity and $\alpha$ is a constant.

As the ionisation of sputtered metal via Penning collision requires a similar collision path, we can assume the density of metal ions created through Penning ionisation

to be

$$n_{ion}^{Penning} = \beta n_{sput} n_{Ar^*} \int \sigma'_{Penning} \rho_{Ar}(E) v dE \tag{3.24}$$

As the excitation of argon to the metastable state ($Ar^*$) by electron collision requires a similar collision path to that of the sputtered target material, we can assume the density of metastable argon to be

$$n_{Ar^*} = \alpha n_{Ar} n_e \int \sigma'_s \rho_e(E) v dE \tag{3.25}$$

As Penning ionisation describes the ionisation of sputtered material by metastable gas collision, we can replace the electron density by the metastable argon density in equation 3.25, resulting in a density of Penning ionised sputtered material of

$$\begin{aligned} n_{ion}^{Penning} = \beta n_{sput} n_e n_{Ar} \int \sigma'_{Penning} \rho_{Ar}(E) v dE \int \sigma'_e \rho_e(E) v dE \\ \sim n_{sput} n_e C(T_e) \sim n_e^2 SYC(T_e) \end{aligned} \tag{3.26}$$

where $\sigma'_{Penning}$ is the cross-section of Penning ionisation for Ar and $C(T_e)$ is a constant related to the creation rate of metastable Ar and rate of Penning ionisation. As has also been shown by Mehdi et.al. [30], assuming the density of sputtered

species to be proportional to the electron density, from equation 3.26 it can be estimated that Penning ionisation can influence the intensity proportionally to $n_e^2$, which is identical to the two-step electron collision mechanism.

This analysis indicates that both electron collision and Penning ionisation lead to a similar trend for intensity vs. plasma density and applied RF-power.

## 3.4 Thin Film Characterisation

The characterisation of the deposited coatings was conducted with a SEM to analyse the coating structure, as well as the thickness, by examining the cross-section of the sample. To analyse the coating composition and contamination by other materials such as Cu from the ICIS-coil, or remnant materials from other processes deposited in the chamber energy dispersive x-ray spectroscopy (EDX) was used.
Magneto optical Kerr-effect microscopy (MOKE) was utilised to determine the magnetic properties of the nickel coatings. The MOKE measurements were conducted at the University of Lisbon by Prof. Olivia Conde.
In the following, a more detailed overview of the applied analytical instruments will be given.

### 3.4.1 Scanning Electron Microscopy & Energy Dispersive X-ray Spectroscopy

Scanning electron microscopes are used to examine the surface structure of material. As they use an electron beam to create an image, the depth of field and resolution is

much higher than for light-emission based microscopes. In SEMs the electron beam is created by an electron gun and passes a number of electromagnetic lenses and apertures before focusing on the substrate surface (fig.3.8) [88]. Typical acceleration voltages for SEM work are in the range of 1-40 kV, depending on the material and the required analysis.

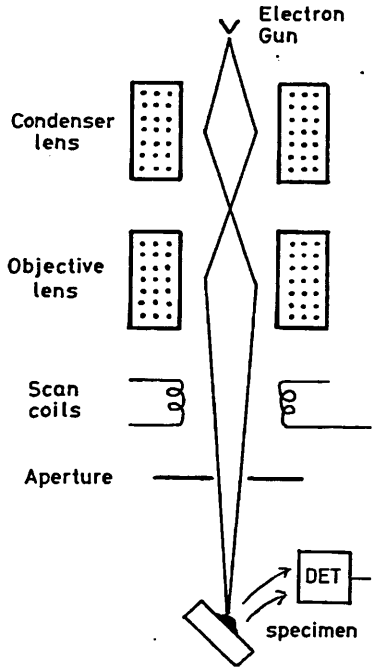


**Figure 3.8:** Schematic of the imaging components of an SEM [89].

A beam deflection system, typically two sets of scan coils inside the objective lens setup, moves the beam across the sample surface as a line raster. The electron signal is then recorded by a detector, amplified and each measurement point is correlated to a pixel on the display to create an image. The magnification in an SEM is determined by the ratio of the size of the display to the size of the scanned area. This allows

for very high magnification levels of several 100,000× [88]. When the beam hits the surface, secondary electrons, backscatter electrons and x-rays created by elastic or inelastic scattering are emitted. Figure 3.9 shows the electrons of the beam penetrating the surface and the region from which the resulting secondary electrons, backscatter electrons and x-rays originate. Secondary electrons are typically used for topographical images. Backscatter electrons primarily give compositional contrast [88], and x-ray detection is mainly used for chemical analysis [89].

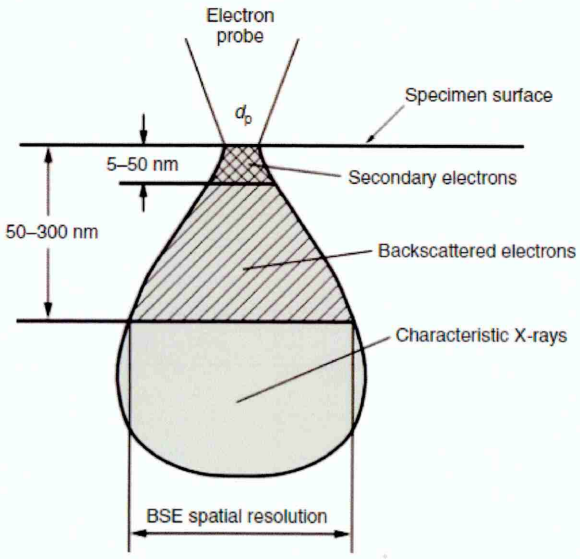


**Figure 3.9:** Schematic of the origin of electrons emitted from the sample [88]

Typically, an Everhart - Thornley detector (ETD) is used to detect signal electrons. The ETD is set at an angle to the sample surface normal; this allows for secondary electrons with large deflection angles and backscatter electrons to enter the detector directly. A Faraday cage is used to attract or repel electrons[88]. When the electrons hit a scintillator, e.g. phosphor, light is emitted which can then be detected by a

photomultiplier [89].

A further detector is the Through - Lens - Detector (TLD). Here the sample is placed within range of the magnetic field of the objective lens; this allows secondary electrons to pass through the lens where they are attracted to a positively biased detector. These electrons are mainly emitted perpendicularly to the sample surface, thus suppressing any shadowing effect that may occur by more scattered electrons [90].

In this work, an FEI Nova NanoSEM 200 in TLD and immersion mode is used with an accelerating voltage of 12 kV to analyse the microstructure of the coating and the coverage of the vias in the samples.

EDX analysis uses an electron beam to excite atoms to emit their characteristic x-rays. When a highly energetic electron ejects an electron from an inner shell of an atom, the atom is ionised. The energy difference between an inner shell and an outer shell electron causes the characteristic x-rays to be emitted or a further electron to be ejected, the so called Auger electron. The radiation that is used for analysis is emitted from the transitions that take place between the K, L, and M shells of the atoms [88].

### 3.4.2 Magneto Optical Kerr-Effect Magnetometry

The magneto optical Kerr-effect (MOKE) describes the rotation of polarised light passing through transparent paramagnetic materials, first discovered by Faraday in

1846 [91]. In 1876, John Kerr [92] observed the rotation of polarised light reflected from a ferromagnetic surface. The magnitude of the rotation is proportional to the magnetisation of the material and for metal films the probe deapth can be 10-20 nm [91].

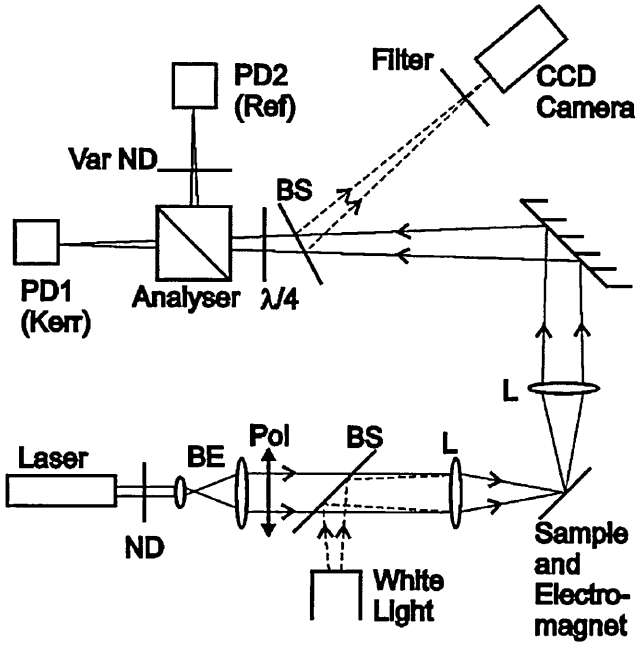


**Figure 3.10:** Schematic of a MOKE microscope with additional optical imaging [93].

In fig.3.10, a schematic of a MOKE microscope as proposed by Allwood et.al. [93] is given. Here two optical systems are incorporated to enable the simultaneous MOKE measurement and imaging of the sample surface; beam splitters are used to separate the optical and MOKE signals. In this system, a solid-state laser beam initially passes through a neutral density filter and half-wave plate to reduce the laser power. This is necessary to be able to operate the laser in a stable regime. The beam is

then expanded to improve the polarisation ratio and focused onto the sample surface. The reflected beam is then directed to a polarising analyser to separate the Kerr and reference signal.

# CHAPTER 4

# Results & Discussions

## 4.1 Initial ICIS Setup Experiments

The incorporation of ICIS technology into a UHV deposition system, involved making a suitable connector to allow for the RF power supply to be operated in pulse mode. Results from the initial experiments have been published in the paper "A novel sputtering technique: Inductively Coupled Impulse Sputtering (ICIS)" [94].

This connector is an analogue / digital input plug converting to a Bayonet Neill - Concelman (BNC) connection (fig.4.1), which is used to connect a pulse delay generator. The circuit consists of a metal-oxide-semiconductor field-effect transistor (MOSFET) and two resistors to switch the RF-power signal on and off with the incoming pulse signal. The pulse delay generator is connected to the pulse signal output of the HIPIMS power supply. With the pulse delay generator it is possible

to synchronise the on-time of both power supplies.

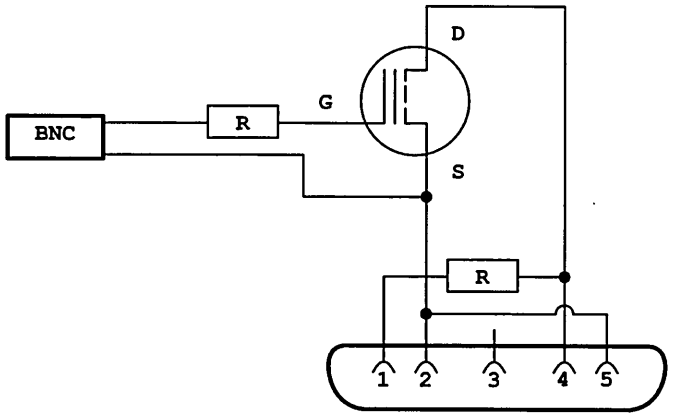


**Figure 4.1:** Schematic of RF-power supply pulsing switch, consisting of a 2N7000 MOSFET and two resistors (R=100 kΩ) inside a housing with analogue/digital converter to BNC input connection.

Initially, a two-turn RF-coil was installed in front of a Ti target. By sweeping through the capacitance values for the $C_T$ (tune) and $C_L$ (load) capacitors in the matching network, an ideal value for maximum plasma intensity was searched for. Only a very faint glow discharge was achieved. To increase the magnetic field strength, the next step was to make a RF-coil with more windings (fig. 4.2) and a smaller diameter. The target material was changed to Cu due to the higher sputter yield. With this setup a higher intensity plasma was noticed, however, the plasma was confined to the centre or the top of the coil (facing away from the target), depending on the direction of the current flow.

From section 2.2.1 it is known that electrons are accelerated along the electric field lines created between the anode and cathode. In RF sources the alternating potential

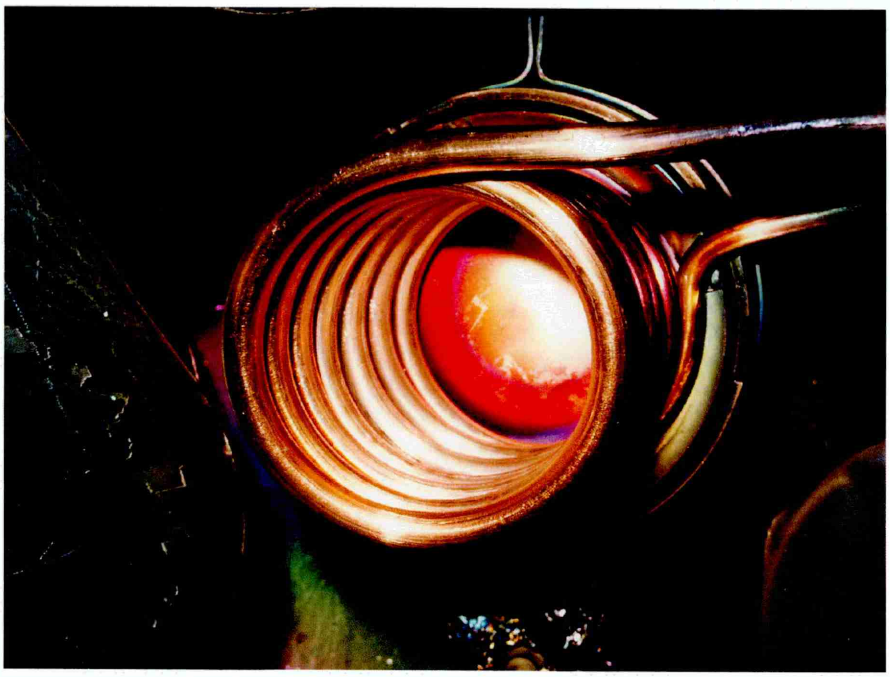

**Figure 4.2:** 7-turn RF-coil positioned in front of the cathode.

lets the electrons oscillate rapidly between the anode and cathode, while the heavy ions are not influenced in their direction due to their high inertia. This allows the ions to pass through the plasma towards the substrate, while the electrons are confined to the coil area. To extend the distance that an electron travels trough the Ar atmosphere even further, a magnetic field is needed. This forces electrons onto cycloidic paths along the electric field lines. As described in section 3.1 in this work a magnetron is not used as a source of magnetic field lines. With a current carrying conductor the direction of the current has an influence on the direction of magnetic field. As the RF signal is positive and negative the directions of the electric and magnetic fields change over the RF pulse duration. During the initial experiments it was found that the connection of the ground terminal has a vital

effect on the plasma generation. When ground is at the substrate facing side of the coil and the power supply at the target side of the coil, the plasma is moved away from the close target proximity, the glow discharge is faint, and the plasma is predominantly on the outside of the coil area. No description of this phenomenon has been found in other literature and further investigation will be necessary to describe it. When the ground connection is on the target facing side of the coil the plasma is in close proximity of the target, expanding over the whole coil with higher power. It is believed that during the negative pulse cycle, due to the retarding force of the E-field from the target the electrons are trapped close to the target surface akin to magnetron sputtering, creating an electrostatic potential well between the cathode and the powered substrate facing end of the coil. This corresponds to the findings of Godyak et.al. [95], where the axial E-field is the driving force for the plasma generation in an ICP process. A schematic of this is shown in figure 4.3.

In the initial process with a Cu target, the colour of the plasma was purple with a light green tint indicating an Ar dominated ionisation in the plasma. The pulse setting for this experiment was a frequency of 500 Hz and a pulse width of 500 µs, creating a duty-cycle of 25 %. To improve the connection to ground potential, a new housing to cover the feedthrough connection on the atmospheric side was designed. With the new housing, it was discovered that the intensity of the plasma was increased substantially. In the 7-turn coil, the plasma was mainly located in the axial centre of the coil. To allow for a greater sputtering rate, we reverted back

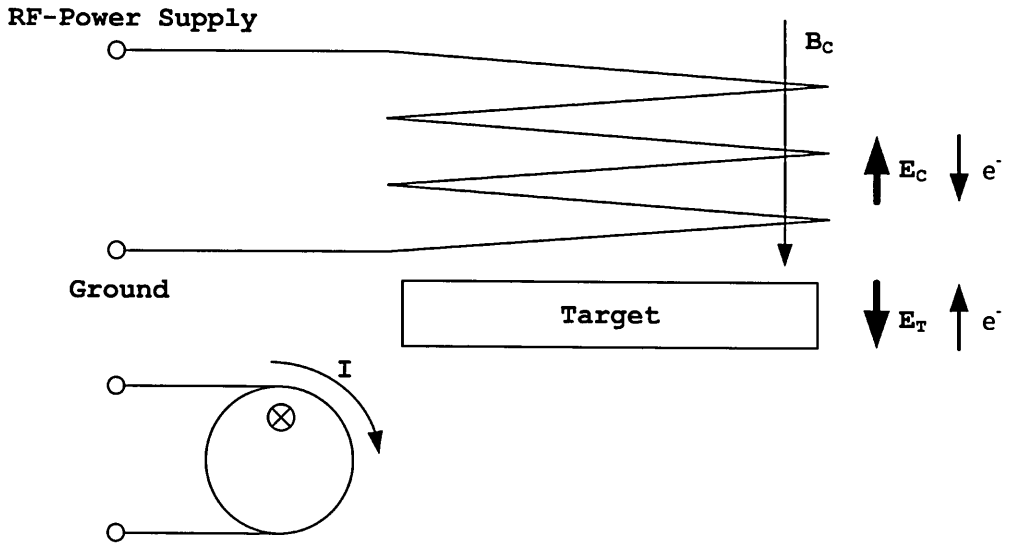


**Figure 4.3:** Schematic of the direction of the E and B fields for negative pulse segments and the corresponding electron motion. The grounded end of the coil at the target end of the coil. Electrons are confined to an electrostatic potential well created between the target and the end of coil connected to the power supply.

to the 2-turn coil applying all changes and settings that have been found to be beneficial for magnet free ICP-sputtering. Fig. 4.4 shows the improved ICIS plasma for the 2-turn coil and a copper target. For high powers, it was found that the voltage and current in the coil cannot be maintained for the whole pulse duration. As can be seen in fig. 4.5, for high powers the voltage signal collapses and starts oscillating before the end of the pulse. To ensure that the pulse is constant, the pulse length is reduced from 500 µs to 150 µs. This allows RF-power settings of up to 4000 W for the full pulse duration. For higher powers the voltage collapses and, as will be seen in section 4.4, the IEDF will be similar to that of a reduction in RF-power in the same order.

**Figure 4.4:** 2-turn RF-coil positioned in front of the cathode.

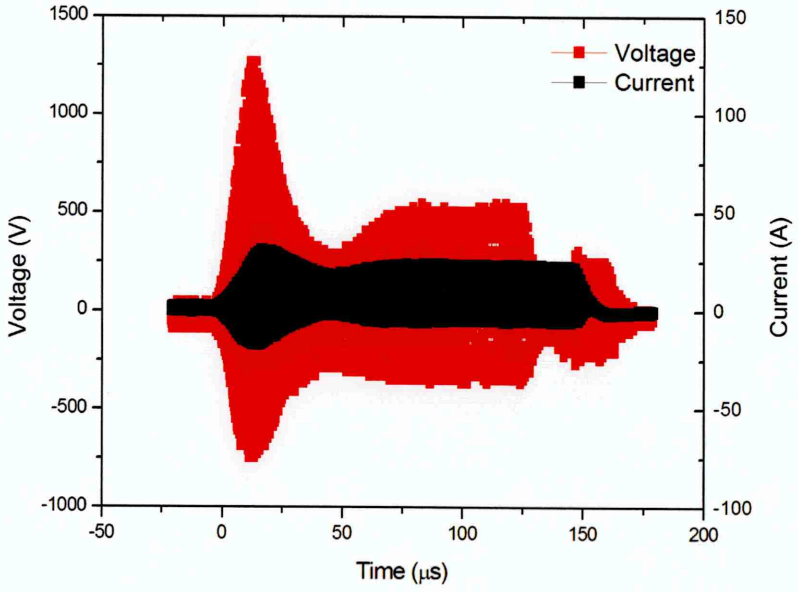


**Figure 4.5:** Current and voltage waveform for high power 4400 W ICIS of Ti.

## 4.2 Plasma Analysis of ICIS by Sputtering of Cu, Ti, Ni

In this section, the ICIS plasma properties of Cu, Ti and Ni by OES and MS are compared for the first time. For a constant pressure of 13 Pa, the power applied to the RF-coil is increased in steps of 200 W from 1000-4000 W to study the effect of increasing RF-power. To study the effect of increasing pressure, the Ar gas flow was increased from 20-120 sccm in steps of 10 sccm. This resulted in a pressure range of 3.3-26.7 Pa. Measurements of the current, voltage, OES signal and MS were conducted simultaneously.

### 4.2.1 Current and voltage on the RF-coil

Current and voltage waveforms for titanium in fig. 4.6 show transient behaviour within the initial 50 µs after the pulse is applied to the coil. During this time the voltage and current go through a maximum value. After this initial spike, the current and voltage reduce to a level that remains constant for the remainder of the pulse. In a similar fashion, the power signal (not shown) exhibits two distinct zones, the first being the initial 30 µs. The second zone from approx. 50 µs to the end of the pulse duration is an area where the power remains constant. In the case of 1000 W set power, the power in the initial phase is actually lower than the second phase. At higher set powers, the transient phase dissipates more power than the rest of the pulse. This indicates that the transient is not part of the traditional glow discharge breakdown, as weak plasma is already being formed in the first few microseconds of

the pulse. The glow discharge breakdown would have already occurred earlier in the RF pulse.

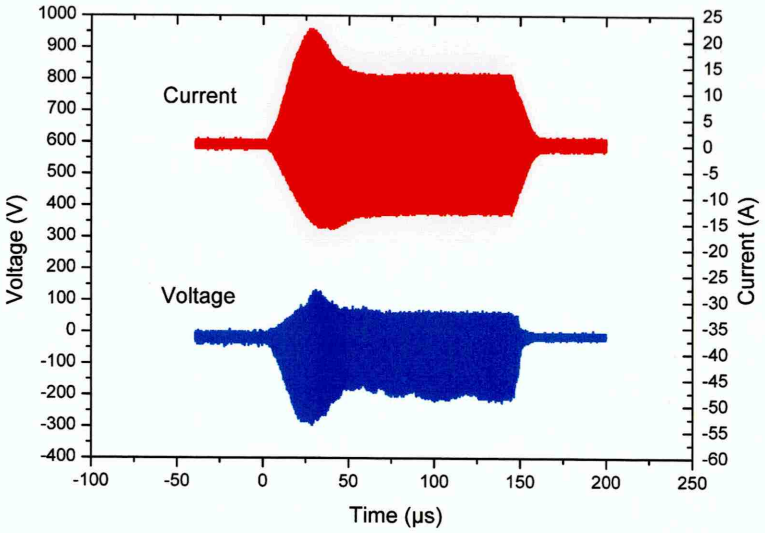


**Figure 4.6:** Current and voltage waveform for a 2400 W ICIS titanium plasma with pulse width of 150 µs and frequency of 500 Hz.

Guo and DeJoseph [73] indicate that the origin of the spike may be due to the design of the power supply delivering a constant power with changing loads and not being fast enough to adapt the voltage to the changing load from the plasma. This is also confirmed by measurements that we have conducted by an Impedans Octiv VI probe. In fig. 4.7, a single pulse with the current, voltage, impedance and phase of Ti sputtered by ICIS is shown. The settings for this pulse were a pulse width of 500 µs; a repetition rate of 500 Hz at a constant power of 2300 W RF-power applied to the internal coil. The voltage initially rises to a peak before reducing to a level which is sustained to the end of the pulse as the current rises. Further, as the current

and voltage rise, the impedance drops to approx. 50 Ω.

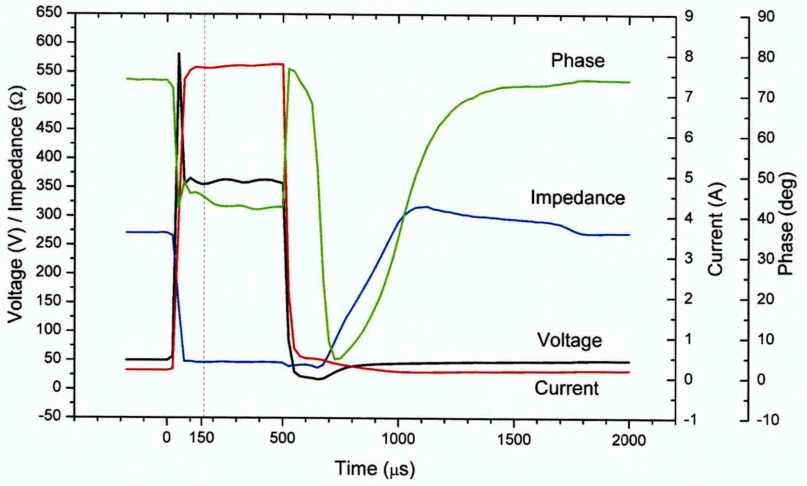


**Figure 4.7:** One titanium 2300 W ICIS pulse, 500 µs pulse width, 500 Hz repetition frequency. Voltage transient indicates the change from capacitive coupling to inductive coupling. Measurement was conducted by Impedans Octiv VI probe. The 150 µs mark shows the pulse width of other measurements.

The phase is reported as the current in relation to the voltage. Current and voltage are 70° out of phase before a pulse is applied, due to a low power RF signal being delivered to the coil by the generator, even during the off-times. This phase is consistent with capacitive coupling (E-mode) discharge. During the pulse the phase changes to 40° which is indicative of an inductive coupling in the discharge (H-mode). When the voltage is reduced and the current drops, the phase returns to 70° and capacitive coupling, but the impedance still remains constant for about 180 µs before increasing again to reach the off-time value. When the impedance starts to rise, the phase jumps to 5°, gradually reverting back to 70° as the impedance increases. These measurements confirm that the transient appears when the load on the power

supply changes rapidly

### 4.2.2 Charge and Resistivity

The measured value for the charge in the RF-coil, fig. 4.8, increases linearly with set power. The deviation from linearity is around -0.05‰. Copper and titanium slopes are nearly identical, while the charge for nickel is lower. However, the trends are similar. Resistivity, fig. 4.9, is not influenced by increasing set power and remains constant, indicating no change to the plasma impedance during the pulse on-time. A small reduction is observed for ICIS of Ni, which is consistent with higher ionisation degree plasma created within the chamber.

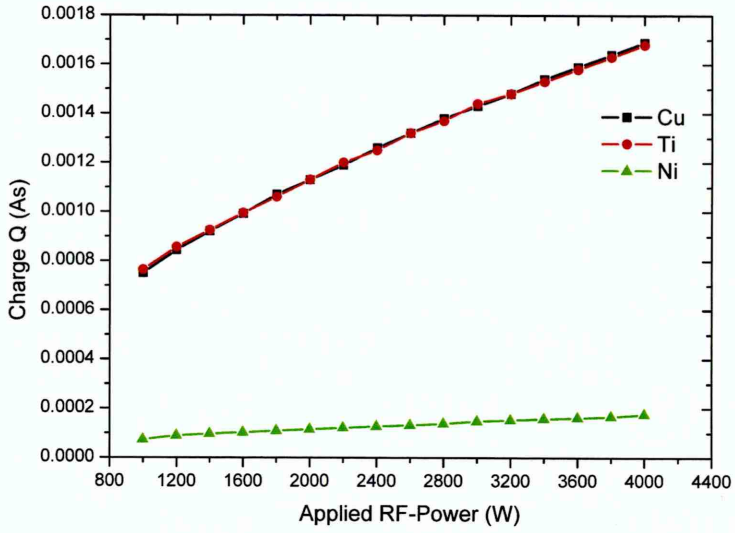


**Figure 4.8:** Charge on the RF-coil with increasing applied RF-power. For all materials, the charge increases linearly with increasing RF-power.

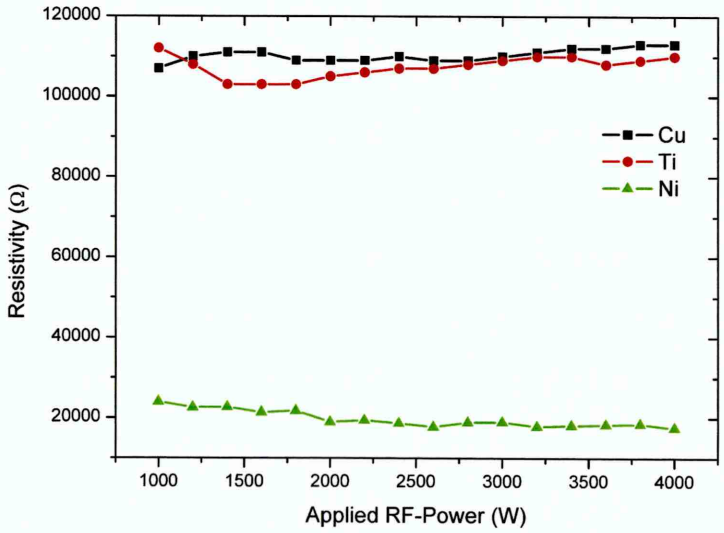


**Figure 4.9:** Resistivity in the RF-coil. For increasing applied RF-power the resistivity does not change.

### 4.2.3 Optical Plasma Analysis

In this section, the results of the optical plasma analysis are presented. The data has been displayed in log-log graphs to enable the comparison with the radiational-collisional model presented in section 3.3.

#### Titanium

OES results for titanium, fig. 4.10, show a linear increase with increasing set power. For all species, the slope is slightly steeper for the first two power settings. However, for further increases the argon remains linear with a lower slope. For the metal species, compared to argon, there are some deviations from the straight linear increase. These deviations are within the error margin.

Comparing the result with the model, as can be seen in table 4.1, the slope for the Ti neutrals is about twice as steep as the argon slope. Ti ions also follow the model with a slope three times steeper than Ar.

**Table 4.1:** Slopes of different regions on the Ti OES intensity graph.

| Applied RF-Power | Ar I (750.387 nm) | Ti I (363.546 nm) | Ti II (376.132 nm) |
|---|---|---|---|
| 1000 - 4000 W | 0.29 | 0.73 | 0.96 |
| 1200 - 4000 W | 0.28 | 0.70 | 0.88 |
| 1000 - 2000 W | 0.32 | 0.83 | 1.23 |
| 2000 - 4000 W | 0.28 | 0.78 | 0.84 |

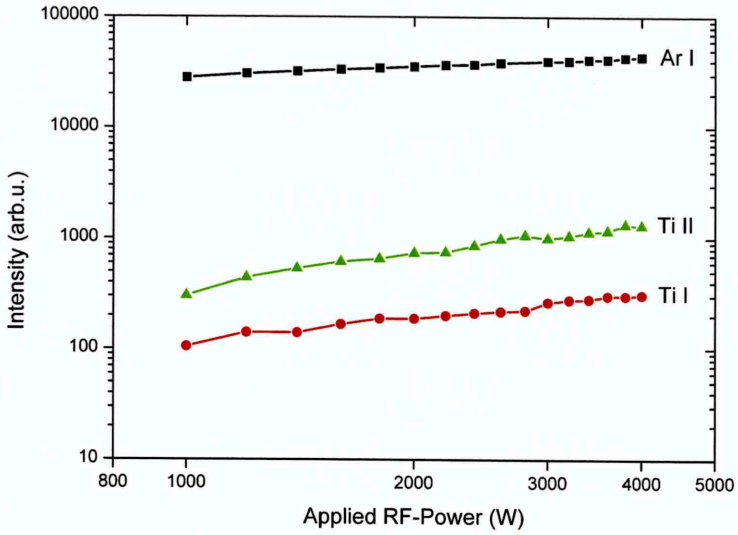


**Figure 4.10:** OES result for excited Ar neutrals (Ar I, 750.387nm), Ti neutral (Ti I, 363.546nm) and Ti ion (Ti II, 376.132). Set power applied to the RF-coil was varied from 1000-4000 W, while the process pressure remained constant. As can be seen from table 3, the slope for Ti I is twice as steep and Ti II three times steeper than the Ar I slope. This result is to be expected according to the model.

### Nickel

As for titanium, nickel exhibits a stronger slope for initial power settings of 1000-1600 W. As can be seen in figure 4.11, the slope is linear and the ratio between the argon and metal neutral slope is approx. 2:1, and between argon and nickel ion it is approx. 3:1 for up to 4000 W set power. Slope values in table 4.2 show that there is only little deviation for Ar and Ni ions for different areas over the graph. The slope for Ni neutrals is steeper at the lowest power settings; this may be a reason for the larger deviation from the model compared to the other species.

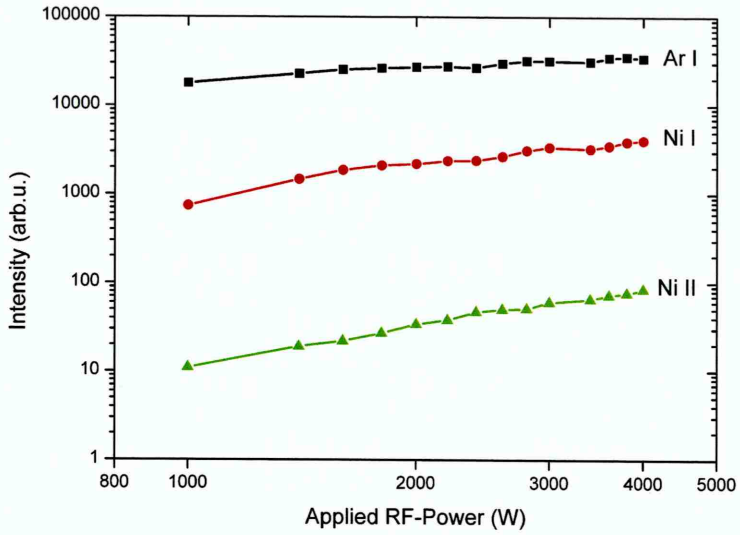


**Figure 4.11:** OES results for excited Ar neutrals (Ar I, 750.387nm), Ni neutral (Ni I, 310.188nm) and Ni ion (Ni II, 333.188nm). Set power applied to the RF-coil was varied from 1000-4000 W, while the process pressure remained constant. As can be seen from table 4.2, the slope for Ni I is twice as steep and Ni II three times steeper than the Ar I slope. This result is to be expected according to the model.

**Table 4.2:** Nickel OES intensity slopes as calculated in the log-log graph in fig.4.11

| Applied RF-Power | Ar I (750.387 nm) | Ni I (310.188 nm) | Ni II (333.188 nm) |
|---|---|---|---|
| 1000 - 4000 W | 0.43 | 1.07 | 1.45 |
| 1400 - 4000 W | 0.38 | 0.88 | 1.40 |
| 1600 - 3400 W | 0.42 | 0.82 | 1.46 |

### Copper

Figure 6 shows the slopes resulting from OES measurements for increasing set RF-power in a log-log graph. The slope for Ar is increasing linearly, while for the metal species there are two visible slopes. These slopes have been examined analogous to the model defined by Dony et al. [84] . From this we expect the slopes for the

metal species to be twice as steep for metal neutrals and three times as steep as the slope of argon for metal ions. When considering the complete power range from 1000-4000 W, the measurements follow the model very closely. However, when looking at the two zones / ranges there is a difference in how the slopes relate to each other. As can be seen from table 4.3, the slope at low power (1000-1600 W) does follow the model, albeit with a factor of 4 steeper slopes. The origin of the factor 4 increase is not known, but could be due an additional source of copper such as sputtering of ICP coil material. The slope at high power (1800-4000 W) does not show any relation to the model.

**Table 4.3:** Copper OES intensity slopes as calculated in the log-log graph in fig. 4.12

| Applied RF-Power | Ar I (750.387 nm) | Cu I (327.396 nm) | Cu II (455.592 nm) |
|---|---|---|---|
| 1000 - 1600 W | 0.38 | 1.48 | 2.60 |
| 1800 - 4000 W | 0.33 | 0.35 | 0.68 |
| 1000 - 4000 W | 0.37 | 0.63 | 1.07 |

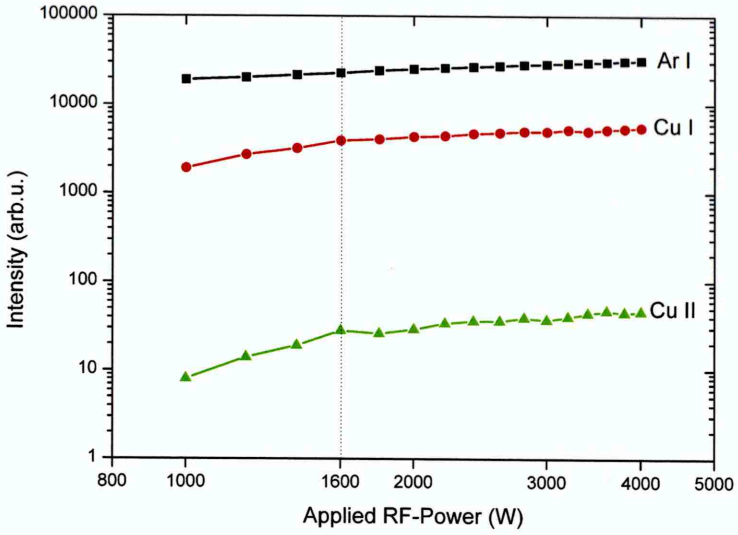


**Figure 4.12:** OES Intensity slopes for argon neutral (Ar I, 750.387 nm), copper neutral (Cu I, 327.396 nm) and copper ion (Cu II, 455.592 nm). For applied RF-power of 1000-1600 W the intensity increases linearly, with the slope of the Cu I being four times and Cu II seven times steeper than predicted by the model.

The radiational-collisional model discussed in section 3.3 expects that the slope value of the exited argon in a log-log graph represents a factor of 1. Further, the model predicts that the excitation and ionisation of the metal each increase the the slope factor by a further factor of one respectively in relation to the Ar slope. These expectations and predictions of the model are in very good agreement with the experimental data for titanium and nickel. From this is can be concluded, that the assumptions made to be able to calculate the model are correct. In the case of ICIS plasma this means that the main excitation mechanisms are electron collisions for all species and excitation states observed by optical emission spectroscopy. In the case of copper, the deviation from the model expectations need to be examined

further.

### 4.2.4 Energy and Mass Spectroscopy

#### Titanium

In figure 4.13, the integral of the MS data shows a decrease for $Ar^{1+}$ for increasing RF-power. $Ar^{2+}$ initially rises reaching a maximum at 1600 W set RF-power, before following the linear decrease with the $Ar^{1+}$.

$Ti^{1+}$ and $Cu^{1+}$ integral intensities rise linearly with increasing power, with the $Cu^{1+}$ having a higher intensity for powers over 1400 W. The $Ti^{2+}$ integral exhibits a general linear rise in intensity. $Cu^{2+}$ intensity is decreasing logarithmically for increasing set power.

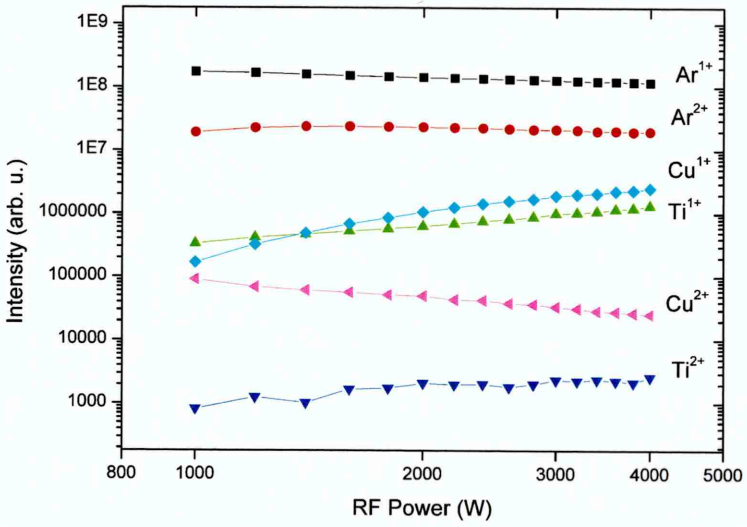


**Figure 4.13:** Integral of the mass spectroscopy intensity of increasing set RF-power. The reduction in intensity is probably caused by charge transfer.

The IEDF for $Ti^{1+}$ in an ICIS plasma in fig.4.14 shows a low energy peak at 3 eV, with increasing intensity for increasing applied RF-power. The second low energy peak has the strongest intensity. It ranges from 20 eV reducing to 10 eV with increasing power. The peak also narrows from a width of 30 eV to 10 eV. Higher energetic peaks appear around 120 eV for 1400 W RF-power, increasing to 160 eV for 4000 W RF-power.

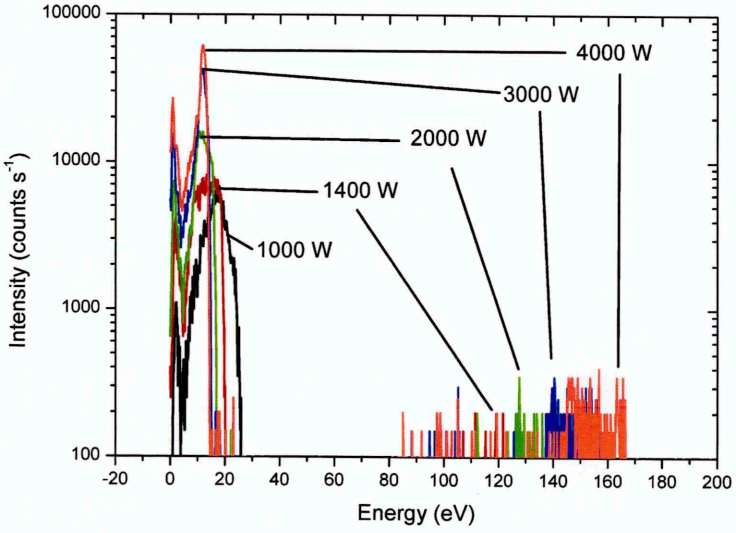


**Figure 4.14:** IEDF of $Ti^{1+}$ ICIS plasma for increasing RF-power with constant process pressure.

### Nickel

The $Ni^{1+}$ and $Ni^{2+}$ integral intensities in fig.4.15 increase with the set power.

$Ar^{1+}$ and $Ar^{2+}$ ions decrease and increase again for power above 3500 W.

As this is the case for the $Ar^{1+}$ (40amu), $Ar^{2+}$ (20amu) and for the 36 amu Ar isotope, the behaviour can be considered real.

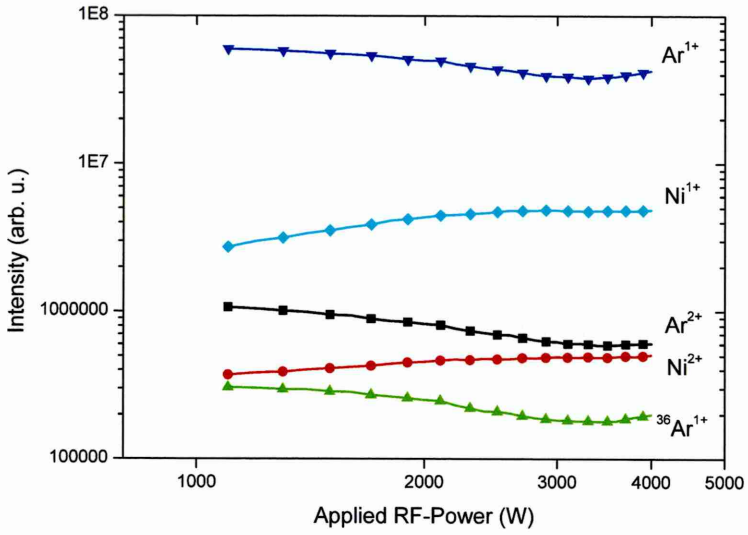


**Figure 4.15:** Integral of the MS intensity of a Ni ICIS plasma for increasing RF-power with constant process pressure.

The IEDF for $Ni^{1+}$ in figure 4.16, shows 2 peaks at low energy levels and one peak at high energy levels. The first low energy peak appears at 1 eV and the signal increases with applied power. A second low energy peak at 20 eV, shows a slight increase in plasma potential with increasing power. The high energy peak appears at 140 eV for 1100 W applied power, reaching a maximum of 170 eV for powers above 3000 W RF-power.

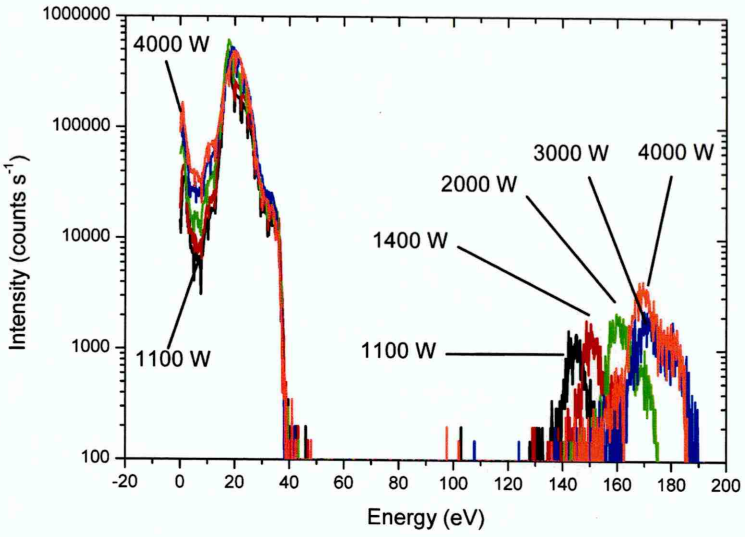


**Figure 4.16:** IEDF of $Ni^{1+}$ ICIS plasma for increasing RF-power with constant process pressure.

### Copper

The integral of the MS signal for a Cu ICIS plasma for increasing set power to the RF-coil in fig. 4.17, shows a linear increase for all species for the set powers up to 1600 W. For higher powers, the $Ar^{1+}$ and $Ar^{2+}$ lines decrease linearly, while the $Cu^{1+}$ line continues to increase before the intensity saturates for powers above 4000 W. $Cu^{2+}$ intensity does not change significantly for powers above 1600 W.

The IEDF in fig.4.18, shows two pronounced peaks at the low energy levels of 3 eV and 20 eV, with the 20 eV peak becoming narrower and shifting slightly to lower energy levels. Higher energetic ions show at 100 eV; here the ions are mainly from high RF-power processes. A second high level energy peak is visible for the 2000 W

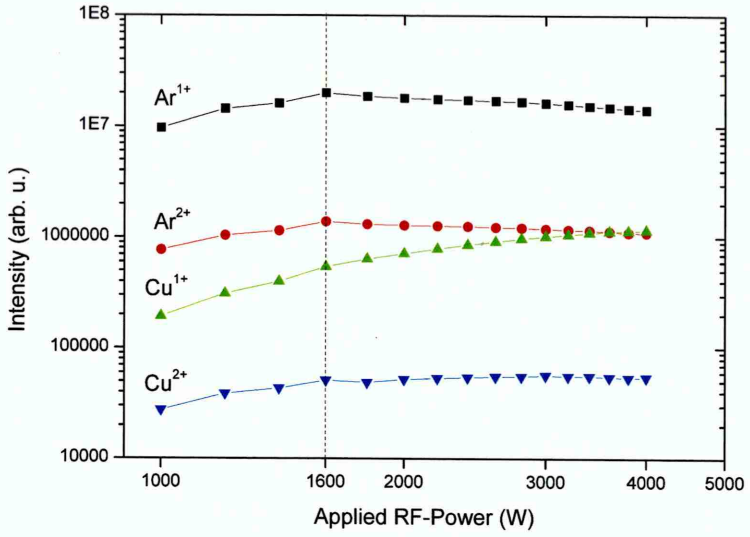


**Figure 4.17:** Cu ICIS MS integral signal normalised to $Cu^{2+}$. $Ar^{1+}$ is on the left y-axis, the other elements on the right y-axis. All elements increase linearly for powers up to 1600 W.

process at 140 eV, increasing to 160 eV for 4000 W applied RF-power.

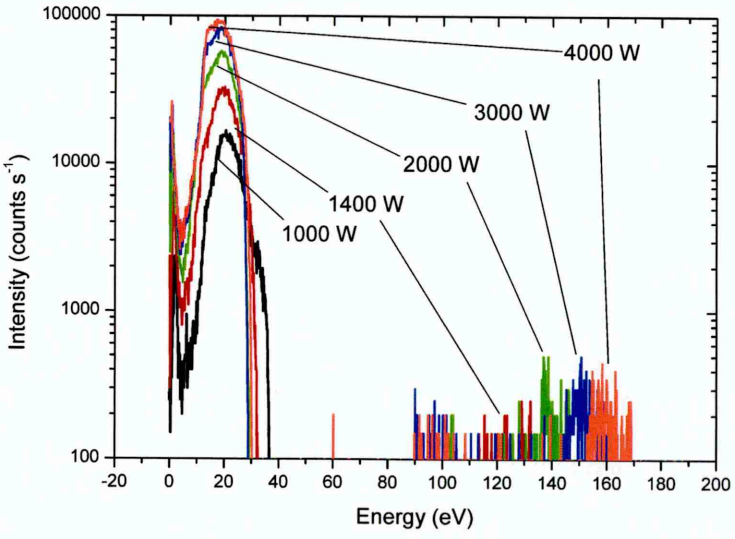


**Figure 4.18:** IEDF of $Cu^{1+}$ in an ICIS plasma for increasing power at a constant process pressure of 14 Pa.

### Summary of ICIS Plasma Investigations

Concluding from section 4.2.1 the pulse shape of the current and voltage waveforms in figure 4.6 show a strong similarity to the ICP discharges described by Guo and DeJoseph [73]. The initial peak in voltage is described by Guo and DeJoseph as a feature of the power supply which cannot react fast enough to reduce the voltage and follow reduction in impedance. Measurements with an Impedans OCTIV VI probe (fig. 4.7) have given a clear indication that the main energy coupling, during the pulse on-time, is inductive. The coupling switches from capacitive to inductive within a few microseconds of applying the voltage, indicating an efficient ionisation of the gas, accompanied by a quick rise in plasma density as indicated by a drop in impedance to 50 Ω. The rapid power switch off of voltage at the end of the pulse leaves a high density plasma driven by a small voltage field, establishing capacitive coupling for some 180 µs. As the plasma begins to decay, the phase briefly turns resistive (8°phase) and the voltage rises by 25 V, while the current slowly decreases to 0 A. The decay of plasma is relatively slow due to the low cross-section of three-body recombinations and the slow diffusion of ions to the walls given by the high operating pressures. As the impedance reaches a maximum, the phase returns to capacitive coupling (75°) for the remainder of the pulse period.

In section 4.2.2 the resistivity in the coil has been measured and did not change with increasing applied power (not shown), indicating a capacitive portion of the

discharge which is not influenced by the increasing applied power. The linear charge increase indicates that the increasing energy is delivered into the discharge and the actual power is proportional to the power set at the power supply.

**Table 4.4:** Excitation energy of examined species

| Titanium Excitation Energies | | |
|---|---|---|
| | kJ/mol | eV |
| $Ti^0$ | 658.80 | 6.83 |
| $Ti^{1+}$ | 1309.80 | 13.58 |
| $Ti^{2+}$ | 2652.50 | 27.49 |
| **Copper Excitation Energies** | | |
| | kJ/mol | eV |
| $Cu^0$ | 745.50 | 7.73 |
| $Cu^{1+}$ | 1957.90 | 20.29 |
| $Cu^{2+}$ | 3555.00 | 36.84 |
| **Nickel Excitation Energies** | | |
| | kJ/mol | eV |
| $Ni^0$ | 737.10 | 7.64 |
| $Ni^{1+}$ | 1753.00 | 18.17 |
| $Ni^{2+}$ | 3395.00 | 35.19 |
| **Argon Excitation Energies** | | |
| | kJ/mol | eV |
| $Ar^0$ | 1520.60 | 15.76 |
| $Ar^{1+}$ | 2665.80 | 27.63 |
| $Ar^{2+}$ | 3931.00 | 40.74 |

$1\,\mathrm{kJ\,mol^{-1}} = 1.0364 \times 10^{-2}\,\mathrm{eV}$

Table 4.4 lists the ionisation energies of the species examined in section 4.2.3. The

comparison of Ti and Ni OES results with the model show that these materials adhere very well to the expected result. In a log-log graph, the slope for metal neutrals is twice as steep as the gas slope and for metal ions it is three times as steep. As described earlier in section 3.3 one electron collision is necessary to excite the gas and a further electron collision needed to excite the metal atom, it can be concluded that the density of excited metal atoms and the intensity of light emission are proportional to the number of electrons squared $n_e^2$. To ionise the metal atoms, a further collision is needed and the intensity is related to $n_e^3$. The plasma density is related to the power and emission intensity of Ar neutrals through $P_{RF} \sim n_e^\beta \sim I_{ArI}^\beta$. According to the measurements, the exponent $\beta$ is in the range of 0.3-0.4 for Ni, Ti and Cu discharges. This signifies a faster than linear increase in density for low powers and a sublinear increase at higher powers. The creation of ions by electron collisions or Penning ionisation, is balanced by charge exchange and outdiffusion towards the anode (chamber walls) and subsequent absorption or neutralisation. The good fit of the data to the described model illustrates that its assumptions are a good approximation of the actual phenomena. Among other things, this signifies similar out-diffusion rates for metal neutrals and metal ions. The OES results for Cu ICIS plasma show a linear increase for all species up to 1600 W applied power. This behaviour is also seen in the MS intensity integral for this process. The reason for this is not clear. Table 4.5 shows that the slopes of the $Cu^{1+}$ MS integral are steeper than the $Ar^{1+}$ slopes, indicating an increasing metal ion content in the plasma. As

the coil material is also copper, there could be additional sputtering of coil material as a second source of optical emission due to the higher sputter yield of copper [96]. This sputtering may also be accelerated by self-sputtering by $Cu^{1+}$ increasing the count rate.

For applied powers above 1600 W $Cu^{1+}$ increasingly takes over sputtering, forcing Ar away from the target. This may explain the reduction in slope, as $Ar^{1+}$ has a higher potential energy it may have a higher secondary electron yield from the target surface. In contrast, $Cu^{1+}$ has a three times lower potential energy. As such it is less efficient in producing secondary electrons and as the Ar is driven away from the target the discharge slows down, resulting in a drop in slope factor. The relation of the Cu neutral slope to the Cu ion slope is close to the model expectation with a higher slope factor.

For Ti and Ni plasma, we have seen that the coil is coated by the target material. Resputtering of Ti and Ni does not seem to have an effect on the plasma.

As discussed in section 3.3, for constant pressure Penning ionisation may have a dependence on the electron density. A higher Ar metastable ratio may be able to explain the factor of 2 increase in slope, from the gas to metal species for Cu at powers below 1600 W compared to the model.

As the slopes of the metal neutrals and ions in the log-log graphs are showing an increase of 1 in slope steepness in relation to each other, assuming that high electron density due to the high applied RF-power offsets the reduced mean free path at

the high process pressure, it can be concluded that Penning ionisation has limited influence on the ionisation for power settings above 1600 W.

There could also be additional sputtering of coil material leading to a second source of optical emission, causing the OES intensity for Cu to be higher than for Ti and Ni.

**Table 4.5:** Slopes of the ICIS of Cu plasma for Cu and Ar ions as measured by Mass Spectroscopy.

| Cu ICIS MS Slopes | 1000 - 1600 W | 1600 - 4000 W |
|---|---|---|
| $Ar^{1+}$ (40 amu) | 1.482 | -0.352 |
| $Ar^{2+}$ (20 amu) | 1.197 | -0.234 |
| $Cu^{1+}$ (63 amu) | 2.141 | 0.816 |
| $Cu^{2+}$ (31 amu) | 1.257 | 0.104 |

A possible reason for the reduced flux of $Ar^{1+}$, $Ar^{2+}$ and $Cu^{2+}$ ions with increasing RF-power could be a reduced efficiency of ionisation due to cooling of the electron temperature.

An estimate of the electron temperature was obtained through the ratio of emission intensity of three resonant Ti I lines, with different upper energy levels and the ground state as lower energy level.

The OES data ratio in figure 4.19, shows an increasing trend with RF-power; this indicates that the electron temperature is rising and not responsible for the reduction in $Ar^{1+}$, $Ar^{2+}$ and $Cu^{2+}$ intensity.

Experiment and model calculations by Dickson et.al. [97] and Nichols et.al. [98], have demonstrated a reduction in electron temperature with magnetron power due to the presence of metal vapour with considerably lower ionisation potential than argon. In the current experiment, increasing RF-power also increases the flux of plasma to the target and increases the flux of sputtered particles, however, the rate of this process is relatively low compared to the heating produced by the RF-power on the coil, as discussed in the following paragraph.

Rossnagel [99] has shown that energising the coil leads to a reduction of gas density due to heating of the gas by collisions with atoms sputtered from the coil, and by charge exchange with ions that have been accelerated either by the potential drop in the presheath or by elastic collisions with electrons. The measured density reduction was as much as 60 % for coil power density of up to $1\,\mathrm{W\,cm^{-2}}$. Further gas heating could come from the sputtered flux from the cathode - according to estimates by Dickson et.al. [97], sputter particle densities equivalent to 1 % of the gas particle density are sufficient to cause rarefaction in excess of 40 %. Extrapolating to the densities of the current experiment of $100\,\mathrm{W\,cm^{-2}}$ and considering plateauing at high powers, we estimate the reduction to be up to 70 % if the power is delivered continuously, or in case of pulsing, the reduction is likely to be less. In the current experiments, the reduction in $Ar^{1+}$ signal was approximately 50 % and could be attributed to heating and rarefaction of the gas by the coil, which is countered by an increase in electron temperature. The reduction was the same regardless of sputter

yield of the material, indicating that cooling of the electron temperature by metal vapour was a minor effect. The situation in the Ni plasma is clearer; as the intensity of the Ni ions is increasing the Ar ions are decreasing, creating a predominantly metal ion plasma.

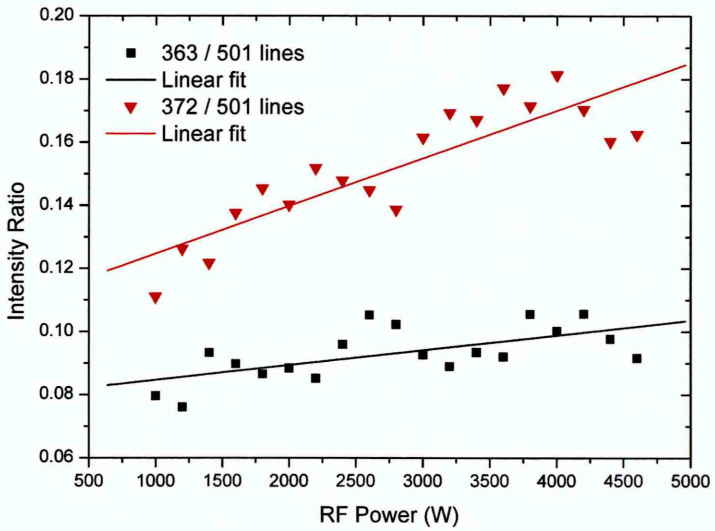


**Figure 4.19:** Ratio of the optical emission intensity of Ti neutral lines with different energy levels indicating a rise of electron temperature with increasing set RF-power. The upper energy levels for the 363 nm line is 3.41 eV , the 372 nm line is 3.32 eV and the 501 nm line is 2.47 eV . Energy levels were retrieved from the ViZier Database [100].

As described in section 2.1.4, in collisional-radiative modelling of plasma processes the densities of the excited states of the specific atom are expressed as functions of the densities of electrons, atoms, ions and the electron temperature. By correlating an external parameter, in this case increasing power, to the emission intensity the used model has helped to link the external effect of increasing RF-power to the

plasma chemistry. The close relation of the experimental data, specifically for Ti and Ni, with the model expectations shows that the model assumptions are suitable and are able to determine the plasma behaviour for increasing applied power at constant process pressure.

The ion energy distribution functions for all three examined materials measured in section 4.2.4, exhibit pronounced high intensity peaks at low energies in the range of 10-20 eV. This is in line with conventional ICP-MS. As will be shown in section 4.4, these low energetic ions can produce dense coatings.

In conclusion, ICIS is a new technology that can effectively sputter magnetic materials and produce a low-energy ion flux beam. However, the ionisation degree is comparable with IPVD magnetron processes.

## 4.3 Analysis of the Effect of RF-Power and Process Pressure on the Microstructure

In this section, an analysis of Cu and Ti coatings deposited by ICIS is performed for the first time. These coatings were deposited by the UHV vacuum deposition system equipped with ICIS technology. A power-pressure matrix was devised to deposit the coatings and to get an understanding of the influence of increasing RF-power at a constant process pressure. For each material, 3 coatings were deposited at different RF-power settings respectively, and a further coating was deposited at the highest power and reduced pressure. The substrates are silicon fragments from the reticle

and are positioned on the substrate holder, rotating at 5 revolutions per minute. The bias of the substrate was kept at floating potential. The coated samples are fractured along the die to analyse the cross section in the SEM.

### 4.3.1 Copper Coatings by ICIS

Copper was deposited on the Si substrates for 120 min to achieve an estimated film thickness of 200 nm. The base pressure was in the range of $4 \times 10^{-4}$ Pa. In the first series of coatings the pressure was kept constant at 13 Pa and the power was increased in steps of 1000 W from 2000 W to 4000 W, to show the influence of increasing the power applied to the RF-coil. For the analysis of the influence of pressure, one coating was deposited at the highest power of 4000 W with a process pressure of 6 Pa. The settings of the pulsed DC bias on the target remain constant at 1900 V. The pulse parameters were a frequency of 500 Hz and a pulse width of 150 µs.

For a power of 2000 W (fig.4.20) the deposition rate is 120 nm $h^{-1}$. The microstructure is dense columnar with perpendicular growth on the top surface. At the edge of a via, the growth is at an oblique angle with increased tilting towards perpendicular at the sidewall. The protuberant material has a hemisphere shape over the thickness of the coating. The sidewalls and bottom of the via are coated evenly with increasing attenuation as the depth increases for high aspect ratios. Via with an aspect ratio of 1:3 or smaller remain open and the sidewalls and bottom are coated evenly.

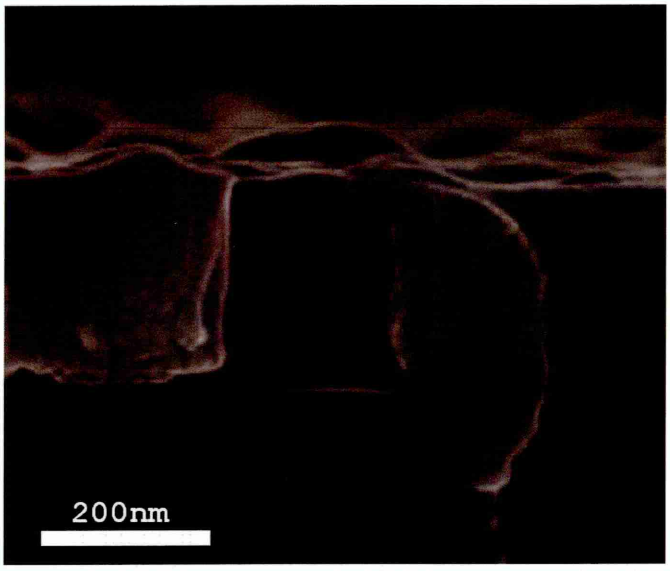


**Figure 4.20:** Cross-section of a corner of a via coated by 2000 W Cu ICIS at a pressure of 13 Pa

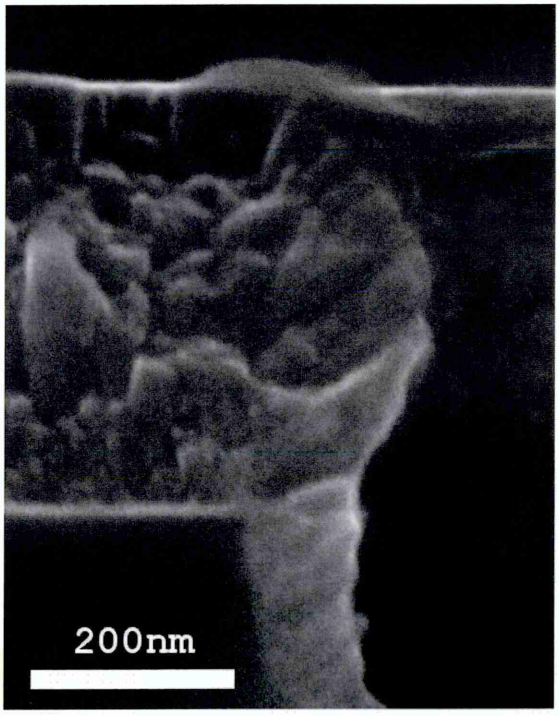


**Figure 4.21:** Cross-section of a corner of a via coated by 3000 W Cu ICIS at a pressure of 13 Pa

For an RF-power of 3000 W the deposition rate increases to 200 nm $h^{-1}$ (fig.4.21). The microstructure is dense columnar with a higher densification of the columns. The protruding material at the edge of the via with an aspect ratio of 1:1.6 has a hemisphere shape over the whole top coating thickness with increased sidewall coating thickness. Via with a ratio of 1:3 fully close after approx. 80 min. The rate of via closure increases with coating thickness. While the via is open, the coverage of side walls and bottom is even, attenuating towards the bottom of the via.

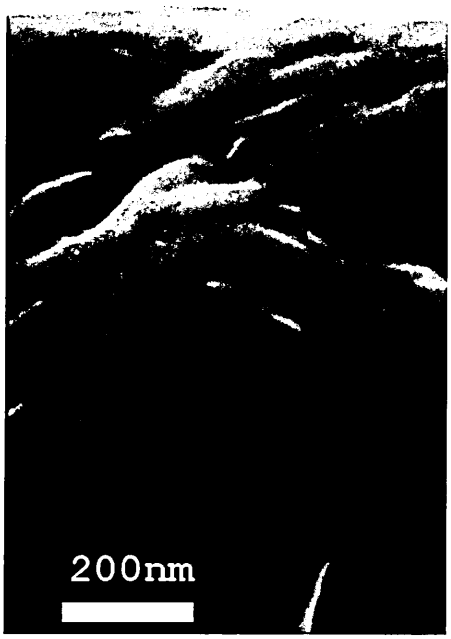


**Figure 4.22:** Cross-section of a corner of a via coated by 4000 W ICIS at a pressure of 13 Pa

In figure 4.22 a pronounced change to the microstructure is recognisable for an RF-power setting of 4000 W. There are no distinguishable grain boundaries identifiable in the dense microstructure. The deposition rate rose marginally to 210 nm $h^{-1}$.

Coating growth was at an oblique angle from the top edge of the via until the opening was fully covered. For an aspect ratio of 1:3, the via opening was covered after approx. 40 min. The sidewalls and bottom were coated evenly while the via was open and the coating thickness is in the range of 5-10 % of the top cover.

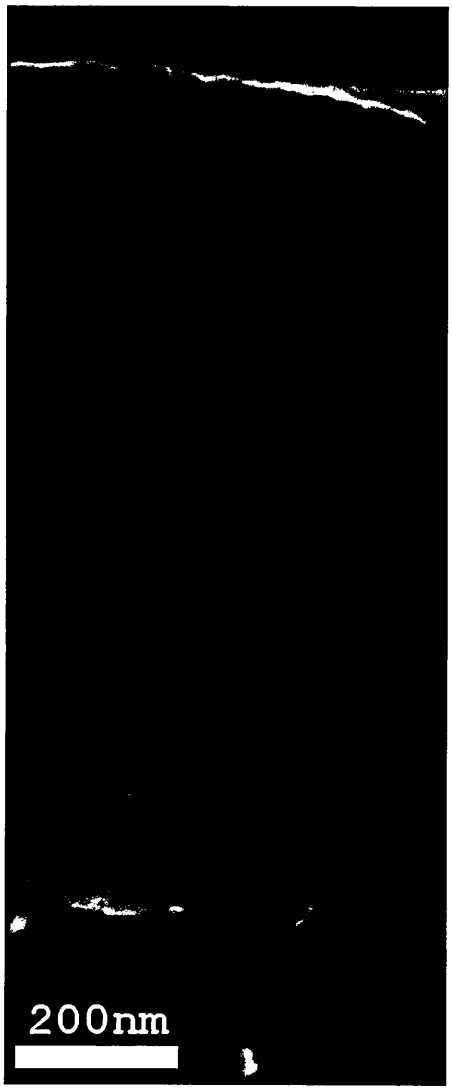


**Figure 4.23:** Cross-section of a corner of a via coated by 4000 W ICIS at a pressure of 6 Pa

When the pressure is reduced to 6 Pa at an RF-power of 4000 W, the microstructure

changes to dense columnar (fig.4.23). The deposition rate increases to 360 nm $h^{-1}$. The opening of the via is closed fully after 60 min. From the edge of the via the coating growth is at an oblique angle. After the columns from the edge meet and close the via, the columns then grow vertically as from the substrate top surface.

### Summary of Cu Coating Investigations

Successful deposition of pure Cu coatings by ICIS has been demonstrated. Analysis of the coating by SEM has revealed a number of promising features for the microstructure, as well as for the coating of high aspect ratio features on a substrate. The microstructure exhibits increased densification of the coatings for increasing applied RF-power from dense columnar to the very dense feature reduced coating as in fig.4.22. This change can be attributed to the higher ionisation of the metal flux and the resulting increased adatom mobility. The microstructure is comparable to zone 2 for the 2000 W and 3000 W coatings, the 4000 W sample is in between zones 2 and 3 compared to the microstructure models. Perpendicular film growth over the whole length of the sidewalls in via shows that the majority of the deposition flux is ionised, as only ions can follow the electric field lines and act perpendicular to the surface. The floor and sharp angles to the sidewalls of the via are also covered uniformly suggesting resputtering inside the feature. Material build up at the edge of the via is not present for ratios larger than 1:2. Increased thickening of material protruding into the via appears with increasing film thickness, attenuating towards

the bottom of the via. Edge rounding at the top of the coating is caused by highly energetic ions resputtering any material build up. For low deposition rates, this effect helps to keep the via open for the process time. The deposition rate for 2000 W applied RF-power is $120\,\mathrm{nm\,h^{-1}}$ increasing to $200\,\mathrm{nm\,h^{-1}}$ for 3000 W, due to increased ionisation of the process gas increasing the sputter rate. Film growth at 4000 W only increases marginally to $210\,\mathrm{nm\,h^{-1}}$ , yet the density of the film increases substantially. This may be caused by gas rarefaction reducing the sputter rate and, as the plasma source is above the target surface, allowing for the majority of the added power to increase the ionisation of the flux of sputtered material. When reducing the pressure to 6 Pa, the deposition rate increases to $360\,\mathrm{nm\,h^{-1}}$ and the coating structure is dense columnar. The change in microstructure may be an effect of the increased mean free path leading to a reduction in collisions and reduced ionisation fraction. The higher deposition rate can also be attributed to the increased mean free path.

### 4.3.2 Titanium Coatings by ICIS

From preliminary experiments it was calculated that to achieve a coating of 200 nm thickness, the process time needs to be 300 min. Apart from the deposition time, the process parameters were identical with the previous Cu coatings to be able to additionally compare how the same settings affect a different material. The base pressure was in the range of $4 \times 10^{-4}$ Pa. Three coatings were deposited at an applied RF-power of 2000 W, 3000 W and 4000 W respectively, at a constant pressure of 13 Pa, to examine the effect of power on the microstructure. A fourth coating was deposited at a power of 4000 W and a pressure of 6 Pa to investigate the effect of process pressure. The pulse parameters were a frequency of 500 Hz and a pulse width of 150 µs. The settings of the pulsed DC bias on the target remain constant at 1900 V.

The first coating deposited at 2000 W exhibits preferential deposition in large globular structures (fig. 4.24), creating a rough surface with dense coating inbetween . The deposition rate was 21 nm $h^{-1}$ measured in the preferred growth regions. Film growth on the sidewalls is perpendicular and the coating thickness reduces until the half-way point for an aspect ratio of 1:3. For the lower half of the via, the coating has a uniform thickness over the sidewalls and bottom.

The structure is dense globular and even for an RF-power of 3000 W. As can be seen in fig. 4.25, the sidewall and bottom coverage is continuous and there is no deposited

material build-up protruding into the via for an aspect ratio of 1:1.6. There are some large material build-ups over the surface of the sample. The deposition rate was $14\,\mathrm{nm\,h^{-1}}$

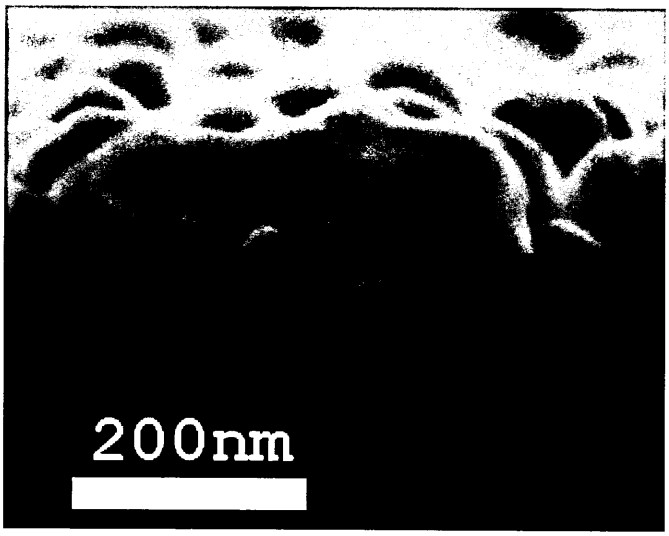


**Figure 4.24:** Cross-section of a corner of a via coated by 2000 W ICIS at a pressure of 13 Pa

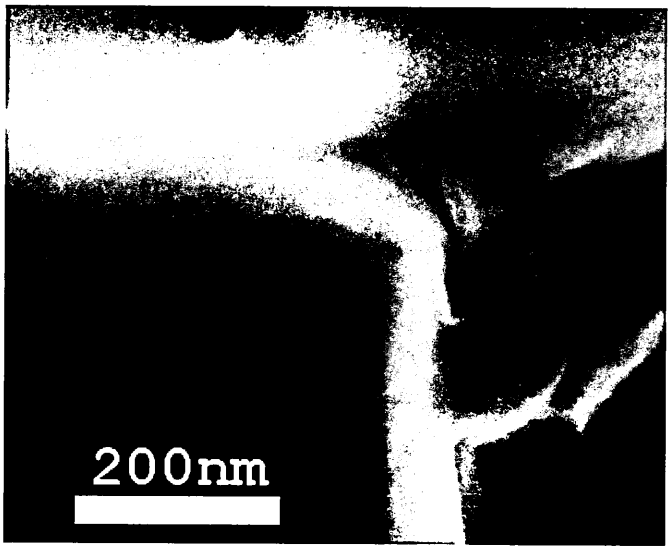


**Figure 4.25:** Cross-section of a corner of a via coated by 3000 W ICIS at a pressure of 13 Pa

For a pressure of 13 Pa and an RF-power of 4000 W, the Ti coating is deposited at a rate of 24 nm $h^{-1}$ (fig. 4.26). The microstructure is dense with no distinct grain boundaries and a very rough surface caused by large preferentially deposited globules, which do not protrude the top of the coating significantly. The coverage of the sidewalls is even and there is no further protruding of material at the top of the via.

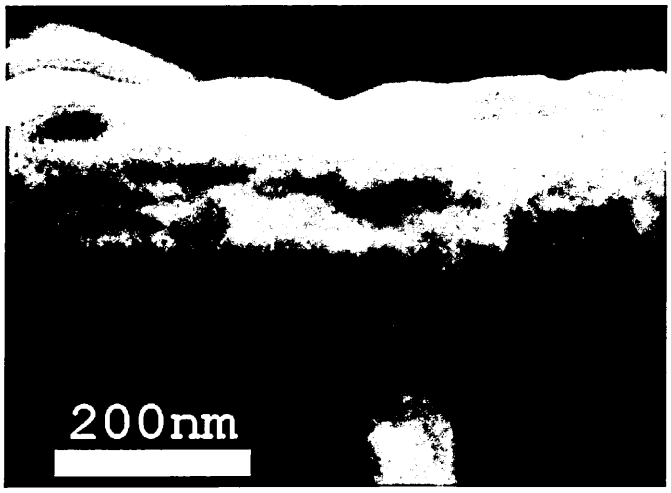


**Figure 4.26:** Cross-section of a corner of a via coated by 4000 W ICIS at a pressure of 13 Pa

As can be seen in fig.4.27, for the reduced pressure of 6 Pa, the microstructure is dense globular. Similarly to the 2000 W deposited sample, the surface is very rough due to areas of preferential growth. The sidewall and bottom coverage is uniform, with some directional growth at an oblique angle. As can be expected, the deposition rate increases approx. threefold to 68 nm $h^{-1}$ compared to the 4000 W power setting. This is due to fewer collisions as the mean free path is extended.


**Figure 4.27:** Cross-section of a corner of a via coated by 4000 W ICIS at a pressure of 6 Pa

### Summary of Ti Coating Investigations

Titanium has been coated onto high aspect ratio via. There are no changes in the microstructure or densification by changing power or pressure. Deposition rates are lower than expected compared to results from preliminary experiments. For increasing applied RF-power, the deposition rates are in the range of $20\,\mathrm{nm\,h^{-1}}$ at a constant pressure of 13 Pa, increasing to $68\,\mathrm{nm\,h^{-1}}$ at the lower pressure of 6 Pa. It was observed that the RF-coil is coated by target material during the process. As the

preliminary experiments were conducted using a coil that had been used for several hours of Ti ICIS processes, it is possible that initially more material is deposited until the coil is fully coated by target material. Once a certain level of coating is achieved, the net deposition may be counteracted by resputtering from the coil and as such increasing the deposition rate on the substrate. The rate increase at low pressure can be related to the reduced mean free path allowing particles to travel further before colliding. The coatings all feature dense globular structure which corresponds to zone 2 in the models. Via show uniform coating deposition on side walls attenuating with increasing depth as well as uniform via bottom coating, with no build up at the edges caused by resputtering of material. Further experiments need to be conducted to investigate why the deposition rate for Ti is low.

## 4.4 Nickel Coatings by ICIS

In this section, the results of the sputtering of pure Ni by ICIS, which have been published in the paper "Nickel coatings by Inductively Coupled Impulse Sputtering (ICIS)" [101], are presented. The aim is the first sputtering of ferromagnetic material by ICIS and the analysis of the plasma and the coating. For these experiments, we used the OES results for the modelling calculations, measured the IEDF by mass-spectrometry, analysed the microstructure and coverage of the substrate by SEM and correlated the emission data to the coating properties. For magnetic property measurements by MOKE, the samples were sent to the University of Lisbon.

### 4.4.1 Plasma Emission Results

Optical spectra for an ICIS 3000 W Ni plasma in Fig. 4.28 show strong emission from Ni neutrals. Ni ions were found on the only strong emission line in the visible spectrum, at a wavelength of 333.188 nm. This line is a convolution of the 333.103 nm and 333.287 nm lines, which have similar weighted oscillator strengths of 0.163 and 0.138 respectively, calculated with values from Ochsenbein et.al. [100]. Most Ni ions can be expected to emit at lower wavelengths in the ultraviolet spectrum. Additional experiments were conducted by mass- and energy- resolved spectroscopy to detect these, as discussed separately in section 4.4.4.

### 4.4.2 Influence of Applied RF-Power on Ionisation and Modelling

Fig. 4.29 shows measured OES intensities against RF-coil power in a log-log graph for the ICIS of Ni plasma. From the slope of excited Ar we obtain an exponent $\beta$=0.34, which is approx. half the value of the Ar emission from the 4p level for RF-MS [84] and one third of the value reported for DC-MS [85].

The slopes for excited Ar and Ni neutrals (Table 4.6 contains the observed gas and metal species) fit the model very well, with the Ni I intensity rising with a factor of 2 faster compared with Ar I. The only deviation from the model is the saturation of Ni I intensity for RF-power settings above 3000 W. For Ni ions the slope of the log intensity is three times the slope of Ar I for RF-power settings below 3000 W. This is consistent with excitation by electron collisions and ionisation by either electron

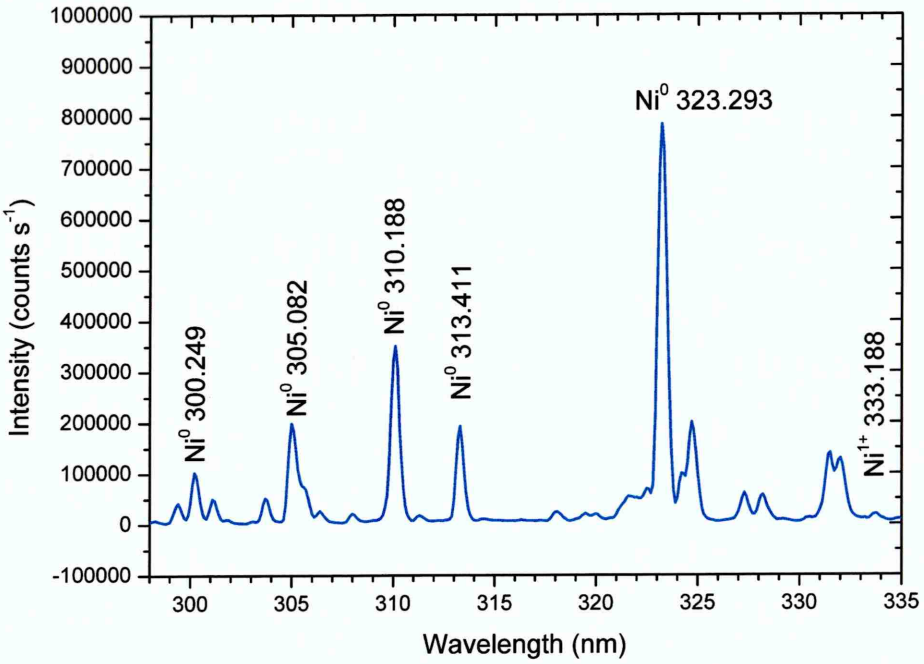


**Figure 4.28:** OES graph of the emission intensity of nickel in ICIS plasma. Clearly visible are the high intensity Ni neutral lines. Ni ion line is the strongest line in the visible spectrum. Applied RF-power was 3000 W.

or Ar* metastable collisions, as described by the used model. Several factors could be the cause for the deviation from the model, such as increased ionisation efficiency for powers above 3000 W by Penning ionisation, a reduction of the mean free path and higher electron temperatures.

The ion to neutral ratio in Fig. 4.30 for increasing RF-power at a constant pressure, shows a doubling of the ratio from 2000 W to 4000 W. This means that the influence of ions on the coating will change largely in this regime. Especially for deposition into high AR vias, the higher ion to neutral ratio is known to enable a better coverage

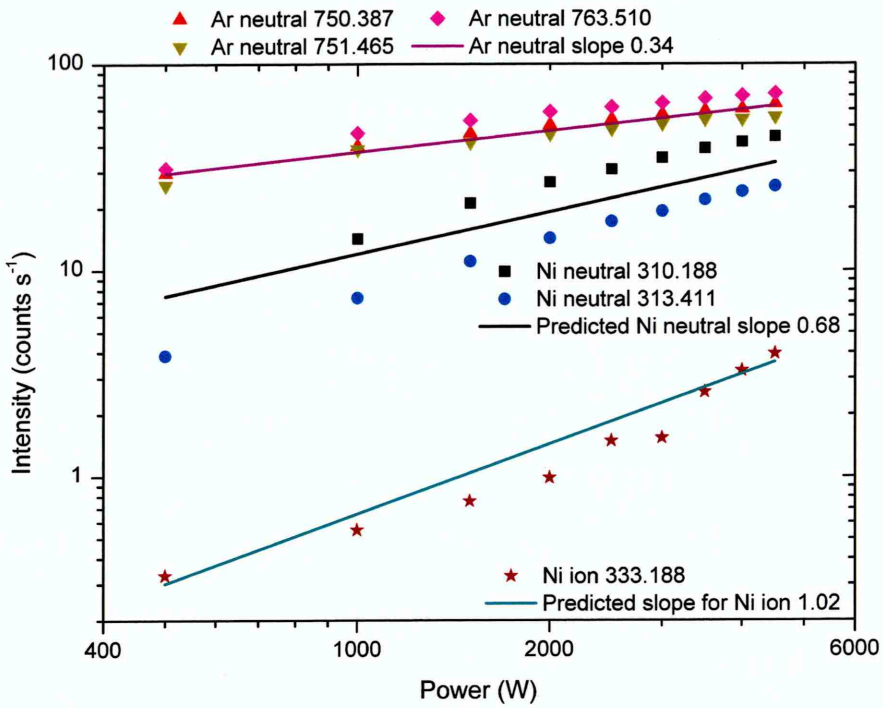


**Figure 4.29:** Measured results for Ar and Ni neutrals for a constant pressure of 12 Pa with varying RF-power.

and film growth on sidewalls and bottom. For AR larger than 3:1 the deposition on the bottom of the via is mainly by ions, as has been shown by Rossnagel [71]. The higher ratio of ions to neutrals also allows for denser coatings with metal ions being more efficient than gas [60].

**Table 4.6:** List of observed gas and metal species data and observed and predicted slope values of intensity-power modelling

| Species | Wavelength(nm) | Osc. Strength | Slope | |
|---|---|---|---|---|
| | | | observed | predicted |
| Ar I | 750.387 | 0.339 | 0.34 | - |
| Ar I | 751.465 | 0.316 | 0.33 | 0.34 |
| Ar I | 763.511 | 1.047 | 0.36 | 0.34 |
| Ni I | 310.188 | 0.568 | 0.78 | 0.68 |
| Ni I | 313.411 | 0.533 | 0.87 | 0.68 |
| Ni II | 333.188 | 0.163-0.138 | 1.12 | 1.02 |

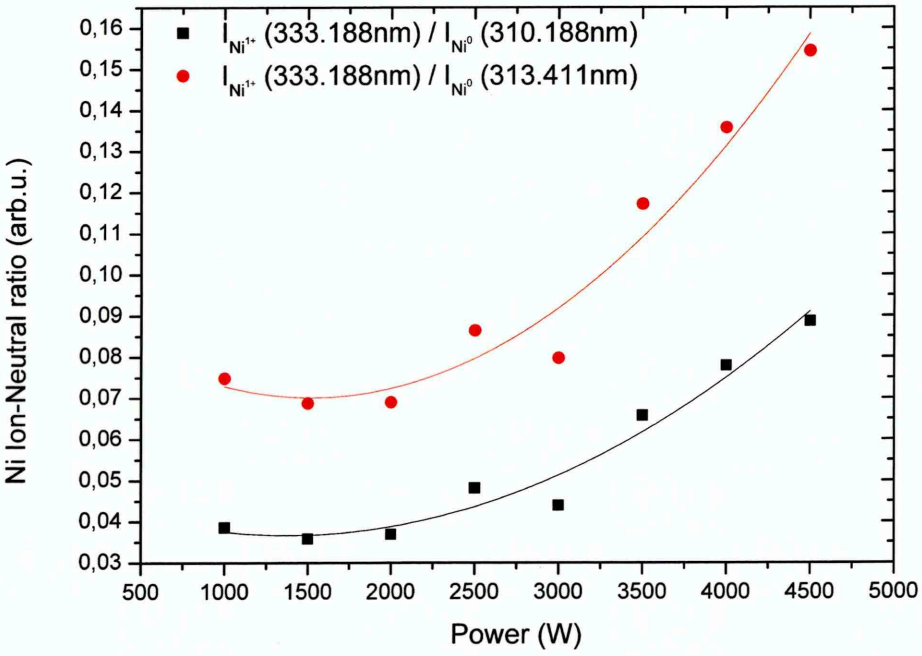


**Figure 4.30:** Ion-to-neutral ratio of ICIS Ni plasma for increasing RF-power at constant process pressure. Emission lines used were: Ni II at 333.188 nm, Ni I at 310.188 nm and Ni I at 313.411 nm.

### 4.4.3 Influence of Process Pressure on Ionisation

Figure 4.31 describes the influence of pressure on the ionisation at a constant power of 3000 W. For pressures below 10 Pa, there is a linear intensity increase for all gas and metal species.

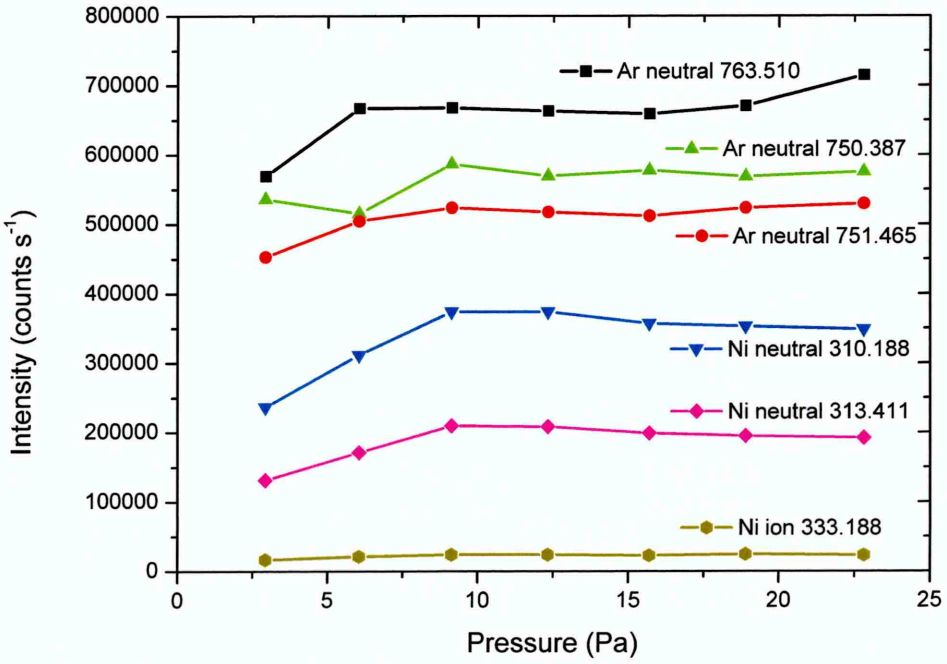


**Figure 4.31:** Measured results for Ar and Ni neutrals for a constant RF-power of 3000 W and varying pressure.

For pressures of 10-20 Pa, the Ar neutral intensity remains constant, while the Ni neutral intensity decreases between 10 Pa and 15 Pa, remaining constant for pressures up to 26 Pa. Ni ion intensity remains constant for all pressures above 10 Pa. This is also confirmed by the ion to neutral ratio plot in Fig. 4.32, where there is no change

in the ratio. This could be due to the constant RF-power that is not sufficient to allow further excitation or ionisation of metal species at pressures higher than 10 Pa.

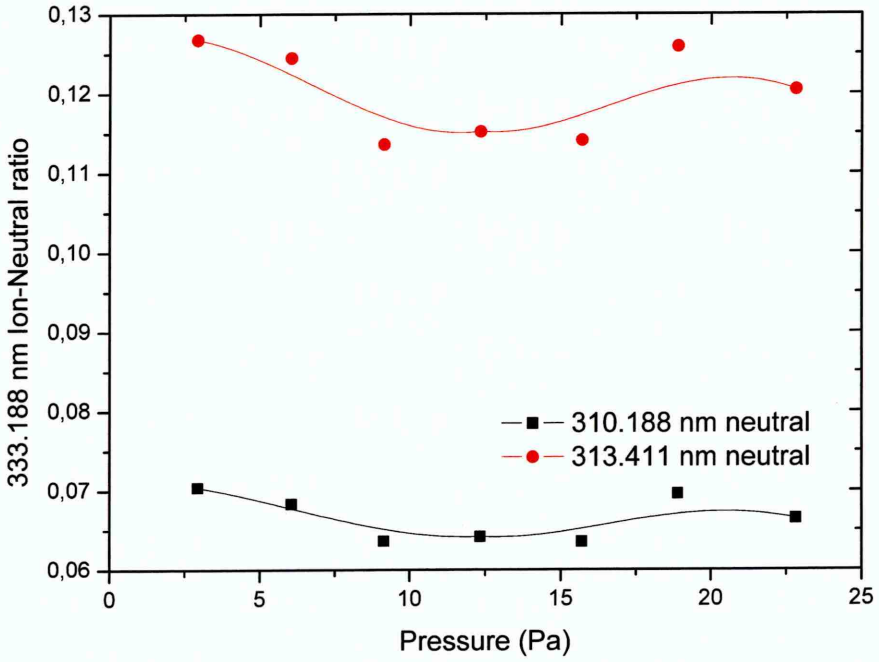


**Figure 4.32:** Ion-to-neutral emission ratio of ICIS Ni plasma for constant power and increasing pressure. Emission lines used were: Ni II at 333.188 nm, Ni I at 310.188 nm and Ni I at 313.411nm.

### 4.4.4 Mass and Energy Resolved Spectroscopy

The energy of impinging ions on the surface of the substrate is an important factor in densifying the structure of the film [60]. For magnetic materials, where the domain size is approx. 50 nm, to achieve bulk material properties in a thin coating it could be beneficial to promote densification of the coating. Fig. 4.32 shows the measurement for Ni II and Ar II ions at 3000 W and 13 Pa.

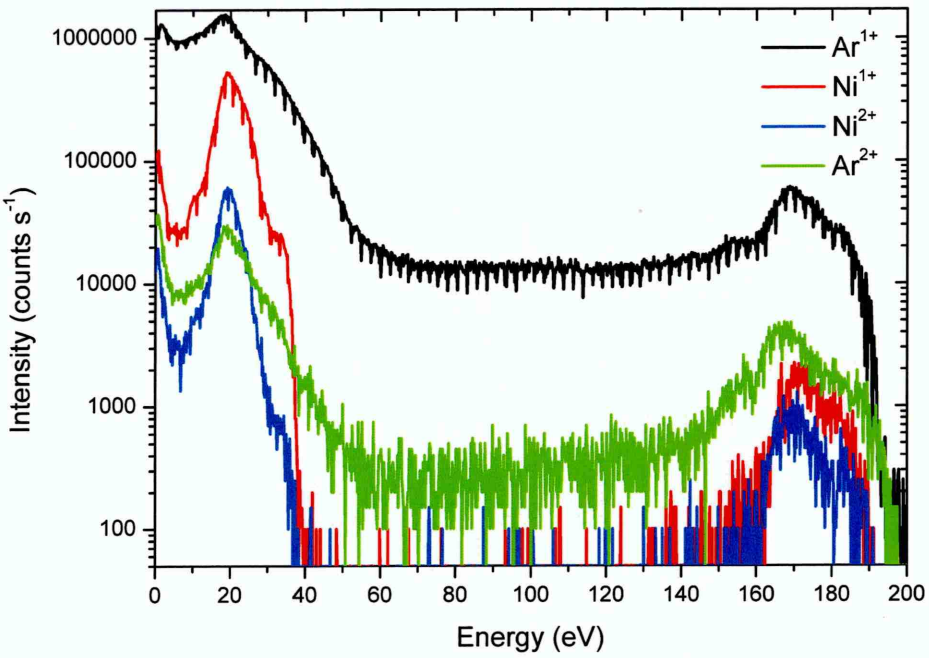


**Figure 4.33:** Ni ion energy distribution for a ICIS plasma. 20 eV is an ideal energy level for increased surface mobility and reduced lattice defects. A second, lower intensity peak is at 170 eV. The double charge of the ion has not been considered in the energy axis.

The energy distribution follows a non-Maxwellian distribution with a narrow ion energy bandwidth. The highest intensity peak energy is 20 eV, which corresponds to the plasma potential. This energy has been found to be an ideal level for ion surface mobility without inducing lattice defects. This low energy level and high ion to neutral ratio make it suitable for production of dense coatings [60]. A further lower intensity peak is visible at 170 eV, corresponding to high energetic ions which can also found be in pulsed plasmas [102]. To determine the origin of these energetic ions, further work is necessary, which lies outside the scope of this thesis.

### 4.4.5 Coating Properties

For the examination of the coating properties, Ni was deposited for a range of power and pressure settings from the power-pressure matrix developed for the plasma study in sections 4.4.1 and 4.4.3. From the plasma study it was concluded that a pressure of approx. 14 Pa would be sufficiently high to study the influence of power on the coating, as the influence of pressure on the plasma does not change significantly above 10 Pa. Power settings of 2000 W, 3000 W and 4000 W applied peak RF-power were chosen to evaluate the influence of power.

Fig. 4.34 shows the cross section of the coating deposited at 2000 W RF-power in a via with an aspect ratio (AR) of 3:1. A dense globular microstructure can be observed near the surface. A good sidewall and bottom coverage are visible. The accumulation of material at the bottom of the structure indicates deposition by ions as also reported by Rossnagel [2]. The overall distribution of the deposit indicates that the majority of the deposited species were metal ions. The dense structure of the bottom coating and no visible separation between the sidewall and bottom, as well as the even sidewall coverage, suggest only modest resputtering from the bottom of the via.

Figures 4.35 (3000 W RF-power) and 4.36 (4000 W RF-power) exhibit the same features of the coating on the substrate surface, as well as on the sidewalls and bottom of the via. However, as can be seen from the insets, the microstructure changes

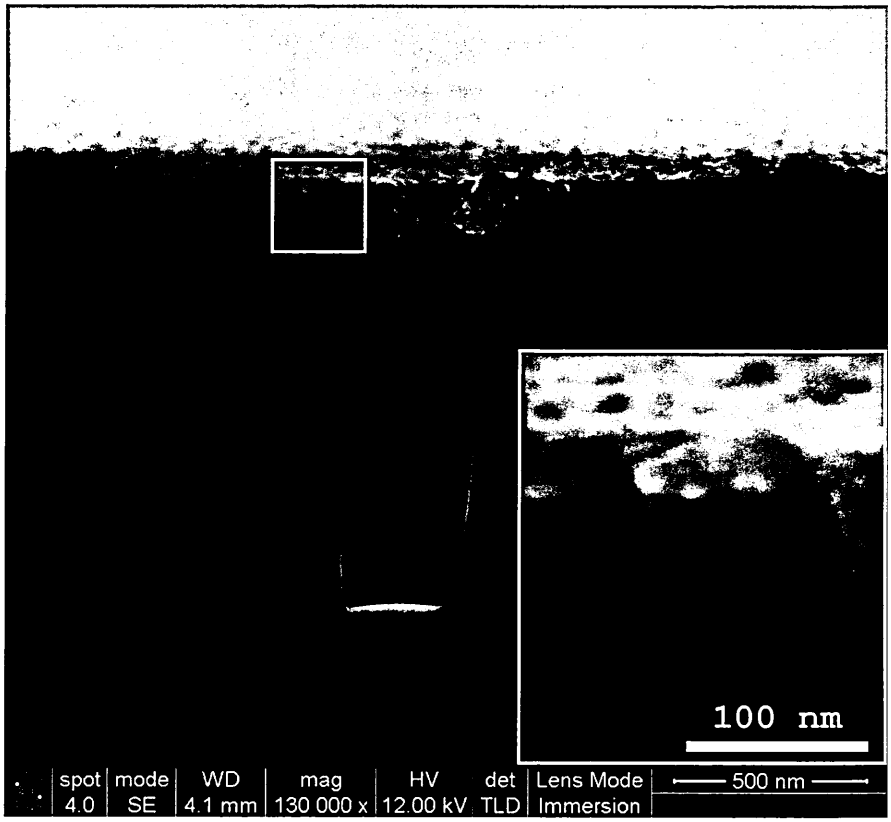


**Figure 4.34:** SEM cross-section of Ni coated via with an AR of 3:1. Deposition parameters 2000 W applied RF-power in ICIS plasma, process pressure 14 Pa. The insert shows magnified image of the coating exhibiting dense globular structure. Deposition rate is 40 nm/h.

with increasing applied RF-power. The grain size reduces and grain boundaries are obscured resulting in a denser coating microstructure. This is consistent with an increased ionisation rate of the deposition flux (figure 4.32), which provides adatoms with high energy and long diffusion paths on the surface of the growing film.

The influence of pressure on the coating morphology at a constant power setting of 4000 W RF-power can be seen when comparing fig.4.36 and fig. 4.37. Fig.4.37 shows a cross-sectional SEM image of a via with an AR of 2:1 at low pressure (6.4 Pa).

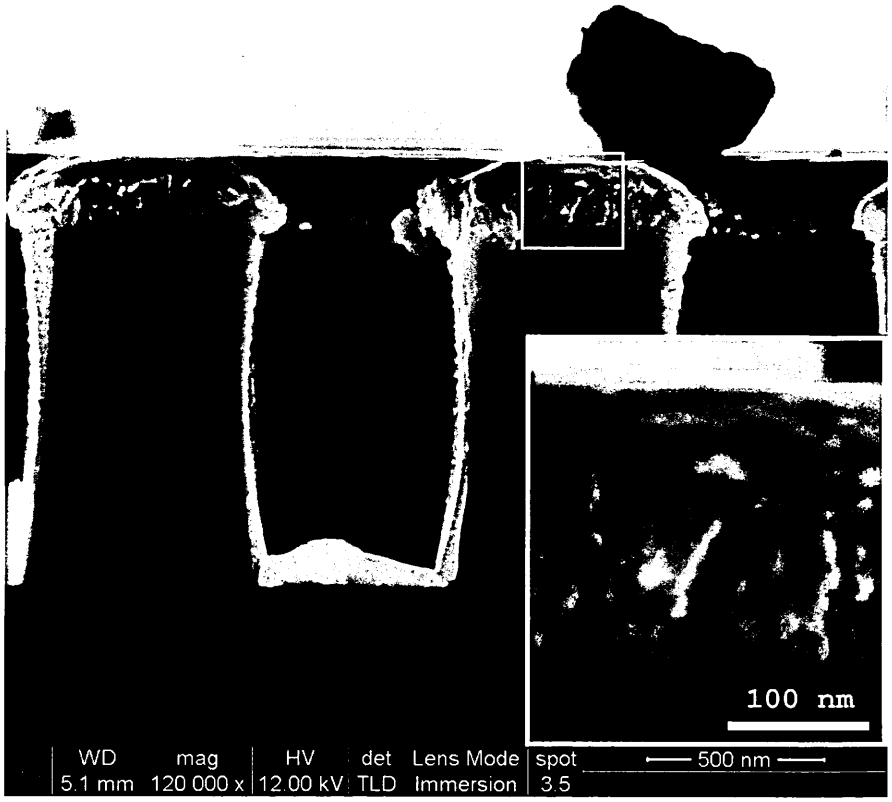


**Figure 4.35:** SEM cross-section of Ni coated via with an AR of 2:1. Deposition parameters 3000 W applied RF-power in ICIS plasma, process pressure 14 Pa. The insert shows the magnified image of the coating showing dense globular structure, but with a smaller feature size than with 2000 W applied RF-power. Deposition rate is 50 nm/h.

These conditions result in a medium ionisation degree of the sputtered material. The films exhibit dense columnar dendritic growth. Similar results for the microstructure have been shown by Linnik et.al. [103], albeit these coatings were deposited in a $N_2$ atmosphere and as such have reduced magnetic properties compared to pure Ni coatings. For the above mentioned process settings and AR, the BC is 21.2 %. The coating deposited at the higher pressure of 14 Pa exhibits a denser globular structure (fig.4.36). The factor 2 increase in pressure resulted in a factor of 2.5

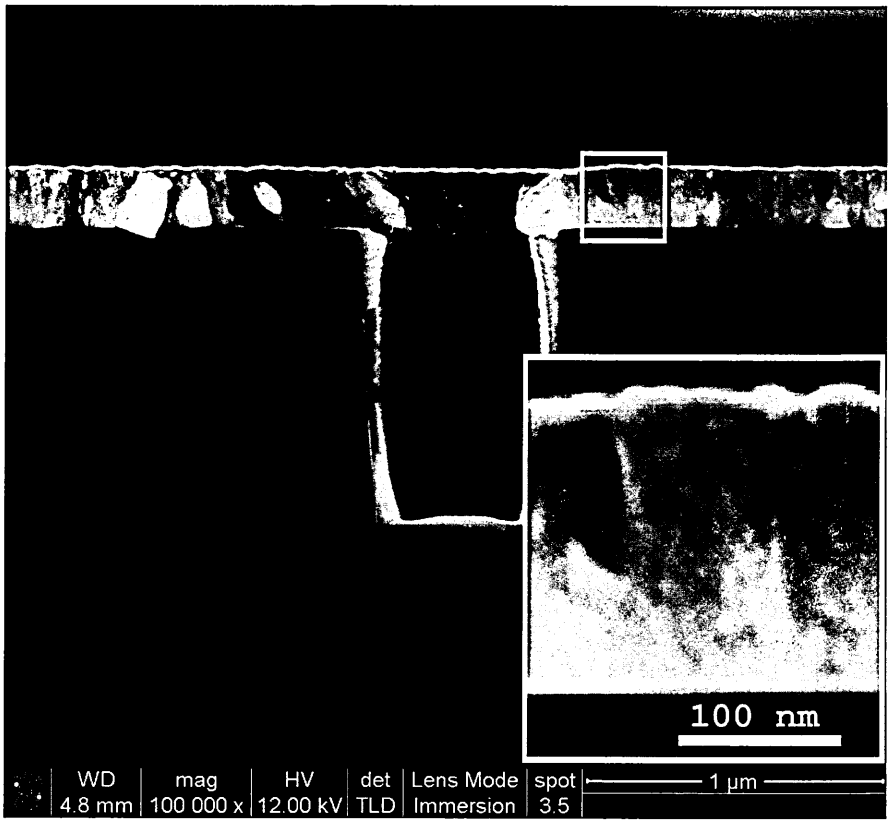


**Figure 4.36:** SEM cross-section of Ni coated via with an AR of 2:1. Deposition parameters 4000 W, applied RF-power in ICIS plasma, process pressure 14 Pa. The insert shows the magnified image of the coating showing dense globular structure, but with a smaller feature size than with 3000 W applied RF-power. Deposition rate is 45 nm/h.

reduced deposition rate, due to increased elastic scattering of the depositing species by the process gas and reduced diffusion rate. Generally, increasing the pressure causes collisional thermalisation of the depositing species, reduction of their energy and mobility on the surface of the growing film resulting typically in a reduced coating density.

Close-up images of the whole length of the via of the samples coated at 4000 W applied RF-power with pressure settings of 14.3 Pa (Fig. 4.38) and 6.4 Pa (Fig. 4.39),

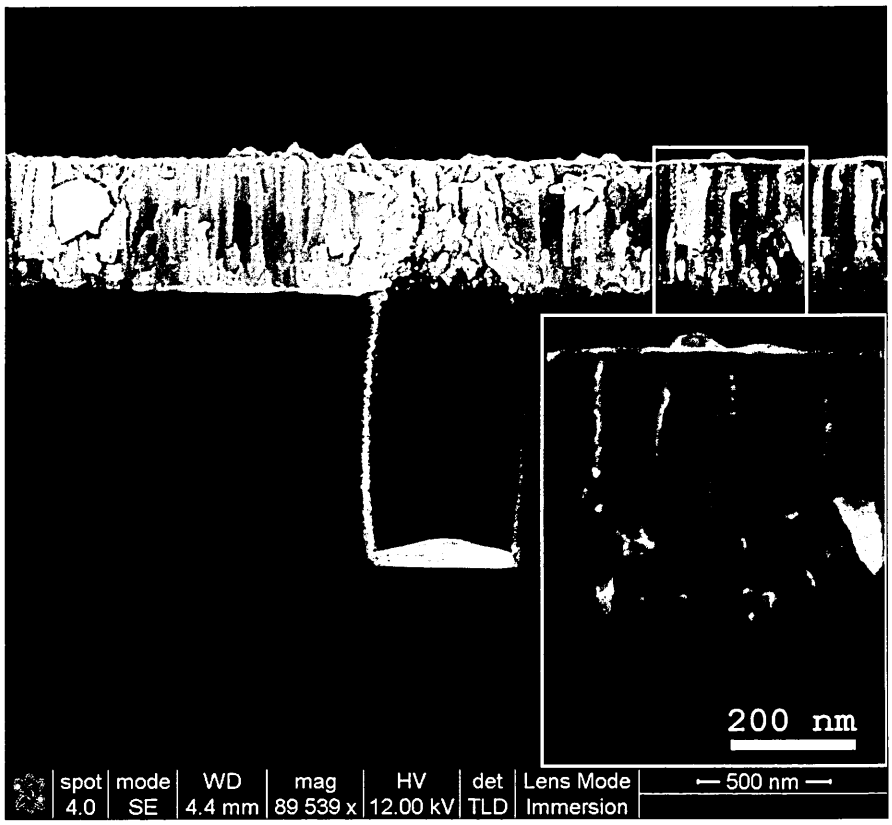


**Figure 4.37:** SEM cross-section of Ni coated high aspect ratio vias deposited with 4000 W RF-Power at 6.4 Pa. The dense columnar structure with dendritic features can be seen. The insert shows the magnified coating structure.

clearly show that the growth of columns on the sidewalls is mostly perpendicular to the substrate surface and homogeneously level over the whole length of the sidewall of the feature. To understand the effect of pressure on morphology we analyse the fluxes of species to the growing film. The gas ion is likely to be unaffected by pressure, as they are created mainly by electron impact which is related to the density of plasma and RF power. This is supported by the constant emission of Ar I (Figure 4.31). At the same time the deposition flux to the substrate is reduced significantly due to scattering. These two effects amount to an elevated gas ion-to-metal neutral ratio

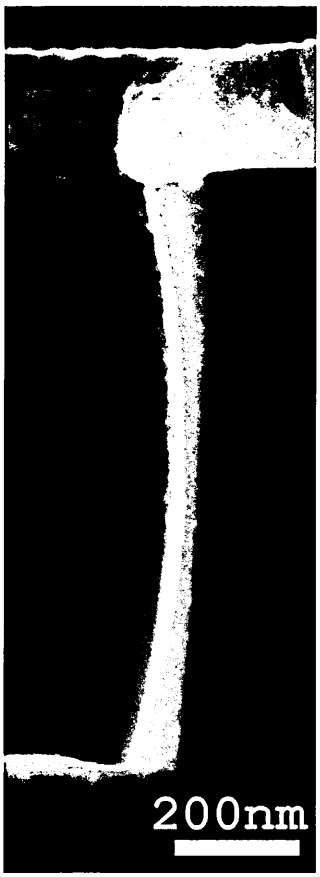


**Figure 4.38:** Close-up of the corner of the via from figure 4.35 (deposition at 14 Pa) showing dense globular growth of the Ni coating. Sidewalls and bottom of the via are evenly coated indicating high metal ionisation and modest resputtering from bottom

with pressure and result in enhanced mobility and densification of the microstructure at higher pressures. This is supported by the significantly better sidewall coverage for the 14.3 Pa film visible in fig.4.38. The open top of the via is consistent with gas-induced resputtering at the corner. The increase in ion-to-neutral ratio also drives a shift in the growth mode of the film on the surface from well-defined columnar to dense globular. In comparison, at the lower ion-to-neutral ratio (fig.4.39) the growth is typical of zone 2 of the Thornton structure zone diagram, where columns


**Figure 4.39:** Close-up of the corner of the via from figure 4.37 (6.4 Pa). Dendritic growth of the Ni coating can be seen along with the perpendicular growth on the sidewalls.

are enlarged and have dense grain boundaries. The column width at the bottom is similar to the width at the top, indicating that the texture selection is complete. At the interface the grain size is already large, indicating that nucleation sites coalesce into larger domains where subsequent growth is not competitive, therefore leading to fast establishment of texture and dense morphology of the film. For the higher pressure of 14.3 Pa, the microstructure seems to be shifting towards the dense Zone T of the Thornton model.

No significant sputtering of the RF-coil was observed in these experiments. From Table 4.7, it can be seen that over process time the contamination by RF-coil

**Table 4.7:** Coating composition of a process series showing reduced contamination by RF-coil material or other impurities.

| Sequence | 1 (0h) | 2 (4h) | 3 (8h) |
|---|---|---|---|
| Power / Pressure | 4000 W / 14.1 Pa | 4000 W / 24.7 Pa | 3000 W / 14.3 Pa |
| Element | Weight % | Weight % | Weight % |
| Nickel | 90.30 | 94.58 | 100.00 |
| Indium | 6.34 | 5.42 | - |
| Copper | 3.37 | - | - |

material can be reduced to below the detection limit of SEM-EDX. Cu and indium (In) contaminants were detected as remnants from other deposition processes in the chamber. This can be related to an observed net deposition of target material on the coil during the process.

### 4.4.6 Magnetic Properties of the Coating

Magnetic properties of the films were measured by MOKE. MOKE hysteresis loops were obtained from measurements of the polarization angle of an He - Ne laser (wavelength 633 nm, power 0.5 mW and 1 mm beam diameter) in longitudinal geometry, where the magnetic field to the sample was applied in the film plane. As can be seen in fig. 4.40, all samples gave a MOKE typical hysteresis response. Fig. 4.40(a) shows a slightly different hysteresis curve with a slope in the intensity values above the coercivity values.

This sample has the highest Ni purity of the process series, as shown in table 4.7. Due to these features, this sample was compared to that of a standard 25 nm permalloy

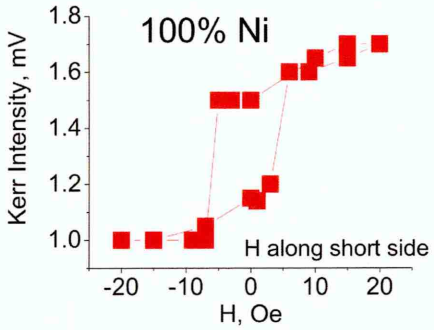


**(a)** Sample 1, 4000 W, 14.1 Pa.

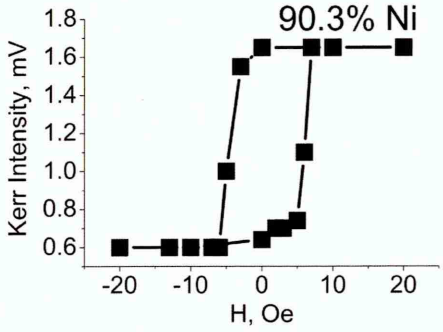


**(b)** Sample 2, 4000 W, 24.7 Pa

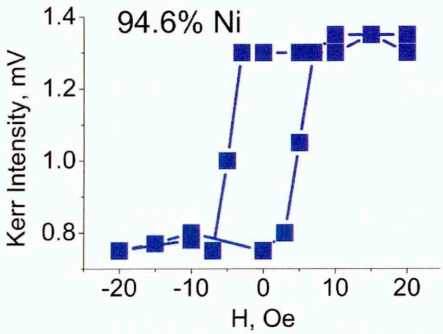


**(c)** Sample 3, 3000 W, 14.3 Pa.

**Figure 4.40:** Comparison of MOKE results for Samples 1, 2 and 3. As can be seen, samples 2 and 3 are similar,' while sample 1 has a slope in values above coercivity

(Py) (80 % Ni, 20 % Fe) film on glass substrate. Fig. 4.41 shows the comparison of the hysteresis loops of Ni and Py with the MOKE intensity of Ni being 1.2 times larger than that of Py and approx. doubled coercivity value of 6 Oe.

The MOKE response is the product of reflectivity and Kerr rotation [93]. With the

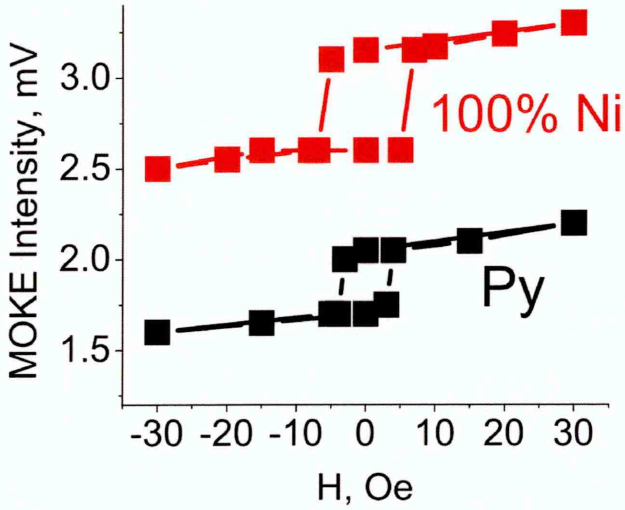


**Figure 4.41:** MOKE comparison of pure Ni coating with a standard reference sample of Py (80 % Ni, 20 % Fe).

Ni showing a MOKE response of 1.2 times larger than Py and the reflectivity of Py and Ni measured to be 0.5, the Kerr rotation of Ni is 0.6 times that of Py. The Kerr rotation is proportional to the magnetisation and for Py is well measured to be 10.0 kG, which is close to the calculated literature value of 9.5 kG [104]. For the Ni coating this corresponds to a magnetisation of 6.0 kG, which is close to the typical magnetisation of Ni in bulk form [104].

# CHAPTER 5

## Conclusions

In this chapter the conclusions of the experimental work are drawn and the scope for future work based on questions arising from the current work is given.

### Setting up the ICIS technology inside a Deposition System

The ICIS setup has been successfully transferred from an experimental system into a coating deposition system.

Significant changes between the ISIS setup in a coating deposition system compared the the existing experimental setup are the use of an internal RF-coil to generate the plasma and the use of an industry standard RF-power supply with a frequency of 13.56 MHz frequency supplying up to 5 kW of power to drive the coil. Initial issues with the plasma generation have been solved by using better ground connection and by connecting the the RF-power supply in order that the current flows in clockwise

direction through the coil towards ground. In this setup the field lines are directed towards the target accelerating Ar ions towards the target to initiate sputtering whereas if the current flows anti-clockwise the files lines are directed away from the target limiting the sputter yield. This was observed when utilising a small coil with more windings, here the glow discharge moved along the axis towards the target with clockwise current flow.

### Plasma Analysis

To gain knowledge of the plasma properties of the new ICIS discharge, analysis of the ICIS plasma has been conducted by measurement of the current and voltage waveforms in the coil, the optical emission and by plasma sampling mass spectrometry.

The current and voltage waveforms that have been measured in the coil, exhibit a sharp rise in the first 10 µs. After reaching the peak value, the waveforms reduce to a level that is sustained for the remainder of the pulse duration. This transient behaviour has been described by Guo and DeJoseph [73] to be a property of the power supply, as due to the rapidly changing plasma impedance the power supply is able to adapt the current and voltage fast enough to sustain a constant power output. This effect could be overcome by designing a specialist power supply for this process. For high RF-powers it is also necessary to adapt the pulse on-time, as the power supply is not able to sustain high power over prolonged pulse durations

and the current and voltage waveforms begin to oscillate. These oscillations effect the plasma generation to the effect of reducing the OES intensity to that of lower power levels. For this reason the RF-power setting has been limited to 4000 W at a pulse width of 150 µs in this work.

The charge increases linearly with the applied power indicating that the increased power is fully coupled into the plasma. Constant resistivity shows that the impedance of the plasma does not change during the pulse on-time. This indicates that the plasma remains predominantly inductive.

The optical emission results have been compared to a model which correlates the optical emission intensity to the applied RF-power. The resulting slope factor in a log-log graph gives an indication of the number of excitations steps, by electron collision, that were needed to excite the individual species to the current state. For the sputtering of titanium and nickel the results relate very well to the model. The slope of the exited argon intensity is used as the reference to which the increase in the slope is compared to. Here, for the metal neutrals the slope factor is a factor of 2 greater than the slope of excited argon. Further, the slope factors for the metal ions is a factor of 3 steeper than the exited argon slope. This indicates that the assumptions made in the modelling are a good representation of the actual plasma and the main excitation mechanism is by electron collisions. Copper neutral and ion slopes exhibit 2 different slope sections. While the Ar slope in the Cu process is comparable with the Ar slopes in the Ti and Ni processes, the first slope section up

to 1600 W for the Cu neutral is four times steeper than expected. Cu ion slopes are 7 times steeper than predicted by the model. This represents an increase in the range of a factor of 2, indicating an additional excitation process. The second slope section up to 4000 W, shows a linear increase with no correlation to the model expectation. Further investigations of this effect are necessary to establish the specific cause of this effect and why this only effects copper and not the other metals used in this study.

Mass spectroscopy measurements of Ni, Ti and Cu show three distinctive peaks. The first peak at 1 eV is from thermalised ions originating from the target and the coil. The second peak at 20 eV represents the plasma potential, and the third peak in the range of 130-180 eV represents higher energetic ions. These ions are created by ionisation in the coil. In addition to these general IEDF properties, there are differences in the IEDF for different materials with increasing power. Each material has characteristic changes in the shape of the peaks, such as varying peak widths or shifts in the energy range. The measured plasma potential results are comparable with other ICP processes which may also be caused by the higher process pressure and thus reduced mean free path of the excited material flux. However, the plasma potential is at an ideal level for the production of dense coatings while limiting lattice defects. This effect is particularly interesting for the deposition of very thin films.

### Effect of RF-Power and Pressure on the Microstructure of Cu and Ti Coatings

This work is first to examine the effects of applied RF-power and and the pressure on the microstructure of coatings deposited by ICIS. Copper coatings exhibit a highly dense columnar microstructure for power settings of up to 3000 W at a pressure of 13 Pa. For a power of 4000 W, the microstructure turns to fully dense with no distinguishing grain boundaries. Deposition rates of up to 210 $\mu m\,h^{-1}$ are achieved for these settings. For a power of 4000 W and a pressure of 6 Pa the microstructure is dense columnar and the deposition rate increases to 360 $\mu m\,h^{-1}$.

For titanium the deposition rate is very low (20 $\mu m\,h^{-1}$) for all power settings at a pressure setting of 13 Pa. The lower deposition rate of Ti in comparison to Cu cannot be linked directly to the different sputter yields. According to the NPL Ar sputter yield table [96], the sputter yield of Cu is 2.6 times higher than Ti. However, the actual deposition rate is 9 times lower than Cu. This may be attributed to a net deposition of target material on the RF-coil in the Ti and Ni processed while additional sputtering of coil material in the Cu process takes place. At a pressure of 6 Pa, the deposition rate rises to 68 $\mu m\,h^{-1}$. For the lower pressure the difference in deposition rate of Ti is half of the rate expected by the sputter yield.

The microstructure of the Ti coatings is dense globular, with a very uneven surface on the top side of the substrate, for all examined cases.

### Nickel Coatings by ICIS

The first sputtering of ferromagnetic material by ICIS has been demonstrated.

The plasma analysis conducted by OES is consistent with the modelling expectations. The slopes of the metal neutrals are a factor of 1 greater than the Ar slope, while the metal ion slope is three times as steep as Ar. In the range of 2000-4000 W at a constant pressure of 14.3 Pa, the ion-to-neutral ratio doubled. In this region the largest influence of increasing power on the ionisation and microstructure can be expected and Ni coatings were deposited at 2000 W, 3000 W and 4000 W.

The influence of increasing pressure was measured at a constant power of 3000 W. The greatest change in the intensity was measured in the range of 3-10 Pa. For pressures above 10 Pa, the intensity counts saturate for increasing pressure. This is also confirmed by a constant ion-to-neutral ratio for increasing pressure.

The IEDF exhibits a non-Maxwellian distribution, with 3 distinct peaks at 1 eV, 20 eV and 170 eV. Confirming the results from the non-magnetic materials and showing the plasma potential to be a function of the process and not of the material.

The microstructure of deposited coatings at a pressure of 14.3 Pa, exhibit a dense globular structure. The deposition rate is in the range of 50 nm, which is twice as fast as for Ti. This correlates very well with the sputter yield which is twice the Ti sputter yield [96]. Coating coverage of high aspect ratio features is even on sidewalls and bottom of the via. The coating deposited at 4000 W and 6.4 Pa exhibits a

dense columnar structure with perpendicular film growth on sidewalls. Deposition increases to $120\,\mu m\,h^{-1}$. Contamination by residual material in the chamber or the RF-coil was measured to be below the detection limit of the EDX, producing pure Ni coatings after four hours of Ni deposition.

The magnetisation, measured by MOKE, for the pure Ni coating deposited at 3000 W and 14.3 Pa is 10 kG. This is close to the literature value for bulk material.

These results show that sputtering of magnetic material with ICIS is comparable to non-magnetic material sputtering in terms of rate and ionisation. This makes ICIS a viable solution for the highly ionised sputtering of magnetic and non-magnetic coatings.

## Future Work

In this section the scope for future work is given based on questions that have arisen during the course of this research project.

- In this work the electron temperature has been estimated by the ion-to-neutral ratio of the metal. To determine the electron temperature and electron density, Langmuir probe measurements need to be conducted. Further, the measurement of the EEDF will be useful to model the excitation, especially of copper, more precisely.
- It will be useful to investigate measures of reducing the coating contamination by residual material or copper from the RF-coil assembly.
- As in the case of the varying properties of different non-magnetic materials, to gain a broader understanding of the sputtering of magnetic materials it will be useful to build a catalogue of magnetic material sputtering by ICIS e.g. Fe, Co and Sm.
- Further detailed investigations of the coating structure and composition by XRD, SIMS or Raman Spectroscopy.
- Further investigation of the anomalies in the sputtering of copper is needed to establish the deviation from the expected OES modelling results and the higher deposition rates compared to the sputter yield of Ti and Ni.

# References


1. ASMUSSEN J., JR., T.A. GROTJOHN, PENGUN MAK, and M.A. PERRIN: 'The design and application of electron cyclotron resonance discharges'. *Plasma Science, IEEE Transactions on* (Dec. 1997), vol. 25(6): pp. 1196–1221.
2. ROSSNAGEL, S. M. and J. HOPWOOD: 'Magnetron sputter deposition with high levels of metal ionization'. *Applied Physics Letters* (1993), vol. 63(24): pp. 3285–3287.
3. KOUZNETSOV, VLADIMIR, KAROL MACAK, JOCHEN M. SCHNEIDER, ULF HELMERSSON, and IVAN PETROV: 'A novel pulsed magnetron sputter technique utilizing very high target power densities'. *Surface and Coatings Technology* (1999), vol. 122(2-3): pp. 290–293.
4. EHIASARIAN, A. P., R. NEW, W. -D. MUENZ, L. HULTMAN, U. HELMERSSON, and V. KOUZNETSOV: 'Influence of high power densities on the composition of pulsed magnetron plasmas'. *Vacuum* (2002), vol. 65(2): pp. 147–154.
5. BOHLMARK, J.: 'Fundamentals of High Power Impulse Magnetron Sputtering'. PhD thesis. Linkoping University Institute of Technology, 2006.
6. HOPWOOD, J.: 'Ionized physical vapor deposition of integrated circuit interconnects'. *Phys. Plasmas* (1998), vol. 5(5): pp. 1624–1631.
7. ALAMI, J., P. O.Å. PERSSON, D. MUSIC, J. T. GUDMUNDSSON, J. BOHLMARK, and U. HELMERSSON: 'Ion-assisted physical vapor deposition for enhanced film properties on nonflat surfaces'. *Journal of Vacuum Science & Technology A* (2005), vol. 23(2): pp. 278–280.

8. LIM, JU-WAN, HEUNG-SIK PARK, TAE-HYEONG PARK, JUNG-JOONG LEE, and JUNGHOON JOO: 'Mechanical properties of titanium nitride coatings deposited by inductively coupled plasma assisted direct current magnetron sputtering'. *Journal of Vacuum Science & Technology A* (2000), vol. 18(2): pp. 524–528.

9. EHIASARIAN, A. P., W. -D. MUENZ, L. HULTMAN, U. HELMERSSON, and I. PETROV: 'High power pulsed magnetron sputtered CrNx films'. *Surface and Coatings Technology* (2003), vol. 163-164: pp. 267–272.

10. KELLY, P.J., P.M. BARKER, S. OSTOVARPOUR, M. RATOVA, G.T. WEST, I. IORDANOVA, and J.W. BRADLEY: 'Deposition of photocatalytic titania coatings on polymeric substrates by HiPIMS'. *Vacuum* (2012), vol. 86(12). cited By 7: pp. 1880–1882.

11. GIBBS, M. R. J., E. W. HILL, and P. J. WRIGHT: 'Magnetic materials for MEMS applications'. *Journal of Physics D: Applied Physics* (2004), vol. 37(22): R237.

12. GIBBS, M.R.J.: 'Materials Optimization for Magnetic MEMS'. *Magnetics, IEEE Transactions on* (June 2007), vol. 43(6): pp. 2666–2671.

13. SANDU, IZABELA, LIONEL PRESMANES, PIERRE ALPHONSE, and PHILIPPE TAILHADES: 'Nanostructured cobalt manganese ferrite thin films for gas sensor application'. *Thin Solid Films* (2006), vol. 495(1-2). {EMRS} 2005 Symposium E Synthesis, Characterization and Applications of Mesostructured Thin Layers: pp. 130–133.

14. GAU, J.-S.: 'Magnetic thin film devices'. *Materials Science and Engineering: B* (1989), vol. 3(4): pp. 377–381.

15. WHITE, R.M.: 'The materials aspect of magnetic recording'. *Journal of Magnetism and Magnetic Materials* (1990), vol. 88(12): pp. 165–176.

16. NIARCHOS, D: 'Magnetic MEMS: key issues and some applications'. *Sensors and Actuators A: Physical* (2003), vol. 109(12): pp. 166–173.

17. ROLL, K., R. KUKLA, M. MAYR, and W.D. MUNZ: 'High rate magnetron sputtering of ferromagnetic SmCo, Fe and CoCr thin films'. *Magnetics, IEEE Transactions on* (Jan. 1984), vol. 20(1): pp. 63–65.

18. WINDOW, B. and F. SHARPLES: 'Magnetron sputtering sources for ferromagnetic material'. *Journal of Vacuum Science & Technology A* (1985), vol. 3(1): pp. 10–13.

19. WIRZ, P.: *Magnetron cathode for sputtering ferromagnetic targets.* US Patent 4,601,806. July 1986.

20. MUSIL, J. and M. MIŠINA: 'Low pressure radio frequency and microwave discharges for d.c. sputtering of ferromagnetic materials'. English. *Czechoslovak Journal of Physics* (2000), vol. 50(6): pp. 785–794.

21. GALLANT, J.L. and P. DMYTRENKO: 'Targets with thin ferromagnetic layers for transient field experiments'. *Nuclear Instruments and Methods in Physics Research* (1982), vol. 200(1): pp. 127–128.

22. GUINIER, ANDRÉ and R. JULLIEN: *The Solid State From Superconductors to Superalloys.* Oxford University Press, 1989.

23. WILSON Richard W. (Phoenix, AZ): *Magnetion sputtering of ferromagnetic material.* June 1978.

24. GALDIKAS, ARVAIDAS and LIUDVIKAS PRANEVIEIUS: *Interactions of Ions with Condensed Matter.* Vol. 229. Horizons in World Physics. Nova Biomedical, 2000: p. 176.

25. YAMAKOSHI, Y. and R. SUZUKI: *Nickel alloy sputtering target and nickel alloy thin film.* US Patent 7,605,481. Oct. 2009.

26. YUKIMURA, K. and A. P. EHIASARIAN: 'Generation of RF plasma assisted high power pulsed sputtering glow discharge without using a magnetic field'. *Nuclear Instruments and Methods in Physics Research Section B: Beam Interactions with Materials and Atoms* (2009), vol. 267(8-9): pp. 1701–1704.

27. LOCHTE-HOLTGREVEN, W. and J. RICHTER: *Plasma diagnostics.* North-Holland Pub. Co., 1968.

28. NUMANO, M.: 'Transition electron density between the coronal and the thermal equilibrium in hydrogen plasmas'. *Journal of Quantitative Spectroscopy and Radiative Transfer* (1995), vol. 53(5): pp. 527–531.

29. DER VAN SIJDE, B., J. J. A. M. van der MULLEN, and D. C. SCHRAM: 'Collisional Radiative Models in Plasmas'. *Beiträge aus der Plasmaphysik* (1984), vol. 24(5): pp. 447–473.

30. MEHDI, T., P.B. LEGRAND, J.P. DAUCHOT, M. WAUTELET, and M. HECQ: 'Optical emission diagnostics of an rf magnetron sputtering discharge'. *Spectrochimica Acta Part B: Atomic Spectroscopy* (1993), vol. 48(8): pp. 1023–1033.

31. EISBERG, R. and R. RESNICK: *Quantum Physics of Atoms, Molecules, Solids, Nuclei and Particles.* 2nd. John Wiley & Sons Ltd., 1985.

32. CHAPMAN, B.: *Glow Discharge Processes, Sputtering and Plasma Etching.* JOHN WILEY & SONS, New York, Chichester, Brisbane, Toronto, Singapore, 1980.

33. MATTOX, DONALD M.: *The Foundations of Vacuum Coating Technology.* Noyes Publications, 2003.

34. MATTOX, DONALD M.: *Handbook of Physical Vapor Deposition (PVD) Processing (Second Edition).* Second Edition. Boston: William Andrew Publishing, 2010: pp. iv–.

35. CHAPIN, J.S.: 'The Planar Magnetron'. *Res./Develop.* (1974), vol. 25(1): pp. 37–40.

36. CHEN, FRANCIS F: *Introduction to Plasma Physics.* Plenum Press, 1974.

37. WINDOW, B. and N. SAVVIDES: 'Charged particle fluxes from planar magnetron sputtering sources'. *J. Vac. Sci. Technol.* (1986), vol. 4: pp. 196–202.

38. SPROUL, WILLIAM D.: 'Multi-cathode unbalanced magnetron sputtering systems'. *Surface and Coatings Technology* (1991), vol. 49(1-3): pp. 284–289.

39. HITTORF, W: 'Ueber die Electricitätsleitung der Gase'. *Annalen der Physik* (1884), vol. 257: pp. 90–139.

40. LIEBERMAN, MICHAEL A. and ALLAN J. LICHTENBERG: *Principles of Plasma Discharges and Materials Processing.* Wiley-Interscience, 2005.

41. HOPWOOD, J.: 'Review of inductively coupled plasmas for plasma processing'. *Plasma Sources Sci. Technol.* (1992), vol. 1(2): p. 109.

42. LISTER, G G: 'Low-pressure gas discharge modelling'. *J. Phys. D: Appl. Phys.* (1992), vol. 25: pp. 1649–1680.

43. YAMASHITA, M.: 'Fundamental characteristics of built-in high-frequency coil-type sputtering apparatus'. *Journal of Vacuum Science Technology A: Vacuum, Surfaces, and Films* (Mar. 1989), vol. 7(2): pp. 151–158.

44. ROSSNAGEL, S. M. and J. HOPWOOD: 'Metal ion deposition from ionized mangetron sputtering discharge'. *J. Vac. Sci. Technol.* (1994), vol. B 12: pp. 449–453.

45. GUDMUNDSSON, J T: 'Ionized physical vapor deposition (IPVD): magnetron sputtering discharges'. *Journal of Physics: Conference Series* (2008), vol. 100(8): p. 082002.

46. HELMERSSON, U., M. LATTEMANN, J. BOHLMARK, EHIASARIAN A. P., and GUDMUNDSSON J. T.: 'Ionized physical vapor deposition (IPVD): A review of technology and applications'. *Thin Solid Films* (2006), vol. 513(1-2): pp. 1–24.

47. MOZGRIN, D.V., I.K. FETISOV, and G.V. KHODACHENKO: 'High Current Low-Pressure Quasi-Stationary Discharge in a Magnetic Field: Experimental Research'. *Plasma Physics Reports* (1995), vol. 21: pp. 400–409.

48. MACAK, K., V. KOUZNETSOV, J. SCHNEIDER, U. HELMERSSON, and I. PETROV: 'Ionized sputter deposition using an extremely high plasma density pulsed magnetron discharge'. *J. Vac. Sci. Technol.* (2000), vol. 18(4): pp. 1533–1537.

49. ANDERS, ANDRÉ: 'Fundamentals of pulsed plasmas for materials processing'. *Surface and Coatings Technology* (2004), vol. 183(2-3): pp. 301–311.

50. EHIASARIAN, A. P., P. EH. HOVSEPIAN, and K. YUKIMURA: 'Rf-plasma glow discharge sputtering'. WO Patent App. PCT/GB2010/050,641. Oct. 2010.

51. YUKIMURA, K., H. OGISO, S. NAKANO, and A.P. EHIASARIAN: 'High-Power Inductively Coupled Impulse Sputtering Glow Plasma'. *Plasma Science, IEEE Transactions on* (Nov. 2011), vol. 39(11): pp. 3085–3094.

52. MALKIN, O.A.: 'Pulsed current and relaxation in gas'. *ATOMIZDAT (in Russian)* (1974), vol.: pp. 27–39.

53. BARNA, P.B.: 'Diagnostics and Applications of Thin Films'. Ed. by ECKERTOVA, L. and T. RUZICKA. IOP Publishing, 1992: p. 295.

54. MOVCHAN, A. and A.V. DEMCHISHIN: 'Investigations of the structure and properties of thick Ni, Ti, W, Al2O3 and ZrO2 vacuum condensates'. *Fiz. Metal. Metalloved.* (1969), vol. 28: pp. 83–90.

55. KRANENBURG, HERMA van and COCK LODDER: 'Tailoring growth and local composition by oblique-incidence deposition: a review and new experimental dat'. *Materials Science & Engineering* (1994), vol. R11: pp. 295–354.

56. THORNTON, JOHN A.: 'Influence of apparatus geometry and deposition conditions on the structure and topography of thick sputtered coatings'. *Journal of Vacuum Science & Technology* (1974), vol. 11(4): pp. 666–670.

57. MIT OpenCourseWare. URL: `http://www.flickriver.com/%5C%5Cphotos/mitopencourseware/4153138383/`.

58. MESSIER, R., A. P. GIRI, and R. A. ROY: 'Revised structure zone model for thin film physical structure'. *Journal of Vacuum Science & Technology A* (1984), vol. 2(2): pp. 500–503.

59. BOXMAN, RAYMOND L., DAVID M. SANDERS, and PHILIP J. MARTIN: *Handbook of Vacuum Arc Science & Technology: Fundamentals and Applications.* William Andrew, 1996.

60. PETROV, I., L. HULTMAN, U. HELMERSSON, J.-E. SUNDGREN, and J.E. GREENE: 'Microstructure modification of TiN by ion bombardment during reactive sputter deposition'. *Thin Solid Films* (1989), vol. 169(2): pp. 299–314.

61. ADIBI, F., I. PETROV, J. E. GREENE, L. HULTMAN, and J.-E. SUNDGREN: 'Effects of high-flux low-energy (20-100 eV) ion irradiation during deposition on the microstructure and preferred orientation of Ti0.5Al0.5N alloys grown by ultra-high-vacuum reactive magnetron sputtering'. *Journal of Applied Physics* (1993), vol. 73(12): pp. 8580–8589.

62. KELLY, P.J and R.D ARNELL: 'The influence of magnetron configuration on ion current density and deposition rate in a dual unbalanced magnetron sputtering system'. *Surface and Coatings Technology* (1998), vol. 108-109: pp. 317–322.

63. KELLY, P.J and R.D ARNELL: 'Magnetron sputtering: a review of recent developments and applications'. *Vacuum* (2000), vol. 56(3): pp. 159–172.

64. KELLY, P. J. and R. D. ARNELL: 'Development of a novel structure zone model relating to the closed-field unbalanced magnetron sputtering system'. *Journal of Vacuum Science & Technology A* (1998), vol. 16(5): pp. 2858–2869.

65. HARSHA, K. S. SREE: *Principles of Vapour Deposition of Thin Films.* Elsevier, 2006.

66. NEEL, LOUIS: 'Some theoretical aspects of rock-magnetism'. *Advances in Physics* (1955), vol. 4(14): pp. 191–243.

67. HOLBER, W. M., J. S. LOGAN, H. J. GRABARZ, J. T. C. YEH, J. B. O. CAUGHMAN, A. SUGERMAN, and F. E. TURENE: 'Copper deposition by electron cyclotron resonance plasma'. *J. Vac. Sci. Technol. A* (1993), vol. 11(6): pp. 2903–2910.

68. GRAPPERHAUS, MICHAEL J., ZORAN KRIVOKAPIC, and MARK J. KUSHNER: 'Design issues in ionized metal physical vapor deposition of copper'. *Journal of Applied Physics* (Jan. 1998), vol. 83(1): pp. 35–43.

69. DICKSON, M. and J. HOPWOOD: 'Axially-resolved study of highly ionized physical vapor deposition'. *Journal of Vacuum Science Technology A: Vacuum, Surfaces, and Films* (July 1997), vol. 15(4): pp. 2307–2312.

70. ROSSNAGEL, S.M.: 'Directional and preferential sputtering-based physical vapor deposition'. *Thin Solid Films* (1995), vol. 263(1): pp. 1–12.

71. ROSSNAGEL, STEVE: 'Ionization by radio frequency inductively coupled plasma'. *Thin Films.* Thin Films (2000), vol. 27. Ed. by HOPWOOD, JEFFREY A.: pp. 37–66.

72. *ATDF Technical Specifications of Q-Cleave-E reticle.*

73. GUO, WEI and CHARLES A DEJOSEPH JR: 'Time-resolved current and voltage measurements on a pulsed rf inductively coupled plasma'. *Plasma Sources Science and Technology* (2001), vol. 10(1): p. 43.

74. *Manual for the TRIAX 180/190/320/550 Monochromator.* 81021. Jobin Yvon. 2005.

75. PAYLING, R., DELWYN JONES, and ARNE BENGTSON: *Glow Discharge Optical Emission Spectrometry.* John Wiley & Sons Ltd., 1997.

76. PALMER, CHRISTOPHER: *Diffraction Grating Handbook.* NEWPORT CORPORATION, 2005.

77. *Hiden Analytical PSM 003 Manual.*

78. BENEDIKT, J, A HECIMOVIC, D ELLERWEG, and A von KEUDELL: 'Quadrupole mass spectrometry of reactive plasmas'. *Journal of Physics D: Applied Physics* (2012), vol. 45(40): p. 403001.

79. ALLEN JR, J.D., J.D. DURHAM, G. K. SCHWEITZER, and W.E. DEEDS: 'A new electron spectrometer design:II'. *Journal of Electron Spectroscopy and Related Phenomena* (1976), vol. 8(5): pp. 395–410.

80. PAUL, W. and H. STEINWEDEL: 'Ein neues Massenspektrometer ohne Magnetfeld'. *Zeitschrift fuer Naturforschung* (1953), vol. A8: pp. 448–450.

81. HOFFMANN, EDMOND de and VINCENT STROOBANT: *Mass Spectrometry Principles and Applications.* 3rd. John Wiley & Sons Ltd., 2007.

82. GUIMARAES, F and J BRETAGNE: 'Study of an argon magnetron discharge used for molybdenum sputtering. I. Collisional radiative model'. *Plasma Sources Science and Technology* (1993), vol. 2(3): p. 127.

83. GUIMARAES, F, J B ALMEIDA, and J BRETAGNE: 'Study of an argon magnetron discharge used for molybdenum sputtering. II. Spectroscopic analysis and comparison with the model'. *Plasma Sources Science and Technology* (1993), vol. 2(3): p. 138.

84. DONY, M.F., A. RICARD, J.P. DAUCHOT, M. HECQ, and M. WAUTELET: 'Optical diagnostics of d.c. and r.f. argon magnetron discharges'. *Surface and Coatings Technology* (1995), vol. 74 - 75, Part 1. Fourth International Conference on Plasma Surface Engineering: pp. 479–484.

85. ROSSNAGEL, S. M. and K. L. SAENGER: 'Optical emission in magnetrons: Nonlinear aspects'. *Journal of Vacuum Science & Technology A* (1989), vol. 7(3): pp. 968–971.

86. PINTASKE, R., TH. WELZEL, M. SCHALLER, N. KAHL, J. HAHN, and F. RICHTER: 'Spectroscopic studies of a magnetron sputtering discharge for boron nitride deposition'. *Surface and Coatings Technology* (1998), vol. 99(3): pp. 266–273.

87. KUNZE, HANS-JOACHIM: *Introduction to plasma spectroscopy.* Springer Berlin / London, 2009.

88. LENG, YANG: *Materials Characterization Introduction to Microscopic and Spectroscopic Methods.* Wiley-VCH Verlag GmbH & Co., 2013.

89. GOODHEW, P.J. and F.J. HUMPHREYS: *Electron Microscopy and Analysis.* 2nd Edition. Taylor & Francis London, 1988.

90. EGERTON, RAY: *Physical Principles of Electron Microscopy: An Introduction to TEM, SEM and AEM.* Springer Science & Business Media, 2006.

91. FOWLER, DAVID E.: *Encyclopedia of Materials Characterization Surfaces, Interfaces, Thin Films.* Ed. by BRUNDLE, C.RICHARD, CHARLES A. EVANS JR., and SHAM WILSON. Manning Publications Co, 1992.

92. KERR, JOHN: 'XLIII. On rotation of the plane of polarization by reflection from the pole of a magnet'. *Philosophical Magazine Series 5* (1877), vol. 3(19): pp. 321–343.

93. ALLWOOD, D A, GANG XIONG, M D COOKE, and R P COWBURN: 'Magneto-optical Kerr effect analysis of magnetic nanostructures'. *Journal of Physics D: Applied Physics* (2003), vol. 36(18): p. 2175.

94. LOCH, D A L and A P EHIASARIAN: 'A novel sputtering technique: Inductively Coupled Impulse Sputtering (ICIS)'. *IOP Conference Series: Materials Science and Engineering* (2012), vol. 39(1): p. 012006.

95. GODYAK, V, B ALEXANDROVICH, R PIEJAK, and A SMOLYAKOV: 'Nonlinear radio-frequency potential in an inductive plasma'. *Plasma Sources Science and Technology* (2000), vol. 9(4): p. 541.

96. *Table of Argon Sputter Yields at 45deg.* National Physical Laboratory. URL: `http://www.npl.co.uk/science-technology/%20%5C%5Csurface-and-nanoanalysis/services/sputter-yield-values`.

97. DICKSON, M., F. QIAN, and J. HOPWOOD: 'Quenching of electron temperature and electron density in ionized physical vapor deposition'. *J. Vac. Sci. Technol* (1997), vol. 15(2): pp. 340–344.

98. NICHOLS, C. A., S. M. ROSSNAGEL, and S. HAMAGUCHI: 'Ionized physical vapor deposition of Cu for high aspect ratio damascene trench fill applications'. *Journal of Vacuum Science & Technology B* (1996), vol. 14(5): pp. 3270–3275.

99. ROSSNAGEL, S. M.: 'Interaction between gas rarefaction and metal ionization in ionized physical vapor deposition'. *Journal of Vacuum Science & Technology B* (1998), vol. 16(6): pp. 3008–3012.

100. OCHSENBEIN, F., P. BAUER, and J. MARCOUT. *Astron. Astrophys., Suppl. Ser.* (2000), vol. 143: pp. 23–32.

101. LOCH, D. A. L., Y. A. GONZALVO, and A. P. EHIASARIAN: 'Nickel coatings by Inductively Coupled Impulse Sputtering (ICIS)'. *Surface and Coatings Technology* (2015), vol. 267. Selected Papers from The Society of Vacuum Coater's 57th Annual Technical Conference: pp. 98–104.

102. BRADLEY, J W, H BAECKER, Y ARANDA-GONZALVO, P J KELLY, and R D ARNELL: 'The distribution of ion energies at the substrate in an asymmetric bipolar pulsed DC magnetron discharge'. *Plasma Sources Science and Technology* (2002), vol. 11(2): p. 165.

103. LINNIK, A.I., A.M. PRUDNIKOV, R.V. SHALAEV, V.N. VARYUKHIN, S.A. KOSTYRYA, and V.V. BURKHOVETSKII: 'Synthesis and magnetic properties of nanocolumnar nickel films deposited in argon-nitrogen atmosphere'. English. *Technical Physics Letters* (2012), vol. 38(6): pp. 499–502.

104. TEBBLE, ROBERT S. and DEREK J. CRAIK: *Magnetic Materials.* Wiley-Interscience, 1969.

# APPENDIX A

## Papers Published in Refereed Journals

A.1 A novel sputtering technique: Inductively Coupled Impulse Sputtering (ICIS)

A novel sputtering technique: Inductively Coupled Impulse Sputtering (ICIS)



2012 IOP Conf. Ser.: Mater. Sci. Eng. 39 012006

(http://iopscience.iop.org/1757-899X/39/1/012006)

HIPIMS 2010 and 2011 IOP Publishing
IOP Conf. Series: Materials Science and Engineering **39** (2012) 012006 doi:10.1088/1757-899X/39/1/012006

# A novel sputtering technique: Inductively Coupled Impulse Sputtering (ICIS)

**D A L Loch, A P Ehiasarian**

HIPIMS Technology Centre, Sheffield Hallam University, Sheffield, UK

**Abstract.** Sputtering magnetic materials with magnetron based systems has the disadvantage of field quenching and variation of alloy composition with target erosion. The advantage of eliminating magnetic fields in the chamber is that this enables sputtered particles to move along the electric field more uniformly. Inductively coupled impulse sputtering (ICIS) is a form of high power impulse magnetron sputtering (HIPIMS) without a magnetic field where a high density plasma is produced by a high power radio frequency (RF) coil in order to sputter the target and ionise the metal vapour. In this emerging technology, the effects of power and pressure on the ionisation and deposition process are not known. The setup comprises of a 13.56 MHz pulsed RF coil pulsed with a duty cycle of 25 % . A pulsed DC voltage of 1900 V was applied to the cathode to attract Argon ions and initiate sputtering. Optical emission spectra (OES) for Cu and Ti neutrals and ions at constant pressure show a linear intensity increase for peak RF powers of 500 W - 3400 W and a steep drop of intensity for a power of 4500 W. Argon neutrals show a linear increase for powers of 500 W - 2300 W and a saturation of intensity between 2300 W - 4500 W. The influence of pressure on the process was studied at a constant peak RF power of 2300 W. With increasing pressure the ionisation degree increased. The microstructure of the coatings shows globular growth at $2.95\times10^{-2}$ mbar and large-grain columnar growth at $1.2\times10^{-1}$ mbar. Bottom coverage of unbiased vias with a width of 0.360 µm and aspect ratio of 2.5:1 increased from 15 % to 20 % for this pressure range. The current work has shown that the concept of combining a RF powered coil with a magnet-free high voltage pulsed DC powered cathode is feasible and produces very stable plasma. The experiments have shown a significant influence of power and pressure on the plasma and coating microstructure.

Keywords: ICIS, Ionised PVD, Magnet-free sputtering, deposition on high aspect ratio vias

## 1. Introduction

During sputtering charged particles i.e. ions, follow the electric field lines that are created in the chamber by the electric potential difference between the plasma bulk and the substrate surface. [1] This means that sputtering with a highly ionised metal plasma makes it possible to deposit coatings with good bottom coverage within high aspect ratio structures [2 - 4].

Conventionally, to achieve the high electron density necessary to ionise the working gas, a magnetic field needs to be applied on the target surface. To ionise the metal vapour additionally high power is necessary. Especially for sputtering magnetic materials the field is shunted and limits the usable target thickness. Furthermore, this additional magnetic field has the disadvantage of disturbing the uniform flow along the electric field lines. While this disturbance is advantageous for the initial

Corresponding author.
E-mail address: daniel.a.loch@student.shu.ac.uk (D Loch)

HIPIMS 2010 and 2011 IOP Publishing
IOP Conf. Series: Materials Science and Engineering **39** (2012) 012006 doi:10.1088/1757-899X/39/1/012006

ionisation of the gas and metal vapour as the collision probability is greatly enhanced, during the movement to the substrate the electrons are forced on cycloidical paths along the magnetic field lines and are confined near the target thus trapping gas and metal ions. [1]

Yukimura and Ehiasarian [5] have designed a magnet free experimental apparatus that consists of 2 electrodes immersed in an 200 kHz RF plasma that is produced by an inductor.

To extend the work described, we examine the ionisation degree in a plasma generated with a RF frequency of 13.56 MHz and a coil positioned within a vacuum chamber. In the current work an radio frequency (RF) powered Copper (Cu) coil is assembled in front of the target (Cu or Ti) to sputter and ionise the metal vapour. The current flowing through the coil induces a magnetic field that confines electrons to the inside of the coil thus enhancing the collision probability[6]. To attract the argon (Ar) ions to the target for sputtering, a high voltage pulsed DC is applied to the target. In the current work the effect of RF power on ionisation is studied and modelled by optical emission spectroscopy (OES) and the bottom coverage of Cu in vias is studied.

## 2. Experimental Details

The experimental ICIS system (schematic in Fig.1) consists of a UHV chamber (Kurt J. Lesker), a Hüttinger PFG 5000 RF power supply (13.56 MHz), a Advanced Converters HIPIMS power supply, a 2-turn 80 mm diameter solid rod copper coil and a magnet free 75 mm diameter cathode.

The plasma discharge is created within the RF powered coil. When the plasma has ignited, pulsed DC power is applied to the cathode. RF and DC power pulses are synchronised by a pulse generator.
In the current work a pressure - RF-power matrix was used to examine the influences of working pressure and RF- power on the discharge while the pulsed DC parameters were kept constant. During the experiments the working pressure was varied from $2.14 \times 10^{-1}$ - $2.96 \times 10^{-2}$ mbar and the RF power was varied between 500 W - 4500 W the DC voltage remained constant at 1900 V. The repetition frequency was 500 Hz with a pulse width of 500 µs, which relates to a duty cycle of 25%. The substrate was silicon oxide ($SiO_2$), an insulator, with vias, the bias voltage was floating. Temperature on the substrate at the beginning of the process was between 20 - 28 °C and during deposition the temperature rose by aprox. 5 °C within one hour.

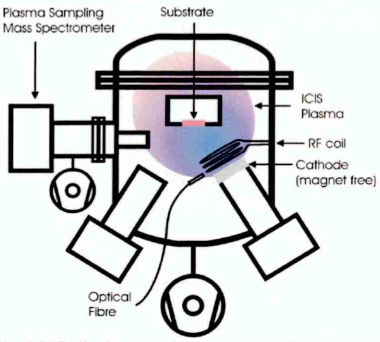


**Figure 1**. Experimental set up of the ICIS discharge with the assembly of the inductive coil, magnet free cathode and optical emission spectroscopy.

### *2.1. Plasma and coating characterisation techniques*

Analysis was carried out by Optical Emission Spectroscopy (OES) (Jobin Ivon Triax 320) with quartz optical fibre and collimator *in vacuo*. To compare the ionisation performance of ICIS with the well understood conventional rf coil enhanced magnetron sputtering technique, the results of the OES measurements were fitted into a model based on magnetron sputtering based on electron ionisation collisions.[7]

HIPIMS 2010 and 2011 IOP Publishing
IOP Conf. Series: Materials Science and Engineering **39** (2012) 012006 doi:10.1088/1757-899X/39/1/012006

Scanning Electron Microscopy (SEM) (FEI NovaSEM 200) was used to determine the bottom coverage, i.e. the ratio of the coating thickness on the bottom and top surfaces of vias.

*2.2. Modelling*

The used model correlates the optical emission of the plasma to the power on the cathode [7], in case of this work, it is the power applied to the induction coil. The model explains the connection between the intensity *(I(λij))* and power (P) for highly ionised magnetron plasma processes. It shows the increase in metal ionisation as a function of power. The intensity is expressed by a power law with exponent β. β is derived from the slope in a log — log graph.

The following subchapter will describe the basis of the model

The intensity of emission is expressed by the density of the components,

$$I(\lambda ij) = c(\lambda ij)\frac{Aij}{\sum_j Aij} \cdot n_0 \cdot n_e \cdot C^i \quad (1),$$

where *I(λij)* is the intensity, *c(λij)* is the spectral response of the spectrometer, *Aij* is the radiative frequency, $n_0$ is the gas neutral density, $n_e$ is the electron density and $C$ is the production rate by electron collision. The spectral response of the spectrometer *(c(λij))*, the radiative frequency *(Aij)* and the production rate by electron collisions can be assumed as constant *(Kij)* with respect to electron density.

For the excitation of Argon ($e + Ar \rightarrow Ar^*$) Eq.1 can be written as follows:

$I_{Ar} = K_{Ar} \cdot n_{Ar} \cdot n_e \cdot C^{Ar}$(2) As most parts of the equation are constant $I_{Ar} \propto n_e$. Further it is assumed that $C^i$ is constant with increasing power so that $n_e \propto P^\beta$, where P is the power and β is the slope in a log-graph. This concludes that $I_{Ar} = P^\beta$ (3).

We determine β by taking the logarithm of both sides of the equation are logarithmised to get and obtain: $\log(I_{Ar}) = \beta \log P$ (4).

Excitation of $Ti^0$ ($e + Me \rightarrow Me^* + e$) is: $I_{Me} = K_{Me} \cdot n_{Me} \cdot n_e \cdot C^{Me}$ (5).

Because plasma is considered quasineutral, $n_{Ar^+} \approx n_e$ and from the definition of sputtering yield it is known that $n_{Me} = \varepsilon \gamma_e n_{Ar^+}$ (6). Where ε is a constant and $\gamma_e$ is the sputtering coefficient, it can be concluded that $I_{Me} \propto {n_e}^2$ . From this it follows that $I_{Me} = \left(P^\beta\right)^2$ (7) and $\log(I_{Ion}) = 2\beta \log P$ (8).

For the ionisation of Ti ($e + Me \rightarrow Me^+ + 2e$), the intensity is $I_{Ion} = K_{Ion} \cdot n_{Ion} \cdot n_e \cdot C^{Ion}$(9). Where $n_{Ion} \approx n_{Me} \cdot n_e \approx {n_e}^2$. Thus $I_{Ion} \propto {n_e}^3$ and $I_{Ion} = \left(P^\beta\right)^3$ (10) which results in $\log(I_{Ion}) = 3\beta \log P$ (11).

## 3. Results and modelling

*3.1. Current and voltage*

The current and voltage behaviour on the cathode during a pulse can be seen in Fig. 2. The influence of the DC voltage on the current can be clearly seen, with the rise in current during the pulse. Hereby the target is biased to 1900V. Note that the voltage does not drop to zero as the current is too low to discharge the generator over the plasma.

HIPIMS 2010 and 2011 IOP Publishing
IOP Conf. Series: Materials Science and Engineering **39** (2012) 012006 doi:10.1088/1757-899X/39/1/012006

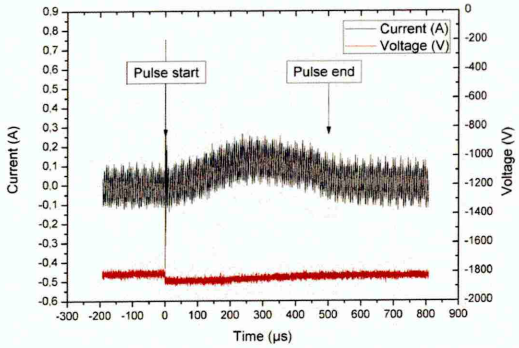


**Figure 2** Current and voltage over time on the Cu-cathode during a pulse at 1.2x10-1 mbar. The target is biased to 1900V. The current induced by the impinging ions is upto 0.3A.

*3.2. Optical Emission*

The OES measurements in fig. 3a and 3b show the intensities of the individual species in the ICIS plasma. In both Ti and Cu cases, strong emission from single-charged metal ions is present. Ar and Cu neutrals are detected as well. Due to limited availability of spectral lines for metal ions and neutrals in the optical spectrum, lines that are visible at all powers were chosen. Emission lines were transitions to ground state with similar upper excitation levels that were generally lower than the Ar neutral excitation level of 15 eV. Spectra lines data was taken from NIST.[8]

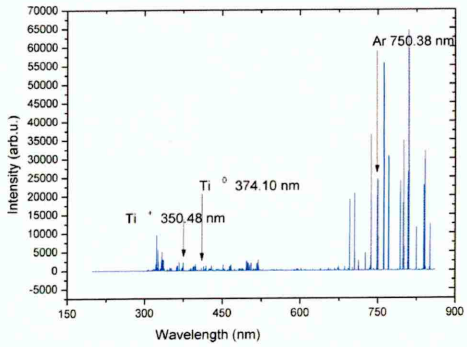


**Figure 3a** OES measurement of Ti ICIS plasmas at 1.2x10-1 mbar, 2300 W RF power. Lines used for analysis have been marked.

HIPIMS 2010 and 2011 IOP Publishing
IOP Conf. Series: Materials Science and Engineering **39** (2012) 012006 doi:10.1088/1757-899X/39/1/012006

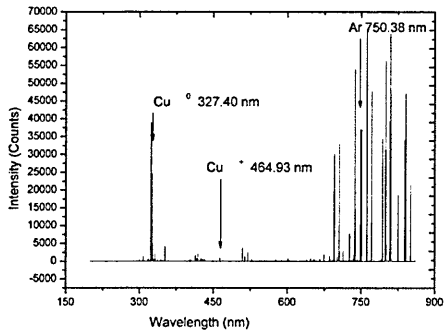


**Figure 3b** OES measurement of Cu and Ti ICIS plasmas at 1.2x10-1 mbar, 2300 W RF power. Lines used for analysis have been marked.

### *3.3. Modelling the influence of power on ionisation*

Calculations from the model predict a linear rise of intensity with increasing power in a log-log graph. In the case of ICIS of Ti plasma, measurements show that the slope of Ar is 0.61±0.08. As the model does not differentiate between sputter elements this means that according to the model the slope of the $Ti^0$ should be 1.22±0.08 and the slope of $Ti^+$ should be 1.83±0.08. As the slopes of the metal species are based on the Ar slope, they all share same error margin.

Figures 4a-c clearly show that all measured values fit very well into the error margin of the slope of the model. The Ti neutrals and ions rise with increasing power, with a sharp drop for very high RF power. Ar intensity rises continuously with power.

The rate of rise of metal ions is faster than that of metal neutrals. Thus the ionisation degree increases with increasing power.

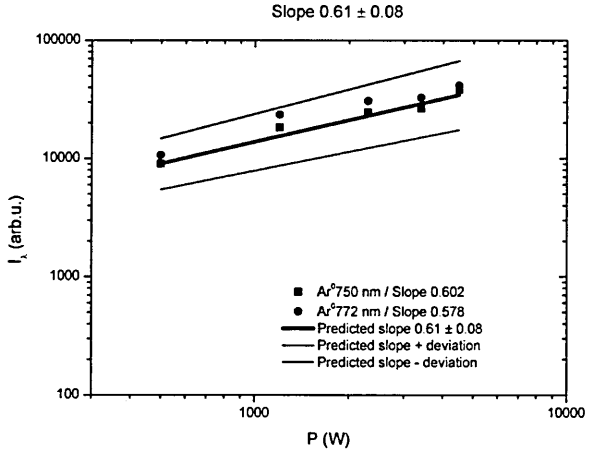


**Figure 4a** Measured and predicted results for the increase of ionisation with increasing power.

HIPIMS 2010 and 2011 IOP Publishing
IOP Conf. Series: Materials Science and Engineering **39** (2012) 012006 doi:10.1088/1757-899X/39/1/012006

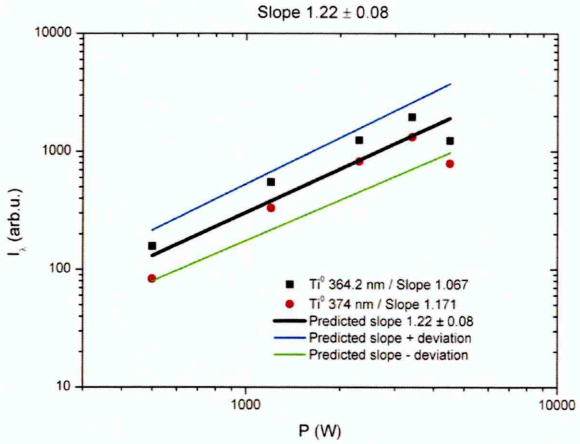


**Figure 4b** Measured and predicted results for the increase of ionisation with increasing power

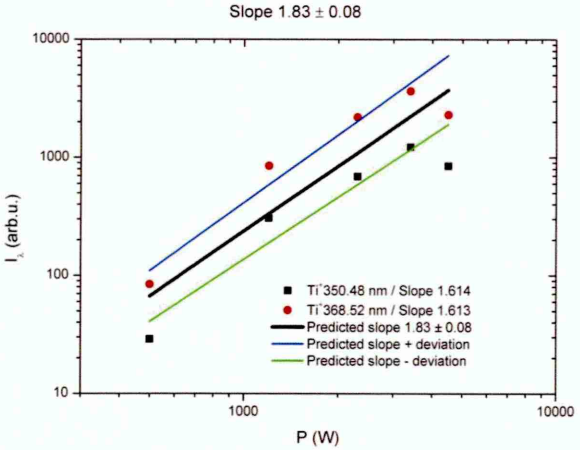


**Figure 4c** Measured and predicted results for the increase of ionisation with increasing power

Fig. 5 shows the increase in the ionisation degree as an ion to neutral ratio. For powers above 1000 W RF the rise is linear with increasing power. Below 1000 W the power is too low to generate Ti ions.

HIPIMS 2010 and 2011 IOP Publishing
IOP Conf. Series: Materials Science and Engineering **39** (2012) 012006 doi:10.1088/1757-899X/39/1/012006

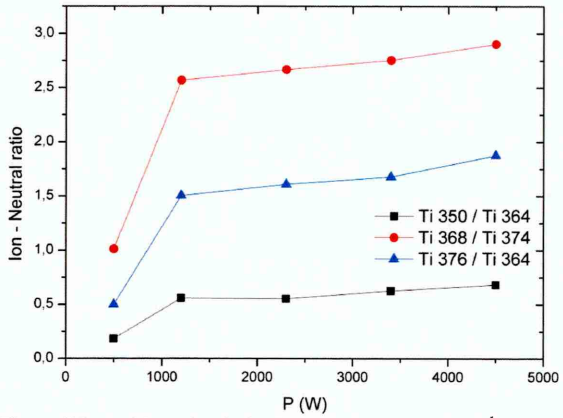


**Figure 5** Ion to Neutral ratio for Ti ICIS plasma at $1.2x10^{-1}$ mbar

Fig.6 shows similar measurements for an ICIS of Cu plasma. When comparing the optical emission from ICIS of Ti and Cu plasmas it can be seen that upto a power of 2300 W both show similar behaviour for the metal species with a linear increase of ionisation as a function of RF power. For higher powers there is a saturation for the Cu metal species.
When sputtering Ti the intensity of Ar rises continuously with increasing power, while when sputtering Cu the intensity of Ar saturates for higher powers.

Table 1 lists the slopes as predicted by the model for Ti and the slopes of the measured Cu plasma species. Cu deviates from the model as the metal slopes are not clearly related to those of the Ar. Additionally, the slope for Ar is significantly greater when Cu is used. The reasons behind this need to be examined further.

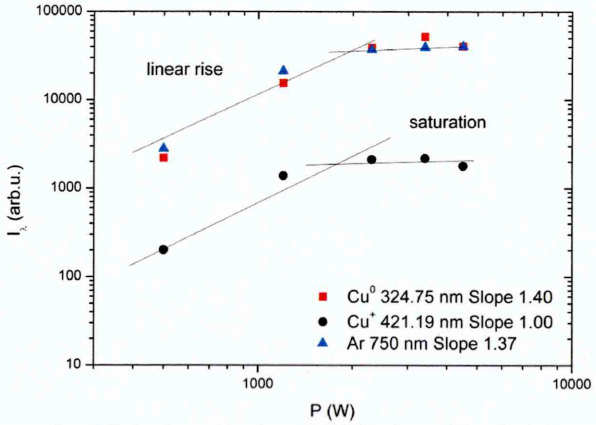


**Figure 6** Ar and Cu neutral and Cu ion intensities for an ICIS Cu plasma. The rise in intensity is linear with power. Pressue $1.2x10^{-1}$ mbar.

HIPIMS 2010 and 2011 IOP Publishing
IOP Conf. Series: Materials Science and Engineering **39** (2012) 012006 doi:10.1088/1757-899X/39/1/012006

**Table 1** Comparison of the slopes of Ar and Cu plasmas. The rise in intensity is linear with power for Ti. Also the Model will need to be adapted to take into account the lower ioniastion potential of metal ions compared to argon.

| | | | |
|---|---|---|---|
| $Ar^0$ slope: | 0.61 | $Ar^0$ slope: | 1.37 |
| $Ti^0$ slope: | 1.22 | $Cu^0$ slope: | 1.41 |
| $Ti^+$ slope: | 1.83 | $Cu^+$ slope: | 1.76 |

To get better results for high density plasmas, the model will need to be adapted to take into account the lower ionisation potential of metal ions compared to argon. This can be seen in the results for Cu, where the measured results do not fit into the model prediction. Cu has a higher sputter rate compared to Ti and as such, probably the metal ion density is considerably higher.
Also due to the possibillity of successive excitations the model results overestimate the presence of metal ions.

*3.4. SEM*

The cross sectional (Fig. 6) SEM image of a high aspect ratio via coated with ICIS of Cu shows good overall coverage. The deposition process was carried out at the higher end of power and, respectively, metal ionisation degree. For this high pressure ($1.2*10^{-1}$ mbar) process the bottom coverage is 21.6 %. The deposition rate was ca. 80 nm/h at 2300 W.

Table 2 compares the bottom coverage between high and low pressure depositions. A general trend was that bottom coverage improved at higher pressures.
The microstructure was influenced strongly by the pressure as well. Dense columnar structure was observed at the higher pressure ($1.2*10^{-1}$ mbar) and dense globular growth at the lower pressure of $2.9*10^{-2}$ mbar. The deposition rate is 99-119 $nmh^{-1}$ for RF-power of 2300 W, average target power of 67 W and a pressure of $1.2\times10^{-1}$ mbar.

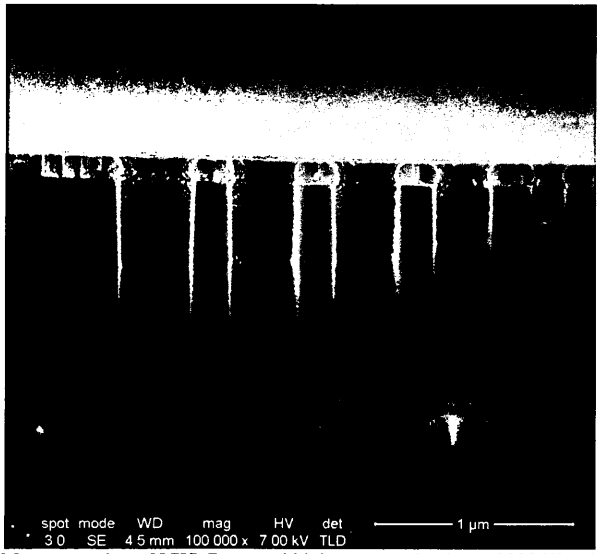


**Figure 7** SEM cross section of ICIS Cu coated high aspect ratio vias at 2300 W, 1.2*10-1 mbar.

HIPIMS 2010 and 2011 IOP Publishing
IOP Conf. Series: Materials Science and Engineering **39** (2012) 012006 doi:10.1088/1757-899X/39/1/012006

**Table 2** Bottom coverage of vias obtained at high and low pressure depositions.

| | Pressure: | $1.2 *10^{-1}$ mbar | |
|---|---|---|---|
| Height | Width | Top thickness | Bottom thickness |
| 1,40 µm | 315 nm | 120 nm | 18nm |
| Ratio: | 4:1 | Bottom coverage: | 21,6 % |
| | Pressure: | $2.96 *10^{-2}$ mbar | |
| 495 nm | 143 nm | 91.8 nm | 15.3 nm |
| Ratio: | 3.5:1 | Bottom coverage: | 14,0 % |
| 240 nm | 143 nm | 91.8nm | 15.3 nm |
| Ratio: | 1.7:1 | Bottom coverage: | 14,0 % |
| 163 nm | 143 nm | 91.8 nm | 20.4 nm |
| Ratio: | 1.2:1 | Bottom coverage: | 18.70% |

## 4. Conclusion

Successful experiments were carried out by sputtering Cu and Ti that present ICIS as a feasible sputtering technique. Working without magnetic field eliminates the racetrack that is created with magnetron sputtering, thus enhancing target utilisation and allowing ions to follow the electric field lines without disturbance.

The measured results of the rate of increase for gas neutrals, metal neutrals and metal ions fit very well to the predicted values of the model for magnetron sputtering. Calculations from the model confirm the increase of the ionisation degree as a function of power for Ti. Further examination has to be done into the sharp drop in intensity for metal neutrals and ions for high RF

Power and adjustments to the model have to be made to take this and the lower ionisation potential, as well as successive exitation into account.These results show that the ionisation mechanisms for ICIS are the same, by type as well as quantity, as for RF-enhanced magnetron sputtering, but without the influence of the magnetic field of the magnetron.

Copper deposition on high aspect ratio vias has shown very promising results. The bottom coverage in vias with aspect ratio of 4:1 is 21.6 % with dense columnar growth and without bias.

## References

[1] Chapman B 1980 Glow Discharge Processes: Sputtering and Plasma Etching. *Wiley-Interscience; 1 edition.*
[2] Grapperhaus M, Krivokapic Z, Kushner M J 1997 J. Appl. Phys. **83**(1), 35 - 43
[3] Hopwood J, Qian F 1995 *J. Appl. Phys.* **78** (2), 758 – 765.
[4] Rossnagel S M, Hopwood J 1993 *J. Vac. Sci. Technol.* **B 12(1)**, 449 – 453.
[5] Yukimura K, Ehiasarian A P 2009 *Nuclear instruments and methods in physics research section B: Beam interactions with materials and atoms,* **267** (8-9), 1701-1704.
[6] Hopwood J 1992 *Plasma Sources Sci. Technol.* **1**, 109 - 116.
[7] Dony M F, Ricard A, Dauchot J P, Hecq M, Wautelet M 1995 *Surf. Coat. Technol.*, **74-75**, 479-484.
[8] NIST atomic spectra database: http://www.nist.gov/pml/data/asd.cfm

## A.2 Nickel Coatings by Inductively Coupled Impulse Sputtering (ICIS)

Surface & Coatings Technology 267 (2015) 98–104

Contents lists available at ScienceDirect

Surface & Coatings Technology

journal homepage: www.elsevier.com/locate/surfcoat

# Nickel coatings by Inductively Coupled Impulse Sputtering (ICIS)

Daniel A.L. Loch [a,*], Yolanda A. Gonzalvo [b], Arutiun P. Ehiasarian [a]

[a] HIPIMS Technology Centre, Materials and Engineering Research Institute, Sheffield Hallam University, Howard St., Sheffield S1 1WB, UK
[b] HIDEN Analytical Ltd., Europa Boulevard, Warrington WA5 7UN, UK

ARTICLE INFO

Available online 18 November 2014

*Keywords:*
ICIS
Pulsed plasma source
Ionised PVD
Magnet-free sputtering
Deposition on high aspect ratio vias
Magnetic material

ABSTRACT

Inductively Coupled Impulse Sputtering (ICIS) removes the need for a magnetron, whilst delivering equal or higher ion-to-neutral ratios compared to other ionised PVD technologies such as High Power Impulse Magnetron Sputtering (HIPIMS). This is especially advantageous for the sputtering of magnetic materials, as these would shunt the magnetic field of the magnetron, thus reducing the efficiency of the sputtering and ionisation process. ICIS produces highly ionised metal-dominated plasma inside a high power pulsed RF-coil with a magnet free high voltage pulsed DC powered cathode.

ICIS operation with magnetic target materials has not been attempted so far. The paper aims to clarify the effects of power and pressure on the chemistry of the deposition flux and is the first investigation of the microstructure of ICIS deposited coatings.

Modelling based on the intensity of the optical emission spectra (OES) is conducted for the first time on the excited species of Ni and Ar in relation to the applied RF-power. Sputtered species show a linear intensity increase for increasing peak RF-power and constant process gas pressure.

The influence of increasing process gas pressure on the ionisation was studied at a constant peak RF-power for pressures. For pressures below 8 Pa the intensity rises, but then remains constant for pressures up to 26 Pa.

The microstructure of Ni coatings shows columnar dendritic or globular growth depending on the ionisation degree. In relation to the film thickness on the top of the substrate, the bottom coverage of unbiased vias with an aspect ratio of 4:1 was 15% and for lower aspect ratios of 1.5:1 was 47.5%.

The current work has shown that the concept of combining a pulsed RF driven coil with a magnet-free pulsed DC powered cathode works well for the sputtering of magnetic material in a stable plasma.



## 1. Introduction

Deposition of thin films of magnetic material is of great importance for various applications such as data recording [1] and magnetic microelectromechanical systems and sensors (MagMEMS) [2,3].

A high degree of ionisation of sputtered species is preferable, as this allows deposition on structured surfaces because ions follow the electric field lines that are created by the potential difference between the plasma bulk and substrate surface and are oriented normally to surface features [4]. This makes it possible to deposit even coatings on sidewalls and the bottom of high aspect ratio features of the substrate [4]. Further this can reduce lattice defect density in the coating and prohibit the early covering of via and trench openings on the substrate, especially on high aspect ratio structures [5,6].

Magnetron-based sputtering techniques suffer from low target utilisation rates of approx. 40% [7] and low utilisation intervals for magnetic materials as targets need to be thin to allow for sufficient magnetic field strength to be established above the target surface by the magnets of the magnetron [8]. Inductively Coupled Impulse Sputtering (ICIS) is a new development which aims to solve the previously mentioned issues by eliminating the need for a magnetron. ICIS is based on an experimental development by Yukimura and Ehiasarian [9], which utilises high pulsed RF-power in the coil and high pulsed DC voltage on the target to generate dense plasma and attract argon ions ($Ar^{1+}$) to initiate sputtering. In previous work the RF-plasma assisted high power pulsed glow discharge was adapted to work inside a deposition system and uses a 13.56 MHz RF-power supply to create the basis for a practical application of ICIS technology [10].

In the current work the plasma composition and ionisation mechanisms are studied in detail for the first time. Optical Emission Spectroscopy (OES) was used to analyse $Ar^0$, $Ni^0$ and $Ni^{1+}$ ion emission. Further measurements by energy-resolved mass spectroscopy were conducted for $Ar^{1+}$ and $Ni^{1+}$ ion fluxes.

A model based on the optical emission of argon in DC and RF magnetron discharges is used to explain the connection between the intensity ($I(\lambda_{ij})$) and power ($P$) for magnetron plasma processes. Dony et al. [11] explain the dependence of the optical emission of the plasma to the power on the cathode. As with ICIS the plasma is generated by an induction coil and not on the target surface, in this study we correlate the

* Corresponding author.
*E-mail address:* d.loch@shu.ac.uk (D.A.L. Loch).

http://dx.doi.org/10.1016/j.surfcoat.2014.11.029
0257-8972/

optical emission of the plasma to the power applied to the coil. As the model is based on processes occurring in magnetron plasmas, we compare the ionisation efficiency of ICIS with conventional magnetron processes.

We report for the first time the microstructure of films formed under ICIS conditions and look at the correlations between morphology and plasma chemistry.

The coating microstructure and thickness are analysed by Scanning Electron Microscopy (SEM) and the coating chemical composition and contamination by sputtered RF-coil material by Energy-Dispersive X-ray spectroscopy (EDX).

## 2. Experimental details

The experimental ICIS system (shown schematically in Fig. 1 and dimensions in Table 1) is set up inside a UHV chamber (Kurt J. Lesker CMS-18) and consists of a 2-turn 80 mm diameter solid rod copper coil and a magnet-free 75 mm diameter cathode furnished with a high purity (3N) Ni target, a Hüttinger PFG 5000 RF power supply (13.56 MHz) to power an RF-coil and a Hüttinger HIPIMS power supply HMP 6/16 to apply a pulsed DC voltage to the cathode. Argon with a purity of 99.998% was used as process gas.

Due to the highly ionised metal plasma that is produced by ICIS, we do not expect to see an influence on the morphology of the coating by the tilt angle between the target and substrate normals. Ionised species would follow the electrical field lines perpendicular to the substrate surface. Additionally, the operating pressures are sufficiently high that we could expect a high number of collisions of metal with the working gas resulting in a randomised (as opposed to directional) flux of depositing particles to the surface of the substrate. However, due to the remaining neutral species in the flux some influence on the top corner of the via can be expected.

The plasma discharge is created within the area of the induction coil driven with pulsed RF power. When the RF plasma has ignited, pulsed DC power is applied to the cathode to attract positive Ar ions to the target surface to initiate sputtering. RF and DC power pulses are synchronised by a pulse generator.

In the current study a pressure vs. RF-power matrix was used to examine the influence on the ionisation in the discharge and deposition flux properties. The pulsed DC voltage was kept constant at 1900 V.

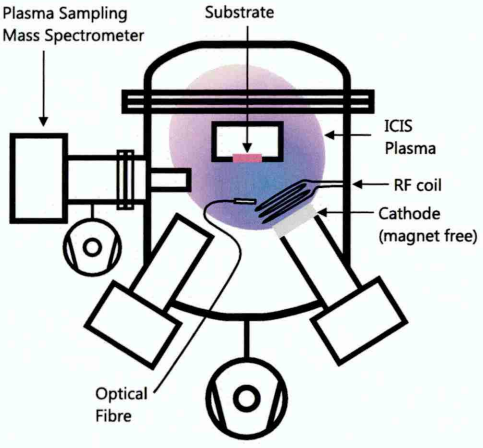


**Fig. 1.** Experimental setup of the ICIS deposition system with the assembly of the inductive coil, magnet-free cathode and OES location. The angle between target and substrate normals is 32°.

**Table 1**
Dimensions of the ICIS setup.

| | |
|---|---|
| Diameter of copper coil: | 7 mm |
| Length of copper coil: | 500 mm |
| RF coil (centre) to substrate distance: | 127 mm |
| Target to substrate distance: | 130 mm |

The working pressure was varied from 2.96 to 21.4 Pa by increasing Ar flow. Peak RF-power was varied between 1000 and 4800 W applied at a repetition frequency of 500 Hz with a pulse width of 150 μs. These settings result in a duty cycle of 7.5%, reducing the average power and thermal load on the coil. The base pressure was in the region of $5 \times 10^{-5}$ Pa. Thin film deposition was carried out on silicon dioxide ($SiO_2$) substrates with vias that were held at floating bias potential. In this series of experiments, the aspect ratio (AR) is the relation of depth to width of the via. Temperature on the substrate at the beginning of the process was between 20–28 °C and no further substrate heating was applied. During deposition the temperature rose by 6–8 °C/h. The deposition rate was approx. 125 nm/h (0.35 Å/s) at a RF power setting of 4000 W and a pressure of 6.4 Pa and approx. 50 nm/h (0.14 Å/s) for a pressure of 14 Pa.

### 2.1. Plasma and coating characterisation techniques

Plasma composition analysis was carried out by OES monochromator (Jobin Yvon Triax 320, HORIBA Synapse CCD detector) with in vacuo quartz optical fibre and collimator placed as indicated in Fig. 1. The spectra resolution is 0.12 nm (1200 grooves/mm in the grating), the focal length of the monochromator was 320 mm and the entrance slit size 0.06 mm.

The fibre is connected to a collimator lens which is protected by a sapphire window inside a 90 mm long, 8 mm internal diameter lens cover that protects the optical fibre from being coated. The spatial resolution is 10 mm, acceptance angle is nominally 2.5°.

The comparison of the excitation efficiency of ICIS with conventional ICP magnetron sputtering is done by using the OES measurement results for increasing RF-power in the model for ionisation by electron and Penning collisions developed for RF-coil enhanced magnetron sputtering described in Section 2.2.

An energy resolved mass spectrometer (Hiden Analytical PSM 003) was used to measure the ion content and ion energy for $Ar^{1+}$ and $Ni^{1+}$ in the ICIS plasma at a position near the substrate as shown in Fig. 1. The energy spectra resolution of the instrument is below 0.5 eV.

SEM (FEI NovaSEM 200) was used to examine the coating properties and to determine the structure and bottom coverage (BC). The bottom-coverage, is a value for the percentage of cover on the bottom of a via compared to the film thickness on the surface of the substrate. An EDX system (Oxford Instruments X-Max detector and INCA analysis software) and 20 keV electron beam were used to obtain the relative composition of the films.

Magnetic properties of the films were measured by Magneto Optical Kerr Effect Spectroscopy (MOKE) at the University of Lisbon. MOKE hysteresis loops were obtained from measurements of the polarization angle of a He–Ne laser (wavelength 633 nm, power 0.5 mW and 1 mm beam diameter) in longitudinal geometry where the magnetic field to the sample was applied in the film plane.

### 2.2. Modelling of the excitation properties

As with ICIS a magnetron is not used to trap the electrons close to the target surface, it is of interest to see how the ICIS process compares to magnetron based sputter processes in terms of excitation and ionisation efficiency of the process gas and sputtered material. Dony et al. [11] have looked at the ionisation in RF driven magnetron processes and optical emissions thereof. In the following we will explain how the Dony model is used to explain the ionisation behaviour of ICIS plasma.

Emission intensity measurement results in Section 3.2 showed an increase in gas and metal excitation and ionisation as a function of power. Generally, the relation between emission intensity of the element ($I_{El}$) and RF-power ($P$) in the coil is expressed by a power law with an exponent that is specific to each species.

For the intensity of argon neutrals and metastables we experimentally obtain the following relation: $\log(I_{Ar}) = \beta \log P$ (1), where $I_{Ar}$ is the intensity of Ar for a chosen wavelength, $P$ is the power applied to the RF coil and $\beta$ is the slope obtained for $Ar^0$.

As the excitation of Ar is predominantly by electron collision the emission intensity $I_{Ar} = K_{Ar} \cdot n_{Ar} \cdot n_e \cdot C^{Ar}$ (2) can be assumed as proportional to the electron density $n_e$, from this follows: $I_{Ar} \propto n_e$ (3).

From Eqs. (1) and (3) it can be concluded that $n_e \propto P^{\beta}$ (4).

For the excitation of metal neutrals the intensity is $I_{Me} = K_{Me} \cdot n_{Me} \cdot n_e \cdot C^{Me}$ (5). Where $K_{Me}$ is a function of the spectral response of the spectrometer and the radiative frequency and can be considered constant for a given line, $n_{Me}$ is the metal atom density and $n_e$ is the electron density. $C^{Me}$ is the production rate by electron collisions and depends on electron temperature, which we assume to be constant for constant pressure and increasing applied power. To assess the temperature shifts as a function of power we analysed the emission line ratio of Ni neutral excitation at different energy levels 310.54 nm (34,408 $cm^{-1}$) and 373.68 nm (57,789 $cm^{-1}$) as compared to 373.92 nm (28,086 $cm^{-1}$). These ratios are sensitive to changes in electron temperature similar to the differences in energy levels. The results (not shown) indicated changes in ratio for the lower temperatures which increased for powers up to 3000 W and were constant thereafter. The ratio was constant for the higher temperatures. This indicates that the fluctuations in temperature were small and can be neglected. This could be attributed to the high operating pressures of the process which induce a high frequency of collisions during which electrons are thermalised efficiently.

The definition of the sputtering yield is $n_{Me} = \varepsilon \gamma_e (n_{Ar^+} + n_{Me^+})$ (6), where $\varepsilon$ is a constant and $\gamma_e$ is the weighted sputtering coefficient for gas and metal sputtering. As plasma can be considered to be quasineutral, the Ar and metal ion density is equivalent to the electron density $(n_{Ar^+} + n_{Me^+}) \approx n_e$ (7). By substituting $(n_{Ar^+} + n_{Me^+})$ with $n_e$ in Eq. (6) and inserting in Eq. (5) it can be concluded that $I_{Me} \propto n_e^2$ (8). Following from Eqs. (4) and (8) for metal neutrals we can conclude that $I_{Me} \sim (P^{\beta})^2$ (9). From this follows that for Ni neutrals in a logarithmic scale the slope $\beta$ is twice as steep as for Ar neutrals: $\log(I_{Ni^0}) \sim 2\beta \log P$ (10). Assuming electron collisions to be the main ionisation mechanism we can assume the metal ion density $(n_{Me^{1+}})$ to be $n_{Me^{1+}} \sim n_{Me} \cdot n_e$ (11). Further from Eqs. (4), (6) and (7) we know that $n_{Me} \sim n_e^2$ (12).

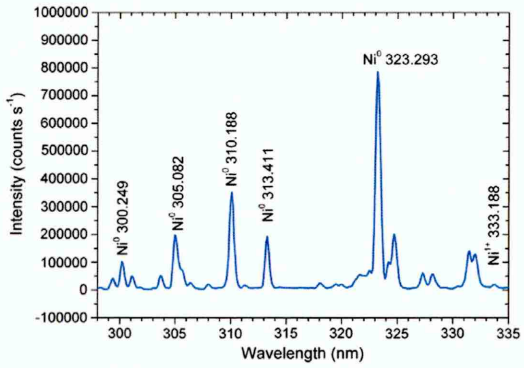


**Fig. 2.** OES graph of the emission intensity of Nickel in ICIS plasma. Clearly visible are the high intensity Ni neutral lines. Ni ion line is the strongest line in the visible spectrum. Applied RF power was 3000 W.

Combining Eqs. (4), (11) and (12), we obtain: $\log(I_{Ni^{1+}}) \sim 3\beta \log P$ (13) for Ni ions. The coefficient of proportionality is higher because a further electron collision is necessary to ionise the metal atoms. This means that the slope of Ni ions is expected to be three times steeper than that of excited Ar neutrals. This is consistent with the findings for conventional DC magnetron sputtering by Rossnagel and Saenger [12].

Furthermore, Penning ionisation of the metal vapour by collisions with Ar metastables ($Ar^*$) needs to be taken into account due to the high operating pressures of the discharge which increase the collision cross section for these types of collisions to be similar to that of electron collision processes. In analogy to the electron collision process, in Penning ionisation the densities of sputtered metal are proportional to the density of electrons; $n_{Me} \approx n_e$ (14), see Eqs. (6) and (7). The ionisation of neutral species is facilitated by collisions with metastable $Ar^*$, this means that $n_{Me^{1+}} \propto n_{Me} \cdot n_{Ar^*}$ (15). This is in turn proportional to $n_{Me} \cdot n_{Ar^*} \propto n_{Me} \cdot n_e$ (16). Using Eq. (14) we can substitute $n_{Me}$ with $n_e$ and obtain $n_{Me^{1+}} \propto n_e^2$ (17). The emission intensity can be seen to be related to the density of ions and electrons, as a further collision is necessary to excite the ion; $I_{Ion} \propto n_{Ion} \cdot n_e$ (18). With Eq. (17) it can be seen that the metal ion intensity is $I_{Me^{1+}} \propto n_e^3$ (19). This analysis indicates that both electron collision and Penning ionisation lead to a similar trend for intensity vs. plasma density and applied RF power.

## 3. Results & discussion

### 3.1. Plasma emission results

Optical spectra for an ICIS 3000 W Ni plasma in Fig. 2 show strong emission from Ni neutrals. Ni ions were found on the only strong emission line in the visible spectrum at a wavelength of 333.188 nm. This line is a convolution of the 333.103 nm and 333.287 nm lines which have similar weighted oscillator strengths of 0.163 and 0.138 respectively, calculated with values from Ochsenbein et al. [13]. Most Ni ions can be expected to emit at lower wavelengths very much further in the ultraviolet spectrum. Additional experiments were conducted by mass- and energy-resolved spectroscopy to detect these, as discussed separately in Section 3.3.

### 3.2. Influence of applied RF-power on ionisation and modelling

Fig. 3 shows measured OES intensities against RF-coil power in a log–log graph for the ICIS of Ni plasma. From the slope of excited Ar we obtain an exponent $\beta = 0.34$, which is approx. half the value for

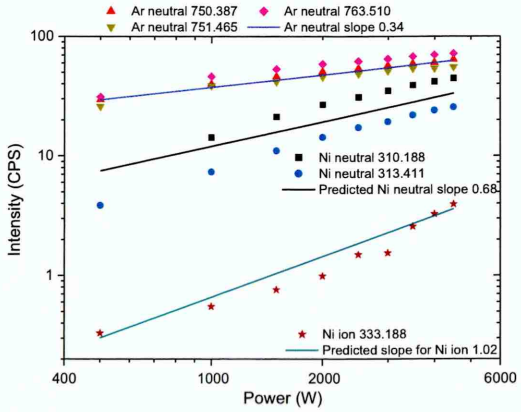


**Fig. 3.** Measured results for Ar and Ni neutrals for a constant pressure of 12 Pa with varying RF-power.

**Table 2**
List of observed gas and metal species data and observed and predicted slope values of intensity–power modelling.

| Species | Wavelength (nm) | Osc. strength | Slope | |
|---|---|---|---|---|
| | | | Observed | Predicted |
| $Ar^0$ | 750.387 | 0.339 | 0.34 | – |
| $Ar^0$ | 751.465 | 0.316 | 0.33 | 0.34 |
| $Ar^0$ | 763.511 | 1.047 | 0.36 | 0.34 |
| $Ni^0$ | 310.188 | 0.568 | 0.78 | 0.68 |
| $Ni^0$ | 313.411 | 0.533 | 0.87 | 0.68 |
| $Ni^{1+}$ | 333.188 | 0.163–0.138 | 1.12 | 1.02 |

the Ar emission from the 4p level for RF-MS [11] and one third of value reported for DC–MS [12]. The slopes for excited Ar and Ni neutrals (Table 2 contains the observed gas and metal species) fit very well to the model with the $Ni^0$ intensity rising with a factor of 2 faster compared with $Ar^0$. The only deviation from the model is the saturation of $Ni^0$ intensity for RF-power settings above 3000 W. For Ni ions the slope of the log intensity is three times the slope of $Ar^0$ for RF-power settings below 3000 W. This is consistent with excitation by electron collisions and ionisation by either electron or $Ar^*$ metastable collisions as described by the used model. Several factors could be the cause for the deviation from the model, such as increased ionisation efficiency for powers above 3000 W by Penning ionisation, a reduction of the mean free path and higher electron temperatures.

The ion to neutral ratio in Fig. 4 for increasing RF power at a constant pressure shows a doubling of the ratio from 2000 W to 4000 W. This means that the influence of ions on the coating will change largely in this regime. Especially for deposition into high AR vias the higher ion to neutral ratio is known to enable a better coverage and film growth on sidewalls and bottom. For AR larger than 3:1 the deposition on the bottom of the via is mainly by ions, as has been shown by Rossnagel [4]. The higher ratio of ions to neutrals also allows for denser coatings with metal ions being more efficient than gas [14].

### 3.3. Influence of process pressure on ionisation

Fig. 5 describes the influence of pressure on the ionisation at a constant power of 3000 W. For pressures below 10 Pa there is a linear intensity increase for all gas and metal species. For pressures of 10–20 Pa, the Ar neutral intensity remains constant, whilst the Ni neutral intensity decreases between 10 Pa and 15 Pa; remaining constant for pressures up to 26 Pa. Ni ion intensity remains constant for all pressures above

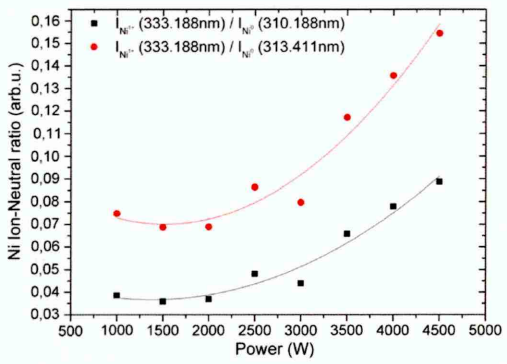


**Fig. 4.** Ion to neutral ratio of ICIS Ni plasma for increasing RF power at constant process pressure. Emission lines used were: $Ni^{1+}$ at 333.188 nm, $Ni^0$ at 310.188 nm and $Ni^0$ at 313.411 nm.

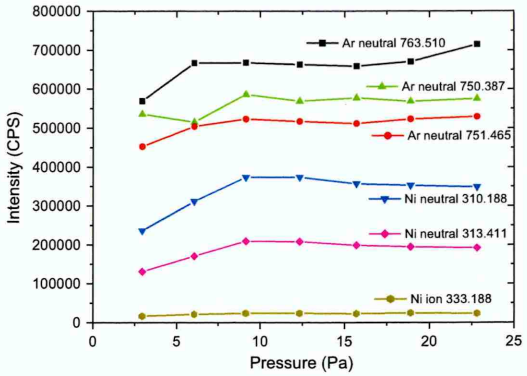


**Fig. 5.** Measured results for Ar and Ni neutrals for a constant RF-Power of 3000 W and varying pressure.

10 Pa. This is also confirmed by the ion to neutral ratio plot in Fig. 6 where there is no change in the ratio.

This could be due to the constant RF power that is not sufficient to allow further excitation or ionisation of metal species at pressures higher than 10 Pa.

### 3.4. Mass and energy resolved spectroscopy

The energy of impinging ions on the surface of the substrate is an important factor in densifying the structure of the film [14]. For magnetic materials, where the domain size is approx. 50 nm, to achieve bulk material properties in a thin coating it could be beneficial to promote densification of the coating. Fig. 7 shows the measurement for $Ni^{1+}$ and $Ar^{1+}$ ions at 3000 W and 13 Pa. The energy distribution follows a non-Maxwellian distribution with a narrow ion energy bandwidth. The highest intensity peak energy is 20 eV which corresponds to the plasma potential. This energy has been found to be an ideal level for ion surface mobility without inducing lattice defects. This low energy level and high ion to neutral ratio make it suitable for production of dense coatings [14]. A further lower intensity peak is visible at 170 eV corresponding to high energetic ions which can

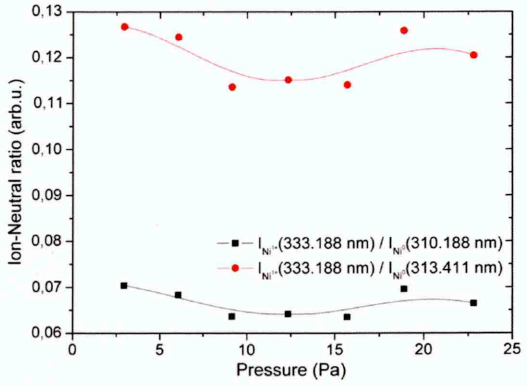


**Fig. 6.** Ion to neutral emission ratio of ICIS Ni plasma for constant power and increasing pressure. Emission lines used were: $Ni^{1+}$ at 333.188 nm, $Ni^0$ at 310.188 nm and $Ni^0$ at 313.411 nm.

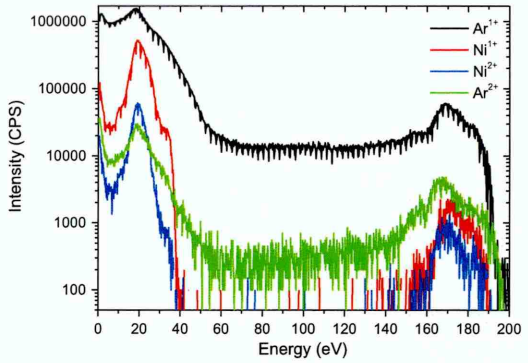


**Fig. 7.** Ni ion energy distribution for a ICIS plasma. 20 eV is an ideal energy level for increased surface mobility and reduced lattice defects. A second, lower intensity peak is at 170 eV. The double charge of the ion has not been considered in the energy axis.

be found also in pulsed plasmas [15]. To determine the origin of these energetic ions further work is necessary which lies outside the scope of this paper.

### 3.5. Coating properties

For the examination of the coating properties we deposited Ni for a range of power and pressure values from the matrix used for the plasma study in Sections 3.1 and 3.2. From the plasma study it was concluded that a pressure of approx. 14 Pa would be sufficiently high to study the influence of power on the coating, as the influence of pressure on the plasma does not change significantly above 10 Pa. Power settings of 2000 W, 3000 W and 4000 W applied peak RF-power were chosen to evaluate the influence of power.

Fig. 8a shows the cross section of the coating deposited at 2000 W RF-power in a via with AR 3:1. A dense globular microstructure can be observed near the surface. A good bottom and sidewall coverage are visible.

The accumulation of material at the bottom of the structure indicates deposition by ions [16]. The overall distribution of the deposit indicates that the majority of the deposited species were metal ions. The dense structure of the bottom coating and no visible separation between the sidewall and bottom as well as the even sidewall coverage suggest only modest resputtering from the bottom of the via.

Figs. 8b (3000 W RF-power) and c (4000 W RF-power) exhibit the same features of the coating on the substrate surface as well as the sidewalls and bottom of the via. However, as can be seen from the insets, the microstructure changes with increasing applied RF-power. The grain

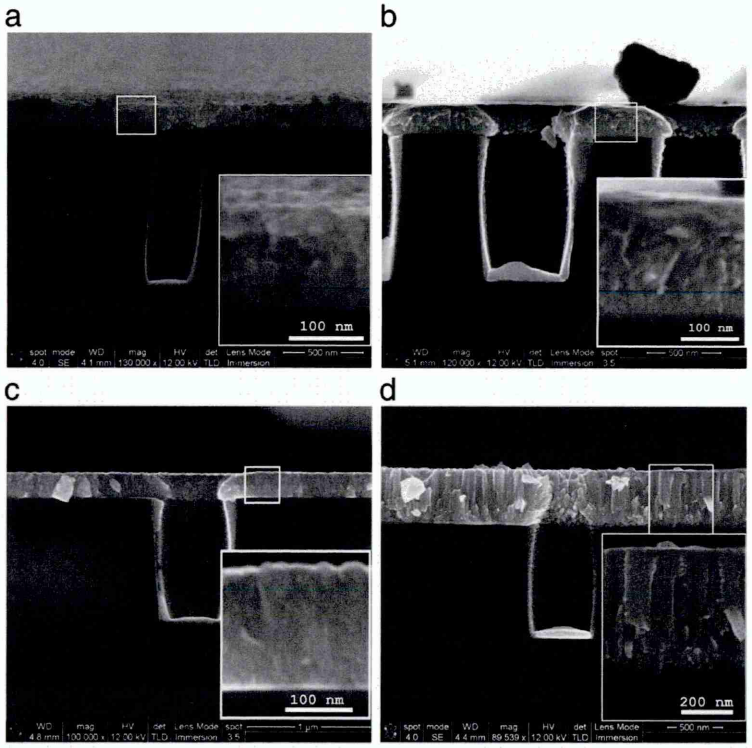


**Fig. 8.** a. SEM cross section of Ni coated via with an AR of 3:1. Deposition parameters 2000 W applied RF-power in ICIS plasma, process pressure 14 Pa. The inset shows magnified image of the coating exhibiting dense globular structure. Deposition rate is 40 nm/h. b. SEM cross section of Ni coated via with an AR of 2:1. Deposition parameters 3000 W applied RF-power in ICIS plasma, process pressure 14 Pa. The inset shows the magnified image of the coating showing dense globular structure, but with a smaller feature size than with 2000 W applied RF-power. Deposition rate is 50 nm/h. c. SEM cross section of Ni coated via with an AR of 2:1. Deposition parameters 4000 W, applied RF-power in ICIS plasma, process pressure 14 Pa. The inset shows the magnified image of the coating showing dense globular structure, but with a smaller feature size than with 3000 W applied RF-power. Deposition rate is 45 nm/h. d. SEM cross section of Ni coated high aspect ratio vias deposited with 4000 W RF-Power at 6.4 Pa. The dense columnar structure with dendritic features can be seen. The inset shows the magnified coating structure.

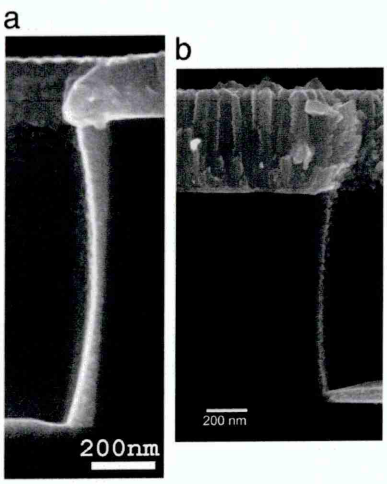


**Fig. 9.** a. Close-up of the corner of the via from Fig. 8b (deposition at 14 Pa) showing dense globular growth of the Ni coating. Sidewalls and bottom of the via are evenly coated indicating high metal ionisation and modest resputtering from bottom. b. Close-up of the corner of the via from Fig. 8d (6.4 Pa). Dendritic growth of the Ni coating can be seen along with the perpendicular growth on the sidewalls.

size reduces and grain boundaries are obscured resulting in a denser coating microstructure. This is consistent with an increased ionisation rate of the deposition flux (Fig. 4) which provides adatoms with high energy and long diffusion paths on the surface of the growing film.

The influence of pressure on the coating morphology at a constant power setting of 4000 W RF power can be seen when comparing Fig. 8c and d. Fig. 8d shows a cross sectional SEM image of a via with an AR of 2:1 at low pressure (6.4 Pa). These conditions result in a medium ionisation degree of the sputtered material. The films exhibit dense columnar dendritic growth. Similar results for the microstructure have been shown by Linnik et al. [17], albeit these coatings were deposited in a $N_2$ atmosphere and as such have reduced magnetic properties, compared to pure Ni coatings. For the abovementioned process settings and AR the BC is 21.2%.

The coating deposited at the higher pressure of 14 Pa exhibits a denser globular structure (Fig. 8c). The factor 2 increase in pressure resulted in a factor of 2.5 reduced deposition rate due to increased elastic scattering of the depositing species by the process gas and reduced diffusion rate. Generally increasing the pressure causes collisional thermalisation of the depositing species, reduction of their energy and mobility on the surface of the growing film resulting typically in a reduced coating density.

Close-up images of the whole length of the via of the samples coated at 4000 W applied RF-power with pressure settings of 14.3 Pa (Fig. 9a) and 6.4 Pa (Fig. 9b), clearly show that the growth of columns on the sidewalls is mostly perpendicular to the substrate surface and homogeneously level over the whole length of the sidewall of the feature.

**Table 3**
Coating composition of a process series showing reduced contamination by RF coil material or other impurities.

| Sequence | 1 (0 h) | 2 (4 h) | 3 (8 h) |
|---|---|---|---|
| Power/pressure | 4000 W/14.1 Pa | 4000 W/24.7 Pa | 3000 W/14.3 Pa |
| Element | Weight % | Weight % | Weight % |
| Ni | 90.30 | 94.58 | 100.00 |
| In | 6.34 | 5.42 | – |
| Cu | 3.37 | – | – |

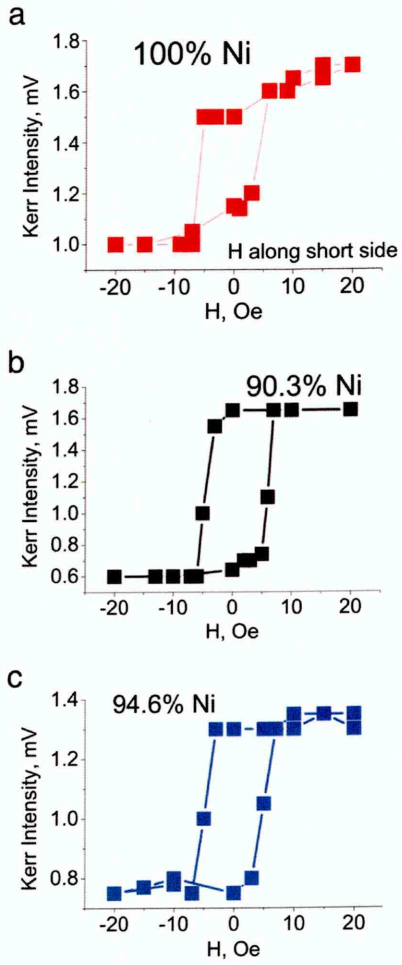


**Fig. 10.** a–c. Comparison of MOKE results for Samples a, b and c. As can be seen b and c are similar whilst a has a slope in values above coercivity.

To understand the effect of pressure on morphology we analyse the fluxes of species to the growing film. The gas ion is likely to be unaffected by pressure as they are created mainly by electron impact which is related to the density of plasma and RF power. This is supported by the constant emission of Ar I (Fig. 5). At the same time the deposition flux to the substrate is reduced significantly due to scattering. These two effects amount to an elevated gas ion-to-metal neutral ratio with pressure and result in enhanced mobility and densification of the microstructure at higher pressures. This is supported by the significantly better side wall coverage for the 14.3 Pa film visible in Fig. 9a. The open top of the via is consistent with gas-induced resputtering at the corner. The increase in ion-to-neutral ratio also drives a shift in the growth mode of the film on the surface from well-defined columnar to dense globular. In comparison, at the lower ion-to-neutral ratio (Fig. 9b) the growth is typical of Zone 2 of the Thornton structure zone diagram, where columns are enlarged and have dense grain boundaries. The column width is similar at the bottom as well as at the top indicating that the texture selection is complete. Already at the interface the grain size is large

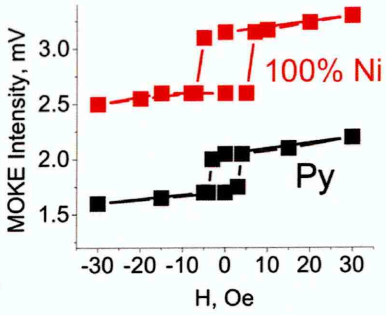


**Fig. 11.** MOKE comparison of pure Ni coating with a standard reference sample of Py (80% Ni, 20% Fe).

indicating that nucleation sites coalesce into larger domains whose subsequent growth is not competitive therefore leading to fast establishment of texture and dense morphology of the film. For the higher pressure of 14.3 Pa, the microstructure seems to be shifting towards the dense Zone T of the Thornton model.

No significant sputtering of the RF coil was observed in these experiments. From Table 3, it can be seen that over process time the contamination by RF-coil material can be reduced to below the detection limit of SEM–EDX. Cu and In contaminants were detected as remnants from other deposition in the chamber. This can be related to an observed net deposition of target material on the coil during the process.

### 3.6. Magnetic properties of the coating

Magnetic properties of the films were measured by Magneto Optical Kerr Effect Spectroscopy (MOKE). MOKE hysteresis loops were obtained from measurements of the polarization angle of a He–Ne laser (wavelength 633 nm, power 0.5 mW and 1 mm beam diameter) in longitudinal geometry where the magnetic field to the sample was applied in the film plane.

As can be seen in Fig. 10a–c, all samples gave a MOKE typical hysteresis response. Fig. 10a shows a slightly different hysteresis curve with a slope in the intensity values above the coercivity values. This sample has the highest Ni purity of the process series shown in Section 3.4. Due to these features, this sample was compared to that of a standard 25 nm permalloy (Py) (80% Ni, 20% Fe) film on glass substrate. Fig. 11 shows the comparison of the hysteresis loops of Ni and Py with the MOKE intensity of Ni being 1.2 times larger than that of Py and approx. doubled coercivity value of 6 Oe. The MOKE response is the product of reflectivity and Kerr rotation [18]. With the Ni showing a MOKE response of 1.2 times larger than Py and the reflectivity of Py and Ni measured to be 0.5, the Kerr rotation of Ni is 0.6 times that of Py. The Kerr rotation is proportional to the magnetisation and for Py is well measured to be 10.0 kG, which is close to the calculated literature value of 9.5 kG [19]. For the Ni coating this corresponds to a magnetisation of 6.0 kG, which is close to the typical magnetisation of Ni in bulk form [19].

## 4. Conclusions

Successful deposition of a magnetic material has been demonstrated by ICIS for the first time whilst achieving high degrees of metal ionisation. The benefits of this are deposition into high aspect ratio structures with good sidewall and bottom coverage. Further a more uniform thickness coating can be deposited on sidewalls due to the perpendicularly approaching electric field lines and high metal ionisation; columns can grow with horizontal orientation on the vertical sidewalls of vias with high aspect ratios.

Calculations of the excitation and ionisation in ICIS processes have shown to be comparable to magnetron based systems up to 3000 W RF-power for Ni. For higher powers further factors increase the ionisation efficiency of sputtered material. At high pressures the coating density was significantly improved due to an increase in gas ion-to-metal neutral ratio.

## Acknowledgements

The authors would like to thank Prof. Olinda Conde and Nikolay Polushkin from the University of Lisbon, Portugal, whose cooperation in the MOKE measurements we greatly appreciate.

## References

[1] R.M. White, J. Magn. Magn. Mater. 88 (1990) 165–176.
[2] M.R.J. Gibbs, et al., J. Phys. D. Appl. Phys. 37 (2004) R237–R244.
[3] D. Niarchos, Sensors Actuators A 109 (2003) 166–173.
[4] S. Rossnagel, Thin Films 27 (2000) 37–65.
[5] K.-H. Müller, Phys. Rev. B 35 (1987) 7906–7913.
[6] A. Anders, J. Phys. D. Appl. Phys. 40 (2007) 2272–2284.
[7] B. Chapman, Glow Discharge Processes: Sputtering and Plasma Etching, 1st edition Wiley-Interscience, 1980.
[8] B. Window, F. Sharples, J. Vac. Sci. Technol. A 3 (1) (1985) 10–13.
[9] K. Yukimura, A.P. Ehiasarian, Nucl. Inst. Methods Phys. Res. B 267 (8–9) (2009) 1701–1704.
[10] D.A.L. Loch, A.P. Ehiasarian, IOP Conf. Ser., Mater. Sci. Eng, 39, 2012, p. 012006.
[11] M.F. Dony, A. Ricard, J.P. Dauchot, M. Hecq, M. Wautelet, Surf. Coat. Technol. 74–75 (1995) 479–484.
[12] S.M. Rossnagel, K.L. Saenger, J. Vac. Sci. Technol. A7 (3) (1989) 968–971.
[13] F. Ochsenbein, P. Bauer, J. Marcout, Astron. Astrophys. Suppl. Ser. 143 (2000) 23–32.
[14] I. Petrov, et al., J. Vac. Sci. Technol. A21 (2003) S.117.
[15] J. Bradley, et al., Plasma Sources Sci. Technol. 11 (2002) 165–174.
[16] S.M. Rossnagel, J. Hopwood, J. Vac. Sci. Technol. B12 (1) (1993) 449–453.
[17] A.I. Linnik, et al., Tech. Phys. Lett. 38 (6) (2012) 499–502.
[18] D. Allwood, et al., J. Phys. D. Appl. Phys. 36 (2003) 2175–2182.
[19] R.S. Tebble, D.J. Craik, Magnetic Materials, 1st edition Wiley-Interscience, 1969.

# APPENDIX B

## Papers Published in Refereed Journals not Directly Related to this Thesis

B.1 Comparison of Al-Si-N nanocomposite coatings deposited by HIPIMS and DC magnetron sputtering

Surface & Coatings Technology 232 (2013) 680–689

Contents lists available at ScienceDirect

Surface & Coatings Technology

journal homepage: www.elsevier.com/locate/surfcoat

# Comparison of Al–Si–N nanocomposite coatings deposited by HIPIMS and DC magnetron sputtering

Erik Lewin [a,*], Daniel Loch [b], Alex Montagne [c,1], Arutiun P. Ehiasarian [b], Jörg Patscheider [a]

[a] Laboratory for Nanoscale Materials Science, Empa, Dübendorf, Switzerland
[b] HIPIMS Technology Centre, MERI, Sheffield Hallam University, UK
[c] Mechanics of Materials and Nanostructures, Empa, Thun, Switzerland

ARTICLE INFO

*Article history:*
Received 14 November 2012
Accepted in revised form 17 June 2013
Available online 24 June 2013

*Keywords:*
Nanocomposites
Coatings
HIPIMS
Plasma characterisation
Mechanical properties
Optical properties

ABSTRACT

This paper presents a comparative study between DC magnetron sputtering (DCMS) and high power impulse magnetron sputtering (HIPIMS) of Al–Si–N. Coatings were synthesised through co-sputtering of Al and Si in a mixed $Ar/N_2$. One set of DCMS experiments and one set of hybrid HIPIMS (Al-target)/DCMS (Si-target) experiments were conducted. It was found that a higher partial pressure of $N_2$ was necessary to obtain fully nitrided material using the HIPIMS process. The Si content of the samples was varied between 0 and 16 at.%. All processes were characterised using optical emission spectroscopy (OES) as well as energy-resolved mass spectrometry (E-MS). The obtained coatings were characterised using X-ray diffraction (XRD), X-ray photoelectron spectroscopy (XPS), scanning electron microscopy (SEM), as well as UV–Vis spectroscopy and nanoindentation.

The HIPIMS processes were found to provide a highly activated growth environment, with $Al^+$ comprising 87% of the total ion flux, compared to 0.6% for the DCMS case, where $Ar^+$ was found to be the dominating species comprising 90% of the total ion flux. Coatings from both HIPIMS and DCMS processes were found to form nanocomposites of a solid solution phase $(Al_{1-x}Si_x)N$ and most likely a $SiN_y$ phase, as shown by XRD and XPS analyses. Compared to coatings from DCMS, samples deposited with HIPIMS had a slightly more textured AlN-phase with smaller grains, as well as smoother and, denser morphology as observed by SEM.

In agreement with previous studies, the coatings had a high transparency in the visual and near IR range; an optical band gap ($E_{04}$) between 4.6 and 5.2 eV and a refractive index between 1.9 and 2.1 was observed. The ternary coatings studied here were found to be hard with the HIPIMS coatings (combined average 22 ± 3 GPa) being harder than their DCMS counterpart (combined average 17 ± 1 GPa). A maximum hardness of 27 GPa was observed for the sample deposited with HIPIMS and a Si-content of 7 at.%.



## 1. Introduction

Nanocomposite coatings of nanocrystalline AlN (or rather the solid solution $(Al_{1-x}Si_x)N$) embedded in an amorphous matrix of $Si_3N_4$ have previously been shown to be hard and transparent for visible light, and thus are useful as scratch-resistant optical coatings [1,2]. Applications as anti-oxidation coatings have also been investigated [3]. Synthesis has been carried out by reactive DC-magnetron sputtering (DCMS), chemical vapour deposition or reactive cathodic arc evaporation. Research into the analysis and understanding of these coatings has been conducted by several groups and the main focus has often been mechanical and optical properties [1–9].

High power impulse magnetron sputtering (HIPIMS) is a recently developed sputtering technique, where very short and intense pulses are used. For detailed reviews the reader is referred to recent reviews by Gudmundsson et al. [10], Sarakinos et al. [11] and Helmersson et al. [12]. The use of very short pulses (typically in the order of 5 to 5000 μs) and low duty cycles (typically below 10%, achieved by a comparably low pulsing frequency, i.e. an off time markedly longer than the on-time) enables very high peak currents and powers (typically a few $kW/cm^2$) to be used, whilst still maintaining an average power within the thermal budget of the target cooling. These high currents and powers raise the plasma density by two orders of magnitude to create an efficient environment for metal ionisation (50 to 90%) and molecule dissociation. This increased ionisation leads to an intense and, through discharge parameters and substrate bias, a controllable bombardment of the growing coating with energetic particles, i.e. of the ionised atoms from the sputtered target materials and the process gases [13]. Such a bombardment, as well as the more reactive plasma, gives new and additional means to control the microstructure of deposited coatings [14]. The HIPIMS process has been shown to enable coatings' deposition with less substrate or bias heating compared to conventional sputtering processes whilst

* Corresponing author, presently at: Dept. of Chemistry - Ångström Laboratory, Uppsala universitet, Sweden. Tel.: +46 18 471 37 68; fax: +46 18 51 35 48.
*E-mail address:* erik.lewin@kemi.uu.se (E. Lewin).
[1] Presently at Laboratoire Interdisciplinaire Carnot de Bourgogne, CNRS - Université de Bourgogne, 9 avenue Alain Savary, FR - 21000 Dijon, France.

0257-8972/$ – see front matter © 2013 Elsevier B.V. All rights reserved.
http://dx.doi.org/10.1016/j.surfcoat.2013.06.076

obtaining smoother coatings with improved adhesion [13] and better step coverage.

Most HIPIMS studies have been using a single target material, mainly using a metallic target, but studies have also been conducted using alloy, composite or sectioned targets in order to synthesise more complex materials. Also combinations of DCMS and HIPIMS on separate magnetrons in combination with rotating substrate carousels have been used to synthesise multilayer coatings [15,16]. The use of HIPIMS and two different targets for confocal co-sputtering to attain a single layer material is less common, but has also been employed using one target in HIPIMS and the second in DCMS mode. No notable difficulties with such a set-up have been observed using metallic or combination of metallic and semi-conductive targets [17–20].

Although coatings in the Al–Si–N system previously haven't been deposited using HIPIMS, AlN coatings have. It was shown that deposition of stoichiometric, transparent AlN is possible with HIPIMS, using an Al target and a mixed $Ar/N_2$ atmosphere, although a higher amount of reactive gas is required to attain stoichiometric material, compared to a DCMS process [21]. This was explained by two factors: firstly the use of current control mode in DCMS and voltage control mode for HIPIMS in combination with the significantly larger secondary electron emission yield of AlN compared to metallic Al [22]; and secondly the ionised and dissociated nitrogen (which are more abundant in a HIPIMS discharge than in a DCMS discharge) react more easily with the Al vapour, and thus pump away some N with Al atoms that do not hit the growing coating but the chamber walls [21]. The HIPIMS discharge of Al in $N_2$ containing atmosphere has also been studied, and it was shown that the ion energy distribution of both $Al^+$ and $N^+$ was considerably shifted to higher energies in a HIPIMS discharge than in a standard DCMS discharge, and that the flux of $Al^+$ was considerably higher for the HIPIMS case [23].

The present work is an initial study into the deposition of ternary Al–Si–N thin films using HIPIMS process, by comparing to a DCMS process in the same deposition system and to the furthest possible extent using identical deposition parameters. The aim is to investigate if, and how, other and possibly more optimised coating microstructures and/or morphologies may be attained compared to a DCMS process. Possible structure modifications include the degree of (metastable) solid solution of Si in the AlN-phase and grain size and general crystallinity. Emphasis is placed on properties which are important for scratch-resistant optical coatings. The present study compares a pure DCMS process (co-sputtering of Al and Si in an $Ar/N_2$ atmosphere) and a reactive hybrid HIPIMS/DCMS process, where the Al magnetron is run in HIPIMS mode and the Si magnetron in DCMS in an $Ar/N_2$ gas mixture. Both processes have been studied in detail with plasma diagnostic tools, and the attained coatings have been characterised with regard to microstructure as well as mechanical and optical properties.

## 2. Experimental details

All experiments were conducted in the same CMS-18 sputter deposition system (Kurt J. Lesker), the layout of which is sketched in Fig. 1. For the present study two 3″ unbalanced planar circular Torus-magnetrons (Kurt J. Lesker), with a closed-field configuration polar and with an angle of 60° between them, were utilised. The base pressure before deposition was $4 \times 10^{-5}$ Pa or lower. The magnetrons were furnished with elemental targets of Al (99.99%) and Si (99.999%, p-type, B-doped). The Si target was powered by a Hüttinger 3000 DC generator which was run through an Advanced Energy SparcLe in active mode for arc suppression; the Al target was in the DCMS case also powered by a Hüttinger 3000 DC generator, and in the HIPIMS case by a Hüttinger HMP2/1 generator. Substrates were mounted on a rotating holder 120 mm from targets, and depositions were carried out simultaneously on Si(001), a-$SiO_2$ and SS304 stainless steel substrates. Prior to introduction into vacuum substrates were cleaned by ultrasonication in acetone and ethanol and finally dried in a hot air stream.

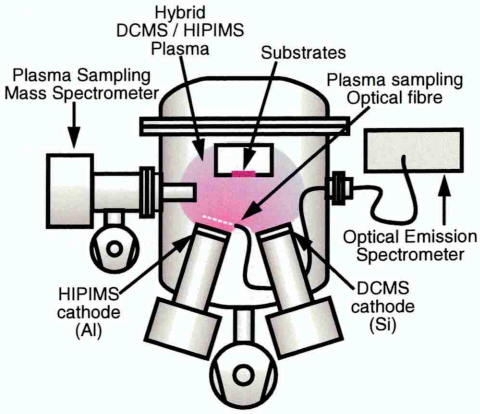


**Fig. 1.** Schematic cross-section of the UHV sputter system used in the present study, showing the positions of the cathodes as well as plasma sampling mass spectrometer and optical emission spectrometer.

Prior to deposition substrates were heated to 200 °C by quartz lamps placed behind the sample holder, this temperature was maintained throughout the deposition. Before each deposition, or process, targets were sputter-cleaned in pure Ar atmosphere of about 0.6 Pa for 3 min. Immediately before deposition substrate surfaces were cleaned by a two minute RF-plasma cleaning using a -100 V bias and an Ar-atmosphere of 0.4 Pa.

The variable deposition parameters are summarised in Table 1, and the processes are described directly below. The Si-target was exclusively run in DCMS-mode, and controlled in constant power mode. Four different powers (0, 40, 80 and 160 W) were chosen to vary the Si content of the coatings. The Al-target was either run in DCMS-mode, at a constant power of 540 W, or in HIPIMS-mode with a time-averaged power of 0.4 kW, a frequency of 160 Hz and a pulse width of 100 μs, giving a duty cycle of 1.6%. One DCMS process and one HIPIMS process (each with three different Si-powers) were studied. Both processes used a constant Ar-flow of 26 sccm (on its own giving a pressure of 0.278 Pa) and a variable $N_2$ flow, maintaining a constant pressure. The DC process used a $N_2$ flow of 14.1–15.5 sccm (i.e. 35–37% reactive gas), giving a total pressure of 0.4 Pa; and the HIPIMS-process was conducted at a higher $N_2$ flow of 23.5–24.6 sccm (i.e. 47–49% reactive gas) giving a total pressure of 0.48 Pa. The HIPIMS discharge was run in voltage control mode, and started with an initial target voltage about 480 V, which was continually (manually) adjusted to maintain a peak power of 34 kW throughout the experiment. The peak power was selected to be between 10 and 100 times the DCMS power to ensure sufficient metal ionisation [14]. The substrates were kept at a floating potential during deposition, which was not measured. Deposition times were varied between 1 h 20 m and 2 h 2 m with the aim of obtaining coatings with a thickness of about 1 μm (which was partly unsuccessful, see results below). The hysteresis experiments were conducted at slightly different parameters, using a fixed voltage of 640 V for the HIPIMS discharge. The reason for this discrepancy is that the parameters of the HIPIMS process had to be altered in order to stabilise the process when running at high $N_2$-flows. The general result of the hysteresis experiments are although still relevant.

The processes were characterised during the depositions and in dedicated sessions with no substrates. Fig. 1 shows a schematic of the analysis set-up. Ion flux chemistry and ion energy were measured by plasma-sampling energy-resolved mass spectrometer (E-MS) model

**Table 1**
Variable deposition conditions together which microstructural parameters for samples are presented in the present study. The base pressure before deposition was in all cases $4 \times 10^{-5}$ Pa or lower, and the deposition pressure and Ar gas flow were constant at 0.40 Pa and 26.0 sccm, respectively. All coatings were deposited at a temperature of 200 °C and floating substrate bias was used. "n/a" signifies that no measurement was performed, "–" signifies that no crystalline phase was observed. Error values correspond to 90% confidence intervals.

| Sample | Al-target | | Si-target | | $N_2$ flow (sccm) | Composition (at.%) | | | | Thickness (μm) | Deposition rate (μm/h) | Bond length (Å) | Grain size (nm) |
|---|---|---|---|---|---|---|---|---|---|---|---|---|---|
| | Type | (W) | Type | (W) | | Al | Si | N | O | | | | |
| D0 | DCMS | 540 | DCMS | 0 | 15–16[a] | 44 | 0 | 42 | 14 | n/a | n/a | 1.872 ± 0.001 | 15 ± 2 |
| D1 | DCMS | 540 | DCMS | 40 | 14.1–14.7 | 42 | 3 | 47 | 9 | 1.0 | 0.46 | 1.857 ± 0.004 | 15 ± 6 |
| D2 | DCMS | 540 | DCMS | 80 | 14.5–14.9 | 38 | 6 | 48 | 8 | 1.1 | 0.52 | 1.857 ± 0.004 | 10 ± 4 |
| D3 | DCMS | 540 | DCMS | 160 | 15.1–15.5 | 30 | 14 | 53 | 1 | 1.2 | 0.60 | – | – |
| H1 | HIPIMS | 400 | DCMS | 40 | 24.3–24.6 | 43 | 3 | 52 | 2 | 0.40 | 0.31 | 1.859 ± 0.007 | 7 ± 1 |
| H2 | HIPIMS | 400 | DCMS | 80 | 23.9–24.3 | 39 | 7 | 53 | 2 | 0.65 | 0.32 | 1.860 ± 0.003 | 6 ± 2 |
| H3 | HIPIMS | 400 | DCMS | 160 | 23.9–25.3 | 30 | 16 | 53 | 1 | 0.60 | 0.44 | – | – |

[a] Deposited at a later occasion, and thus with a slightly different setting to the (manually set) throttling of the turbo pump, and hence slightly different gas flows were required to maintain the set deposition pressure.

PSM002 (Hiden Analytical Ltd.) with grounded orifice, Bessel box energy filter, quadrupole mass filter and SEM detector, mounted in the vicinity of the substrate, almost perpendicular to the plane of Fig. 1, as described earlier [24]. The spectrometer was driven in time-averaged mode with an extractor grid set at -10 V. Ionisation degree of metal and nitrogen were studied in time-averaged mode by optical emission spectroscopy (OES) using a Triax 320 monochromator with CCD detector (Horiba Jobin Yvon) and resolution of 0.12 nm. Light emission was collected in vacuo by a collimated quartz fibre sampling the volume 30 mm above the Al target.

The coatings were analysed using X-ray diffraction (XRD) and X-ray photoelectron spectroscopy (XPS). XRD was performed using a Bruker D5000 diffractometer utilising Cu Kα radiation and using low incident angle and a secondary side parallel plate collimator with an acceptance angle of 0.40° for grazing incidence scans, and Bragg–Brentano optics for θ/2θ-scans; both using a Ni-filter to reduce Cu Kβ-radiation. GIXRD was performed on samples deposited on Si(100) substrates and θ/2θ-scans on samples deposited on a-$SiO_2$ substrates. XPS was performed on a Physical Electronics Quantum 2000 Micro-ESCA spectrometer, using samples deposited on Si. Compositions were determined by depth profiles using 4 keV $Ar^+$, and elemental sensitivity factors provided by the instrument manufacturer (which by previous comparison with ion beam analysis have proved reliable for the present materials system). High resolution spectra for chemical analysis were obtained after a more careful sputter-etching: 5 min using 1 keV $Ar^+$, conditions at which no sputter-induced damaged or artefacts have been observed. Charge referencing was done using Au ($E_B$ of the Au $4f_{7/2}$ peak set to 85.20 eV), which was redeposited from the clamp holding the sample during sputter-etching; this method has been described in detail and evaluated previously [4,5].

The coating morphology was observed by scanning electron microscopy (SEM) using a FEI NanoSEM 230, operated at 15 kV in high-vacuum mode. Prior to measurements samples were coated with a thin carbon layer by evaporation to improve conduction. No artefacts from the carbon coating could be observed at the used magnifications on the fractured (and smooth) substrate surfaces, thus ensuring that observed structures in the coating are features of the studied material.

Optical measurements of the coatings to determine the transmission, absorption coefficient and refractive index were performed using a Shimadzu UV-3600 UV–Vis–NIR spectrometer. Data were evaluated using the envelope method, which allows the determination of the above mentioned parameters from a single transmission spectrum with interference fringes [25,26]. The presented values for optical constants as function of wavelength have been attained through interpolation between the values at the fringe positions.

Mechanical properties of the coatings were determined by nanoindentation. Indentations were performed with the Hysitron Ubi (Minneapolis, USA) equipped with a Berkovich diamond tip. The shape of the probe has been calibrated using a reference material of well-known elastic modulus: fused silica (E = 72 GPa). Indentation tests on coatings were carried out 10 μm from each other to avoid any interaction between imprints. For the majority of samples two maximum loads (1.5 and 2 mN, respectively) were applied, leading to a maximum penetration depth ranging from 25 to 50 nm. This ensured that the total penetration of the film was less than the recommended maximum of 10% of the film thickness [27]. For the thinnest sample no plastic deformation was achieved at these loads. In this last case a large number of indents with different loads were performed over a wide range of loads (from 1.5 to 6 mN), and the stated values are from a depth where the hardness and Young's modulus were found to be independent of depth, but still in an acceptable range regarding to the film thickness. Mechanical properties were obtained from the unloading curve using the method of Oliver and Pharr [28].

Macroscopic stresses were determined for coatings deposited on Si measuring the wafer curvature by profilometry and calculating the stress through the corrected Stoney's equation [29–31]. For the calculations the literature values of the biaxial modulus for Si(100) was used [31]. Measurements were performed using a Tencor P10 needle profilometer, with three pairs of orthogonal, 5 mm longs scans from which an average stress was calculated.

## 3. Results and discussion

### 3.1. Processes — general observations and hysteresis experiments

Hysteresis experiments were conducted with constant pumping speed, Ar-flow (27 sccm), DC target power (Si: 80 W, Al: 540 W when applicable) and HIPIMS ignition voltage (at 640 V when applicable); the flow of reactive $N_2$ gas was varied. Data from these experiments are shown in Fig. 2.

The DCMS-process showed the expected behaviour known from previous studies, see Fig. 2 (blue curves). There are several observations that point to target poisoning above a reactive gas flow of 8 sccm, see bold arrows: A slight change in the slope of the pressure curve (a), a change in slope of the Si-target voltage curve (b) and a small hysteresis in the Al-target current (c). The chosen working conditions for the DCMS-process (about 15 sccm) are thus in fully poisoned mode, ensuring fully nitrided coatings (fully transparent coatings and no Si–Si bonds observed in XPS, see below). The levelling out of the Al-target current above 11 sccm is due to the current limit of the power supply. This is also the reason that no higher reactive gas flows were investigated for the DCMS process. The relatively small hysteresis effect is probably due to sufficient pumping speed of the vacuum system, as explained by the Berg model [32].

Results from hysteresis experiments for the HIPIMS process are also shown in Fig. 2 (red curves): one experiment with $N_2$-flows

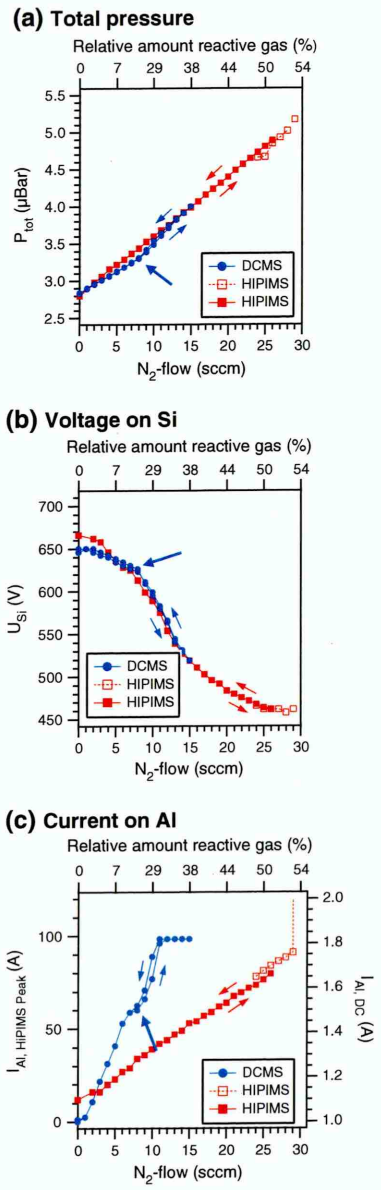


**Fig. 2.** Data from hysteresis experiments on respective process: (a) Total pressure, (b) voltage on Si target and (c) current on Al target. Data shown from both DCMS (●, blue) and HIPIMS (■ and □, red). From the HIPIMS two experiments are shown, the first (solid line, ■) reverses at 26 sccm $N_2$ and the second (□, dashed line) starts at 24 sccm, and reverses at 29 sccm $N_2$. Bold arrows mark indications of poisoning in DCMS-process and thin arrows show directions of increasing and decreasing gas flow in the experiments.

0–24–0 sccm (solid squares), and a second experiment where data points are for flows larger than 24 sccm $N_2$ (open squares). Up to a $N_2$-flow of 25 sccm no hysteresis or other indications of a poisoning can be observed: the pressure (a) and the observed peak power of the HIPIMS-discharge (c) increase linearly, and the decrease in Si-target voltage (c) is steady and without distinct breaks. Up to this point, decreasing the nitrogen flow gives data points which perfectly overlap those attained whilst increasing the reactive gas flow (see solid squares). Above 25 sccm of reactive gas flow (see open red markers and dashed line in Fig. 2) there is a sudden change in the HIPIMS-process, indicating a complete target poisoning. Exactly at which flow this poisoning occurs was found to be strongly dependent on how fast the flow was increased — for the experiment shown in Fig. 2 it occurred at 29 sccm. The poisoning was characterised by a drastic increase in peak current that reaches the arc suppression limit of the power supply (in this case 280 A) within 3 μs and stops the HIPIMS-pulse prematurely, and thus prevents any significant sputtering of the target and the process operates in poisoned mode and only returns to a 'normal' state only upon a reduction of the $N_2$ flow below 8 sccm (not shown in graph). Thus the process is unstable above reactive gas flows of 25 sccm, and is due to power supply limitations at risk of getting stuck in poisoned mode. The observed current-increase of the Al-target as it is poisoned is also observed for the DC-process (although less drastically), and is both cases most likely due to the 130% increase in the secondary electron emission yield of AlN compared to Al [22].

Samples deposited with the HIPIMS-process at a $N_2$ flow of 15 sccm were found to be not fully nitrided, visible by inspection as coatings had a slight yellow colour, and confirmed by high resolution XPS, which showed small contributions from Si – Si bonds. Thus, the working point of the HIPIMS-process was chosen as close to the total poisoning point as possible, i.e. at ca. 24 sccm, which produced fully nitrided material (fully transparent coatings and no Si – Si bonds observed in XPS, see below). The observation, that a higher partial pressure of $N_2$ is required for fully nitrided Al–(Si)–N material using HIPIMS, is in agreement with literature where deposition of AlN using HIPIMS and pulsed DC processes have been compared, and referred to the different control modes of DCMS and HIPIMS discharges (also applicable here) as well as increased reactivity of ionised and dissociated nitrogen, see the Introduction section and Guillaumot et al. [21]. As would be expected, a weak trend in $N_2$-consumption is also observed for both processes, as Si-target power is increased slightly more $N_2$ is required to maintain the set deposition pressure, see Table 1.

The working conditions at ca. 24 sccm $N_2$ were found to work well when running the Si-target at 80 or 160 W, but for a Si-power of 40 W the process became unstable and fell into the poisoned mode. The plasma from the Si-target (if intense enough) thus acts to stabilise the HIPIMS-discharge. The reason for this is most likely that a running Si target provides a $N_2$ pump thus further reducing the risk of poisoning the Al target; furthermore the Si target discharge provides charge carriers to assist the ignition of HIPIMS plasma at lower voltage than is required for independent operation. Without such assistance a binary AlN reference sample could not be synthesised using the HIPIMS process, this was done with the DCMS process.

The deposition rates of the HIPIMS-processes (0.31–0.44 μm/h) were consistently found to be lower than that of the DC-processes (0.46–0.60 μm/h) using the same Si target powers (40, 80 and 160 W) and a constant settings for the Al target. As expected, the deposition rate is increasing for both processes with Si-target power, see Table 1. A decrease in deposition rate for HIPIMS compared to DCMS using the same average power is well known for most materials [10,12,33]. In this context it is interesting to note that these deposition processes yield almost identical compositions with regard to Al, Si and N (see below and Table 1) despite the Si target being operated at identical powers, and only the process on the Al target is changed from DC to HIPIMS. This observation may be explained by an increased re-sputtering at the growing film surface for the HIPIMS-process. This increased re-sputtering at the growing coating is caused by the increased energy of the ions in the plasma (see plasma

analysis below), and can due to the similar mass of Al and Si not be expected to cause any preferential sputtering and thus the composition of the deposited material is retained. It should also be noted that the magnetrons, in a closed-field configuration, and the HIPIMS discharge may also influence the plasma density of the DC discharge above the Si target.

### 3.2. Processes — plasma characterisation

The same processes used to deposit coatings were also characterised using E-MS and OES. Results are given in Figs. 3 and 4, respectively, and summarised below. Within each process series (DCMS and HIPIMS) the differences were very minor, i.e. the power of the Si target had little or no influence on the attained OES or E-MS spectra. This is demonstrated by comparing Fig. 3a and b, where the second data-set was acquired with the Si-target on (80 W) and still only showing negligible amounts of $Si^+$ ions at the substrate position. Thus only one representative set of data for each process type is given.

The time-averaged ion energy distribution functions (IEDFs) of different species are shown in Fig. 3, and the relative amounts of observed species are given in insets. As can be seen, there are distinct differences between the two processes, with the HIPIMS generating a much greater flux of energetic ions (up to ~40 eV) than the DCMS process (energies up to ~20 eV). The high energy tail observed for the HIPIMS process also leads to higher average energies for respective species, with the average energy of $Al^+$ increasing from 2.3 to 4.3 eV, and from 0.9 to 2.3 for $Ar^+$. For the DCMS process the dominating species is $Ar^+$ (90%), which is in agreement with literature on reactive processes using conventional DC discharges [34]. The HIPIMS process, on the other hand, shows an equally large domination by $Al^+$ (87%). The HIPIMS process shows only a minor contribution from $Ar^+$ (0.6%), which indicates a strong gas rarefaction in front of the target. For both processes the ion species may be divided in four groups, with internally similar IEDFs: the directly ionised gas species $Ar^+$ and $N_2^+$; the dissociated and ionised $N^+$ together with the metallic $Al^+$; the doubly ionised ions $N^{2+}$and $Ar^{2+}$; and finally the very minor contributions from $AlN^+$ clusters and $Si^+$ from the second (DCMS) discharge. In the DCMS process the directly ionised gas species are dominating ($Ar^+$ and $N_2^+$ summing up to 93%), and show maxima at low energies with a rapid fall-off in intensity for higher energies. In the HIPIMS process these contributions are heavily reduced due to gas rarefaction, caused by the intense metal ion flux from the target. The HIPIMS process is totally dominated by the second group ($Al^+$ and $N^+$ summing up to 98%). These IEDFs are for both processes broader without distinct peaks and have a less steep fall off than the first group. Thus these species comprise the high energy contribution, and the interaction of the gas with the highly energetic sputtered metal flux results in gas heating and reduction in the low energy group (i.e. $Ar^+$ and $N_2^+$). For both cases the contribution of doubly ionised species is minor, although there is a clear increase for the HIPIMS compared to the DCMS process. This is illustrated by the $N^+/N_2^+$ ratio of 22 for HIPIMS and 1 in DCMS.

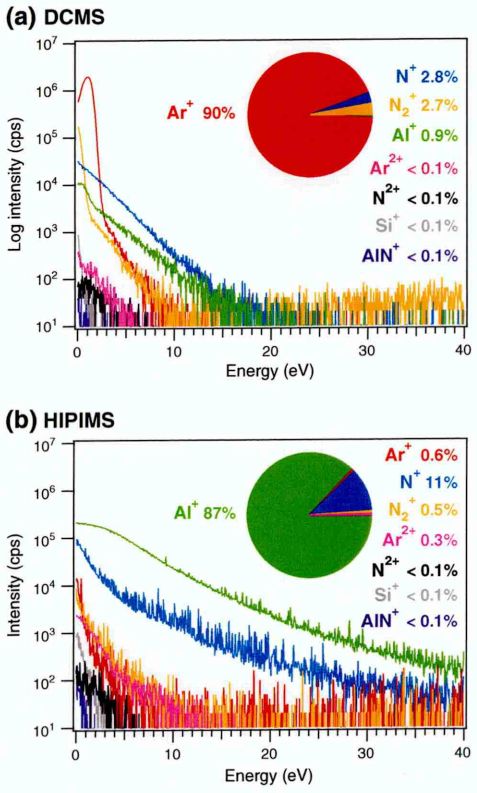


**Fig. 3.** Results from energy resolved mass spectroscopy measurements of the plasmas, showing ion energy distribution functions (IEDFs) from respective process: a) DCMS (Al @ 510–530 W, Si-target not run) and b) HIPIMS (Al @ 400 W, Si @ 80 W). Insets show total integrated area under respective IEDF.

These findings are in general agreement with previous plasma studies of HIPIMS of Al in a nitrogen containing atmosphere. The main difference is higher flux and energies for $N^+$ in the present study compared to literature [23]. For HIPIMS there is a much larger amount of $Al^+$ than $Ar^+$. The combination of a grounded orifice and a relatively high first-grid extraction potential (-10 V) could give rise to artefacts in the relative amounts, but cannot account for the difference in ion flux between Al and Ar ions observed here.

Selected regions of optical emission spectra of DCMS and HIPIMS are given in Fig. 4, normalised to the emission intensity of $Ar^0$ (at 749.5 nm). Strong $Al^+$ ion emission was observed in HIPIMS whereas it was below the detection limit for DCMS, which indicates a higher metal ionisation degree in the former case. Also the nitrogen gas ionisation is increased, as indicated by the $N_2^+/N_2^0$ emission ratios, which is increased by factor of 2 in HIPIMS compared to DCMS. We can also observe substantially increased amounts of excited (i.e. emitting) Al neutrals, which is an indication of a larger metallic contribution to the plasma.

### 3.3. Composition, phase- and microstructure

The compositions of the coatings deposited with the DC- and HIPIMS-processes are shown in Fig. 5 and Table 1 (where some process parameters are summarised with chemical and structural parameters of the resulting coatings). In general, the two series show similar results, and the Si/Al-ratio increases as Si target power is increased. Si contents between 0 and 16 at.% are obtained. The N-content is around 50 at.% and thus indicates fully nitrided material. The main difference between the series is the O content, which is substantial (8–9 at.%) for the low and medium Si-content coatings deposited with DCMS (D1 and D2). All the HIPIMS-coatings have less than 2.5 at.% oxygen. The base pressure for the oxygen-rich depositions were not distinctly higher for these depositions compared to others; however the structure of the DCMS coatings as observed in SEM cross sections (see below) is less dense. The observed O-content is therefore considered mainly to be an effect of post-deposition oxidation which penetrates along voids in the under dense coatings.

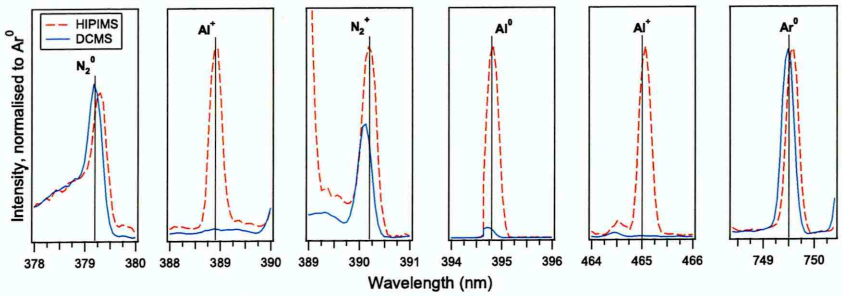


**Fig. 4.** Results from plasma characterisation of respective process using optical emission spectroscopy (OES), showing selected spectral regions (each 2 nm wide) with specific spectral lines. Spectra from both DCMS (blue solid line) and HIPIMS (red broken line) processes are shown.

Nevertheless, oxygen is present in the material and is likely to impact coating performance as discussed in the 'Mechanical properties' section.

High resolution XPS spectra (see Fig. 6) show that coatings deposited with both processes are fully nitrided — observed binding energies of Al 2p (73.6–74.0 eV), Si 2p (101.0–101.6 eV) and N 1s (396.6–396.8 eV) agree (possibly with a small systematic shift to lower binding energies) with previous studies for Al–Si–N material and indicate that Al and Si are both bonded to N, without any significant contribution from metallic Si–Si (at 99.6 eV) and Al–Al (at 72.9 eV) bonds [2,5,35]. Also the binding energy difference between the peaks only differs slightly from previous observations of ternary Al–Si–N coatings, thus supporting that both Al and Si are solely bonded to N. Besides the change in intensity (not visible in Fig. 7 due to normalisation), the only other systematic difference between the samples was a slight shift of the Si 2p peak to lower binding energies, as the Si-content increased. These observations are in agreement with previous studies [2,5].

Diffractograms from GI-scans are shown in Fig. 7; all observed peaks can be indexed to the wurtzite AlN-structure [37]. In agreement with previous studies the crystallinity decreases (peak intensity decrease and peak width increase) for higher Si contents [1,2]. Coatings with the highest Si-content (14–16 at.%) have no peaks and are thus X-ray amorphous. In all four coatings with crystalline AlN, peaks from many different lattice planes are observed, signifying that the samples are polycrystalline with a mainly random orientation of the grains. However,

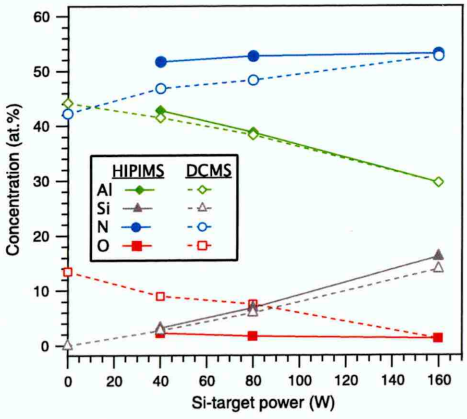


**Fig. 5.** Composition of the coatings in the HIPIMS (filled markers, solid lines) and DCMS (open markers, dashed lines) sample series, as determined by XPS sputter depth profiles. Lines are only intended as guides for the eye.

comparing Fig. 7(a) and (b) differences in the relative intensity of the different diffraction peaks can be observed between DCMS and HIPIMS deposited coatings, this indicates that there are differences in the preferential orientation of AlN crystallites. Further measurements with θ/2θ geometry (not shown) reveal that the ternary samples deposited with HIPIMS have a distinct (002) texture, whereas the ternary samples deposited with DCMS are more randomly oriented, but still with a preferred (002) orientation. The binary AlN reference sample deposited with DCMS also shows a preferred (002) texture, which is the most common growth direction of sputtered AlN coatings under a wide range of conditions [37,38]. It should although be noted that other crystalline directions are also present, as is evident by the GIXRD scans shown in Fig. 7, thus the texture is not perfect for any of the coatings in the present study. The more pronounced texture in the coatings deposited with HIPIMS is probably an effect of the more energetic particle flux for this process (see above). An increased bombardment of the growing film with energetic particles will increase the adatom mobility. This has previously been shown to increase the crystallinity of sputter-deposited AlN [37]. This increased adatom mobility can be part of the explanation of the smoother morphology observed in SEM (see below). Similar observations have previously been made for TiN deposited by HIPIMS [14,39].

The peak positions of the samples are consistently shifted to slightly higher diffraction angles compared to the literature reference, thus indicating a lattice contraction, see Table 1. Assuming a wurtzite unit cell with the c/a-ratio of pure AlN (1.60) the bond length is determined to be 1.854–1.861 Å. This should be compared to 1.872 Å for the pure AlN coating and bulk reference from literature which gives 1.868 Å [36]. This lattice contraction is larger than what can be caused by the observed coating stress (see below). Furthermore, the contraction is observed in GIXRD-scans, which probes different spatial directions depending on 2θ-angle, and since no 2θ-dependence of the contraction is observed it cannot be the result of coating stress. These observations are consistent with previous studies, where a solid solution of Si in AlN, i.e. $(Al_{1-x}Si_x)N$, has been observed with a saturation concentration of about 6 at.% to cause such lattice contractions [1,2]. With regard to the lattice parameter, no statistically significant difference could be observed between the samples deposited with DCMS and HIPIMS processes. There are also differences in peak broadening between the samples; this is interpreted as a change in crystallite size. An estimation of grain sizes through Scherrer's equation [41] gives values between 10 and 30 nm, generally decreasing with Si content, see Table 1. Smaller sizes are found for samples deposited with HIPIMS compared to their DCMS-counterparts. Both these observations are in agreement with literature, where Si is found to cause grain refinement [1,2]; and previous observations that the intense ion-bombardment from a HIPIMS discharge can cause grain refinement, see e.g. Alami et al. [41]. It has however also been observed, e.g. in the case of CrAlSiN, that HIPIMS-deposited nanocomposites exhibit larger grain size compared to DCMS

deposited coatings [17]. These different effects of switching from a DCMS to a HIPIMS process can be understood from the fact that energetic particles can, dependent on the individual particle energy as well as the total energy of the particle flux, facilitate higher crystallinity by increased adatom mobility but they can also disturb the crystalline growth through implantation and collision cascades.

It can thus be concluded that the samples consist of nanocrystalline (nc-) $(Al_{1-x}Si_x)N$, and considering the total compositions and previously observed limit of solid solution [1,2,5,6], at least the medium and high Si content samples must contain a second phase acting as a tissue or matrix phase. This second phase must be composed of $SiN_y$. Hence samples are either single phase solid-solution nc-$(Al_{1-x}Si_x)N$ (low Si-content) or nanocomposites of $(Al_{1-x}Si_x)N$ and $SiN_y$. The relative amount of both phases cannot be determined from the present data, as the exact compositions of the phases (x and y, respectively) cannot be determined with sufficient certainty from XRD and/or XPS data. The peak shift in XRD shows a solid solution, but the uncertainties (including different stress in the coatings) and spread of the observed bond lengths makes it impossible with any certainty to determine x with the help of previous data. Also the XPS data is here of little help, as the different bonding contributions (N–Si and N–Al, respectively) cannot be separated.

SEM-images of fractured cross sections of the coatings are shown in Fig. 8. It is easily observed that the coatings deposited with HIPIMS (lower part of Fig. 8) have both smoother surfaces and cross sections. This difference in morphology, along with the absence of internal voids, is typical of the HIPIMS process [10–12] and is caused by higher average ion energy (as observed in IEDFs, see above), higher ion-to-neutral ratios, higher metal ionisation degree and higher dissociation degree of molecules. All this enhances the adatom mobility on the growing coating. Adatom mobility of $Al^+$ is expected to increase also due to the ~2 eV rise in an average energy observed in IEDFs. This is important as Al is the heavier film-forming element and such energy enhancements are sufficient to allow significantly higher fraction of adatoms to overcome surface diffusion barriers, acquire longer diffusion lengths, form larger nucleation islands and promote layer-by-layer growth. This may lead to stronger texture and a more homogeneous growth front, less shadowing and denser coating morphology.

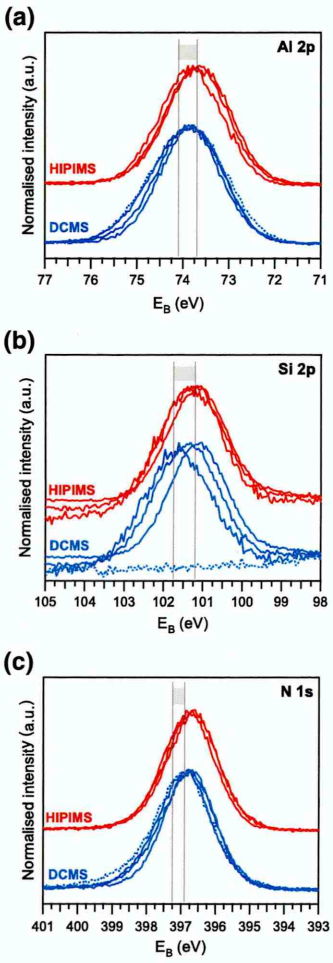


**Fig. 6.** High resolution XPS spectra from samples deposited by HIPIMS (top, red) and DCMS (bottom, blue). The spectra have been normalised. Binding energy scale referenced with $Au4f_{7/2}$ fixed at 85.2 eV. Dotted line is the binary AlN-reference sample. Grey lines and areas mark literature ranges for Al–Si–N coatings using the same charge referencing method [5].

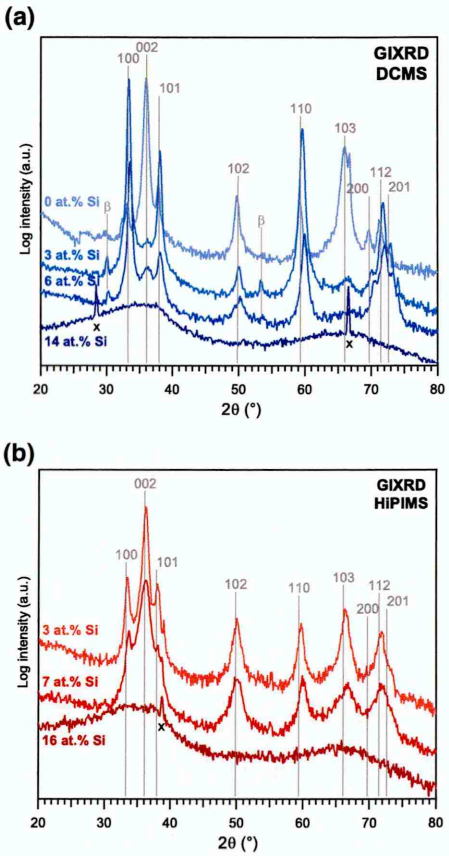


**Fig. 7.** Diffractograms from GIXRD-scans of samples deposited by DCMS (a) and HIPIMS (b). Si-content is increasing downwards in graphs. Literature positions for wurtzite AlN shown by vertical lines and indices [36], peaks due to Cu Kβ-radiation marked with "β" and peaks due to Si-substrate marked with "x". Please note logarithmic y-scale.

These different microstructures are most likely at least partly responsible for the higher O-content observed for the coatings deposited with the DCMS-process, see above. Furthermore, droplets (diameter < 150 nm) are observed for coatings deposited with the HIPIMS-process. Finally, it can be observed that cross sections become more fine-grained/featureless as Si-content increases, which is in agreement with literature and XRD observations above [1,2,8].

### 3.4. Material properties

#### 3.4.1. Mechanical

Results from nanoindentation measurements on samples deposited with DCMS and HIPIMS are shown in Fig. 9, and obtained values are given in Table 2. As can be seen, both Young's modulus and hardness are systematically higher for the coatings deposited by HIPIMS, compared to their DCMS counterparts. For both deposition processes a hardness maximum is found for medium Si-content (D2 and H2 samples), which should as noted above correspond to a small amount of $SiN_y$ tissue phase around the $(Al_{1-x}Si_x)N$ crystallites. This is thus in agreement with literature [1,35] where a hardness maximum is found for small tissue phase thicknesses and explained as nanocomposite hardening. The attained hardness values for the ternary DCMS-deposited coatings (15–19 GPa) are lower than those previously have been attained using DCMS (up to about 30 GPa) [1,2]. An explanation for this could be in the larger target to substrate distance and a different target configuration in the present deposition system, both leading to a reduced plasma density at the substrate surface, and thereby lower adatom mobility and under dense and thus softer coatings. The coatings deposited with HIPIMS, on the other hand, show hardness values (21–27 GPa) in good agreement with what previously has been attained using DCMS. The same trends as observed for the hardness are also observed for the Young's modulus, where 163–171 GPa and 132–178 GPa were attained for DCMS and HIPIMS deposited coatings, respectively. Both the H/E and the $H^3/E^2$ values are systematically higher for the coatings deposited with HIPIMS, see Table 2. This indicates that these coatings are tougher and more resistant to plastic deformation, than their DCMS counterparts. It is also interesting to note that both measures indicate that the medium Si-content coatings (D1 and H1) are the toughest coatings.

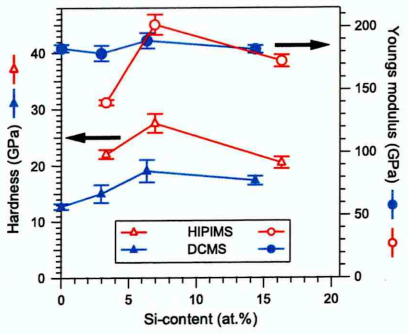


**Fig. 9.** Mechanical properties (hardness △ and elastic modulus ○), as measured by nanoindentation. Samples from DCMS-series shown with solid, blue markers and from HIPIMS-series with open, red markers. Error bars indicate 95% confidence intervals.

Macroscopic stresses calculated via Stoney's equation were in general low: absolute numbers below 0.5 GPa, see Table 2. The DCMS-process yielded coatings with slightly tensile stresses, and the coatings deposited by the HIPIMS-process were found to have no, or slightly compressive stresses. Also for the thin HIPIMS-sample the observed stress of -0.5 GPa gave rise to a clear substrate deflection, for the two other thin coatings deflection was less clear but the absolute stress must thus be below 0.5 GPa. The low stresses leads to the conclusion that the above hardness increase for coatings deposited with HIPIMS cannot be explained by an increase in coating stresses, and is thus ascribed to the different microstructure.

For the present study, the interesting finding is the differences between samples deposited in the same chamber using DCMS or HIPIMS

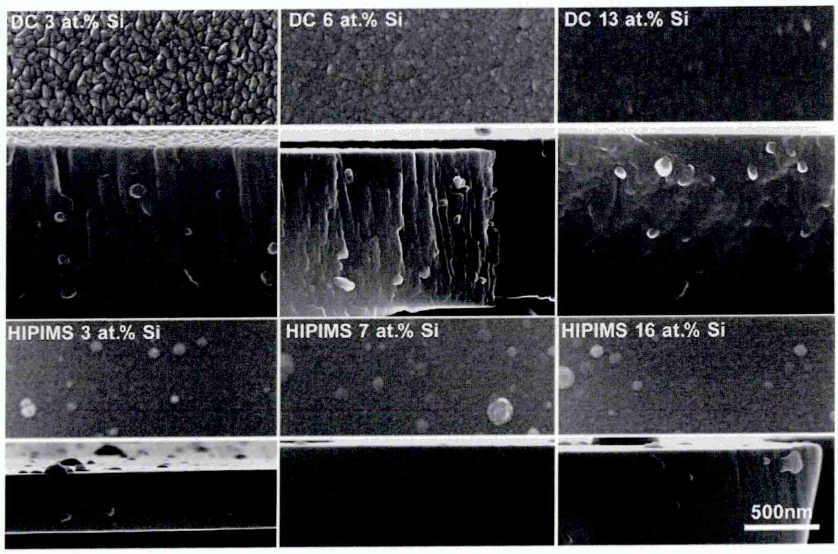


**Fig. 8.** SEM images of samples from both DCMS (top half of figure) and HIPIMS (bottom half of figure) processes. Fractured cross section of respective samples shown directly below top-view with annotation. The scale bar is valid for all images.

**Table 2**
Mechanical and optical properties of the studied coatings. Error values correspond to 95% confidence intervals. "n/a" signifies that no measurement was performed.

| Sample | H (GPa) | Y (GPa) | H/Y | $H^3/Y^2$ (GPa) | Stress (GPa) | n | $E_{04}$ (nm) | $E_{04}$ (eV) |
|---|---|---|---|---|---|---|---|---|
| D0 | 12.7 ± 0.5 | 183 ± 3 | 0.07 | 0.06 | n/a | n/a | n/a | n/a |
| D1 | 15.0 ± 1.6 | 179 ± 6 | 0.08 | 0.11 | 0.46 ± 0.02 | 1.97 | 238 | 5.2 |
| D2 | 19.0 ± 2.0 | 189 ± 6 | 0.10 | 0.19 | 0.25 ± 0.07 | 1.99 | 246 | 5.0 |
| D3 | 17.3 ± 0.8 | 182 ± 3 | 0.10 | 0.16 | 0.49 ± 0.05 | 2.02 | 267 | 4.6 |
| H1 | 22.0 ± 0.8 | 140 ± 2 | 0.16 | 0.54 | -0.02 ± 0.09 | 2.02 | 259 | 4.8 |
| H2 | 27.5 ± 1.7 | 202 ± 8 | 0.14 | 0.51 | -0.04 ± 0.04 | 2.05 | 258 | 4.8 |
| H3 | 20.5 ± 1.0 | 173 ± 5 | 0.12 | 0.29 | -0.48 ± 0.17 | 2.03 | 263 | 4.7 |

processes, respectively. As has been seen from the plasma characterisation (see Figs. 3 and 4) the HIPIMS process has a significantly larger amount of ions, as well as higher ion energies. Both these conditions can contribute to increased adatom mobility and densification through bombardment, and thus explain the apparently denser and smoother HIPIMS coatings (see SEM images in Fig. 8). This difference in microstructure is probably a large part of the explanation for the enhanced hardness and resistance to plastic deformation of the HIPIMS coatings compared to the DCMS coatings.

Comparing with literature it can be noted that similar hardness values (25–30 GPa) have been attained previously for Al–Si–N materials deposited by DCMS. These reports although pertain to samples that either differ in morphology, or microstructure and composition: Pelisson et al. report on high hardness for nanocomposite samples (i.e. as the present results) that exhibit a columnar morphology (i.e. in contrast to the present results) [1,2]; Musil et al. report high hardness and toughness for amorphous coatings with Si-content above 25% (i.e. different from the present results) with a featureless cross section (i.e. similar to the present results) [8]. These results thus show that there are several ways to attain hardness values of 25–30 GPa for Al–Si–N coatings, e.g. by variation of deposition conditions (as performed in the present study), or by variation of composition (as described in ref [8]). This opens up for the possibility of further optimisation of the deposition conditions and composition, and it is well possible that even harder and tougher coatings may be produced if the HIPIMS process can be optimised further. It is worth mentioning that the denser structure of the HIPIMS films is also likely to result in better environmental resistance, as oxidation or other forms of corrosive processes will be slower in a dense structure compared to a columnar structure with large amounts of internal surface diffusion paths.

*3.4.2. Optical properties*

Both coating series are transparent to the eye, and on reflective substrates (such as polished Si) interference colours are observed. UV–Vis–NIR measurements confirm these initial observations; typical spectra are shown in Fig. 10. As can be seen, there is for all samples more than 50% transmission above 300 nm (for coatings that are 0.4 to 1.2 μm thick). From these spectra the optical band gap ($E_{04}$, i.e. the energy at which the absorption coefficient passes $10^4$ $cm^{-1}$) and the refractive index of the materials can be determined, these are given in Table 2. The optical band gap, $E_{04}$, is found to vary between 4.6 and 5.2 eV, generally decreasing slightly with Si content. The values are slightly lower for the HIPIMS-deposited coatings (4.7–4.8 eV), compared to the DCMS-deposited coatings (4.6–5.2 eV). The refractive index at 633 nm is found to vary between 1.97 and 2.05, which is consistent with previous observations from the Al–Si–N-system. The HIPIMS-deposited samples consistently have a slightly higher refractive index than their DCMS-counterparts, which could be an indication that these samples have a thicker $SiN_x$-matrix phase [2], possibly an effect of the smaller grain sizes or a change in the solubility-limit of Si in AlN. Furthermore this could be brought about by the significantly denser grain (column) boundaries in the HIPIMS films.

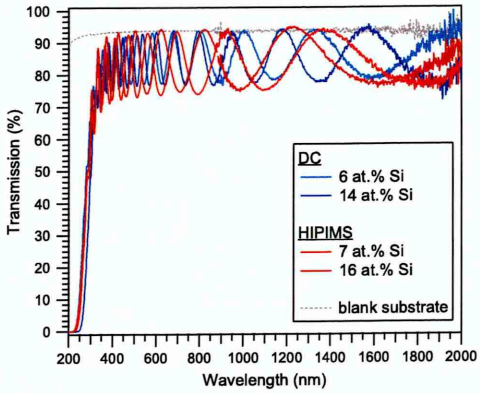


**Fig. 10.** Typical optical transmission spectra for the deposited Al–Si–N coatings. Here medium and high Si-content samples deposited with both DCMS and HIPIMS processes are shown.

## 4. Concluding remarks

The present initial study has compared the deposition of ternary Al–Si–N coatings using DCMS and HIPIMS. Ternary coatings were generally found to contain $(Al_{1-x}Si_x)N$ solid solution phase (possibly with an amorphous $SiN_y$ matrix phase, thus being nanocomposites) or to be X-ray amorphous depending on their atomic composition. HIPIMS deposition conditions containing high amounts of metal ions and dissociated nitrogen resulting in the formation of dense coatings with slightly more textured crystalline phase, and a higher hardness of the coatings. In contrast DCMS deposition conditions with lower degrees of ionisation and dissociation promoted a more random columnar, grainy and open morphology. This resulted in softer and more oxidised material, compared to the coatings deposited by HIPIMS. In the case of HIPIMS, hardening is achieved without addition of stress on account of increased structural density. Together with previous results this indicates that even harder coatings can be attained through further process optimisation. Also the optical properties were slightly affected by the different processes, which could be explained by a higher density of coatings deposited with HIPIMS. Continued studies of the use of HIPIMS to deposit ternary Al–Si–N coatings for scratch resistant optical coatings is thus motivated, and it will be the aim of the authors to pursue this further.

## Acknowledgements

The authors wish to acknowledge the financial support of COST through the short time scientific mission MP0804 7410 and the Swedish research council (VR ref. no. 623-2010-604).

## References

[1] A. Pélisson, M. Parlinska-Wojtan, H.J. Hug, J. Patscheider, Surf. Coat. Technol. 202 (4–7) (2007) 884.
[2] A. Pélisson, PhD, Doctoral thesis, University of Basel, Basel, 2009, http://dx.doi.org/10.5451/unibas-004994875 (url: http://edoc.unibas.ch/diss/DissB_8830).
[3] A. Mazel, P. Marti, F. Henry, B. Armas, R. Bonnet, M. Loubradou, Thin Solid Films 304 (1–2) (1997) 256.
[4] A. Pélisson-Schecker, H.J. Hug, J. Patscheider, Surf. Interface Anal. 44 (1) (2012) 29.
[5] A. Pélisson-Schecker, H.J. Hug, J. Patscheider, J. Appl. Phys. 108 (2) (2010) 023508.
[6] C.A. Pignedoli, D. Passerone, H.J. Hug, A. Pélisson-Schecker, J. Patscheider, Appl. Phys. Lett. 96 (7) (2010) 071908.
[7] C.-L. Chang, C.-S. Huang, Thin Solid Films 519 (15) (2011) 4923.
[8] J. Musil, M. Šašek, P. Zeman, R. Čerstvý, D. Heřman, J.G. Han, V. Šatava, Surf. Coat. Technol. 202 (15) (2008) 3485.

[9] H. Liu, W. Tang, D. Hui, L. Hei, F. Lu, Thin Solid Films 517 (21) (2009) 5988.
[10] J.T. Gudmundsson, N. Brenning, D. Lundin, U. Helmersson, J. Vac. Sci. Technol. A Vac. Surf. Films 30 (3) (2012) 030801.
[11] K. Sarakinos, J. Alami, S. Konstantinidis, Surf. Coat. Technol. 204 (11) (2010) 1661.
[12] U. Helmersson, M. Lattemann, J. Bohlmark, A.P. Ehiasarian, J.T. Gudmundsson, Thin Solid Films 513 (1–2) (2006) 1.
[13] A.P. Ehiasarian, A. Vetushka, A. Hecimovic, S. Konstantinidis, J. Appl. Phys. 104 (8) (2008) 083305.
[14] A.P. Ehiasarian, A. Vetushka, Y.A. Gonzalvo, G. Safran, L. Szekely, P.B. Barna, J. Appl. Phys. 109 (10) (2011) 104314.
[15] G. Kamath, A.P. Ehiasarian, P.E. Hovsepian, IEEE Trans. Plasma Sci. 38 (11) (2010) 3062.
[16] Y.P. Purandare, A.P. Ehiasarian, M.M. Stack, P.E. Hovsepian, Surf. Coat. Technol. 204 (8) (2010) 1158.
[17] D. Rafaja, C. Wüstefeld, J. Kutzner, A.P. Ehiasarian, M. Síma, V. Klemm, D. Heger, J. Kortus, Z. Krist. 225 (12) (2010) 599.
[18] C. Ma, P. Briois, J. Böhlmark, F. Lapostolle, A. Billard, Ionics 14 (6) (2008) 471.
[19] G. Greczynski, J. Lu, M.P. Johansson, J. Jensen, I. Petrov, J.E. Greene, L. Hultman, Surf. Coat. Technol. 206 (19–20) (2012) 4202.
[20] G. Greczynski, J. Lu, M. Johansson, J. Jensen, I. Petrov, J.E. Greene, L. Hultman, Vacuum 86 (8) (2012) 1036.
[21] A. Guillaumot, F. Lapostolle, C. Dublanche-Tixier, J.C. Oliveira, A. Billard, C. Langlade, Vacuum 85 (2) (2010) 120.
[22] D. Depla, S. Mahieu, R. De Gryse, Thin Solid Films 517 (9) (2009) 2825.
[23] P.Y. Jouan, L. Le Brizoual, M. Ganciu, C. Cardinaud, S. Tricot, M. Djouadi, IEEE Trans. Plasma Sci. 38 (11) (2010) 3089.
[24] A.P. Ehiasarian, Y.A. Gonzalvo, T.D. Whitmore, Plasma Process. Polym. 4 (S1) (2007) S309.
[25] R. Swanepoel, J. Phys. E Sci. Instrum. 16 (12) (1983) 1214.
[26] Dirk Poelman, Philippe Frederic Smet, J. Phys. D Appl. Phys. 36 (15) (2003) 1850, http://dx.doi.org/10.1088/0022-3727/36/15/316.
[27] W. Nix, Metall. Mater. Trans. A 20 (11) (1989) 2217.
[28] W.C. Oliver, G.M. Pharr, J. Mater. Res. 7 (1992) 1564.
[29] G.G. Stoney, Proc. R. Soc. Lond. A 82 (553) (1909) 172.
[30] C.A. Klein, J. Appl. Phys. 88 (9) (2000) 5487.
[31] G.C.A.M. Janssen, M.M. Abdalla, F. van Keulen, B.R. Pujada, B. van Venrooy, Thin Solid Films 517 (6) (2009) 1858.
[32] S. Berg, T. Nyberg, Thin Solid Films 476 (2) (2005) 215.
[33] M. Samuelsson, D. Lundin, J. Jensen, M.A. Raadu, J.T. Gudmundsson, U. Helmersson, Surf. Coat. Technol. 205 (2) (2010) 591.
[34] M. Mišina, L.R. Shaginyan, M. Maček, P. Panjan, Surf. Coat. Technol. 142–144 (0) (2001) 348.
[35] J.F. Moulder, W.F. Stickle, P.E. Sobol, K.D. Bomben, Handbook of X-ray Photoelectron Spectroscopy, Physical Electronics, Inc., Eden Prairie, Minnesota, USA, 1995.
[36] H.F. McMurdie, M.C. Morris, E.H. Evans, B. Paretzkin, J.H.d. Groot, C.R. Hubbard, S.J. Carmel, Natl. Bur. Stand. (U. S.) Monogr. 25 (1975) 5, (section 12).
[37] G.F. Iriarte, F. Engelmark, I.V. Katardjiev, J. Mater. Res. 17 (06) (2002) 1469.
[38] M. Ishihara, S.J. Li, H. Yumoto, K. Akashi, Y. Ide, Thin Solid Films 316 (1–2) (1998) 152.
[39] M. Lattemann, U. Helmersson, J.E. Greene, Thin Solid Films 518 (21) (2010) 5978.
[40] P. Scardi, M. Leoni, R. Delhez, J. Appl. Crystallogr. 37 (2004) 381.
[41] J. Alami, K. Sarakinos, F. Uslu, M. Wuttig, J. Phys. D Appl. Phys. 42 (1) (2009) 015304, http://dx.doi.org/10.1088/0022-3727/42/1/015304.

## B.2 Effect of the degree of high power impulse magnetron sputtering utilisation on the structure and properties of TiN films

Thin Solid Films 562 (2014) 132–139

Contents lists available at ScienceDirect

Thin Solid Films

journal homepage: www.elsevier.com/locate/tsf

# Effect of the degree of high power impulse magnetron sputtering utilisation on the structure and properties of TiN films

Papken Eh. Hovsepian, Arunprabhu A. Sugumaran *, Yashodhan Purandare, Daniel A.L. Loch, Arutiun P. Ehiasarian

*Nanotechnology Centre for PVD Research, Materials and Engineering Research Institute, Sheffield Hallam University, City Campus, Howard Street, Sheffield S1 1WB, United Kingdom*

ARTICLE INFO

*Article history:*
Received 16 October 2013
Received in revised form 25 March 2014
Accepted 2 April 2014
Available online 12 April 2014

*Keywords:*
High power impulse magnetron sputtering
Titanium nitride
Optical emission spectroscopy
Microstructure
Texture
Residual stress

ABSTRACT

TiN films were deposited using high power impulse magnetron sputtering (HIPIMS) enabled four cathode industrial size coating system equipped with HIPIMS power supplies. The standard version of this system allows control over the ion bombardment during coating growth by varying the strength of the electromagnetic field of the unbalancing coils and bias voltage applied to the substrate. The coatings were produced in different coating growth conditions achieved in combined HIPIMS – direct current (dc) unbalanced magnetron sputtering (HIPIMS/UBM) processes where HIPIMS was used as an additional tool to manipulate the ionisation degree in the plasma. Four cathode combinations were explored with increasing contribution of HIPIMS namely 4UBM (pure UBM), 1HIPIMS + 3UBM, 2HIPIMS + 2UBM and 2HIPIMS (pure HIPIMS) to deposit TiN coatings. Optical emission spectroscopy (OES) measurements were carried out to examine the plasma generated by the various combinations of HIPIMS and UBM cathodes. The micro-structural study was done by scanning electron microscopy (SEM). X-ray diffraction (XRD) technique was used to calculate the residual stress and texture parameter. It has been revealed that the residual stress can be controlled in a wide range from −0.22 GPa to −11.67 GPa by intelligent selection of the degree of HIPIMS utilisation, strength of the electromagnetic field of the unbalancing coils and the bias voltage applied to the substrate while maintaining the stoichiometry of the coatings. The effect of the degree of HIPIMS utilisation on the microstructure, texture and residual stress is discussed. Combining HIPIMS with dc-UBM sputtering is also seen as an effective tool for improving the productivity of the deposition process.



## 1. Introduction

High power impulse magnetron sputtering (HIPIMS) is a fast developing technology, which utilises extremely high power impulses (short pulses) to ionise the sputtered metal atom flux. It is characterised with power densities of about 3 kW $cm^{-2}$ and current densities of about 2 A $cm^{-2}$ applied at low duty cycle of <0.25% [1]. Each power impulse undergoes a cycle of breakdown-ignition, gas sputtering and self-sputtering and produces highly dense plasma of the order of $10^{13}$ $cm^{-3}$. This has the effect of ionising and activating reactive and inert gases in the plasma while sputtered metal atoms traversing the plasma are ionised with a high probability and charge states of $2^+$ or higher are observed for many target materials. The resulting deposition flux is rich in metal ions and highly activated gas ions which results in $Me^+/Me^0$ (metal ion to metal neutral) and $G^+/Me^+$ (gas ion to metal ion) ratios of 1 near the substrate. The mean energy of metal and gas ions of approximately 6 eV is factor 3 greater than in conventional sputtering in the same conditions [2]. The high ion-to-neutral ratios, high degree of metal ionisation and gas activation in the deposition flux are prerequisites for the build-up of a dense microstructure and specific preferred orientation of the coatings. Thus HIPIMS coatings have improved wear, corrosion and oxidation resistance. Oxide coatings have improved optical and electrical properties [3]. The HIPIMS has also been used for pre-treatment of the substrate prior to coating deposition to improve adhesion by intensive sputter-cleaning of impurities and metal ion implantation [1,4]. Extensive reviews on the sputter-cleaning process and technology can be found in the literatures [3,5].

However, one of the drawbacks of HIPIMS is the lower deposition rate when compared to the conventional magnetron sputtering. Major contribution to the reduction is the back attraction of the positively charged metal ions to the cathode, an effect observed and described already with the arc discharges [6]. One way to improve the deposition rate is to use lower strength magnetic fields, for example lower than 40 mT as suggested in [7], which reduces the magnetic confinement of the plasma and allows more positive ions to reach the substrate. Following this approach, deposition rates reaching 90% of the deposition rate of the conventional magnetron sputtering were achieved for Nb

* Corresponding author. Tel.: +44 114 225 4081; fax: +44 114 225 3501.
*E-mail address:* Arunprabhu.ArunachalamSugumaran@student.shu.ac.uk (A.A. Sugumaran).

http://dx.doi.org/10.1016/j.tsf.2014.04.002
0040-6090/

and other metals [7,8]. With deposition systems equipped with multiple and different plasma sources however, there is a possibility to run combined processes where only parts of the sources are operated in HIPIMS mode. A schematic cross section of a Hauzer system equipped with one HIPIMS source and three conventional unbalanced magnetrons was published already in 2004, soon after the upscaling of the HIPIMS technology [9]. In such configuration HIPIMS was made available to be used for surface pre-treatment to enhance the coating-substrate adhesion and also to deposit the coatings, either as a single source or in combination with the standard unbalanced magnetrons with improved microstructure due to the higher ionisation of the sputtered material. Indeed, highly dense TiN coatings with excellent mechanical properties deposited by HIPIMS can be seen elsewhere in the literature [10,11,12]. Nanoscale multilayer coatings of CrN/NbN with enhanced wear and corrosion resistance [13], CrN/TiN with improved wear resistance [14] and CrAlYN/CrN with improved high temperature oxidation resistance [15] were produced by the combined HIPIMS and conventional direct current (dc)-unbalanced magnetron (UBM) sputtering technology. The performance enhancement of the above said coatings was attributed to the fully dense microstructure with reduced multilayer waviness and sharp interfaces resulting from the higher ad atom mobility (energy) of the condensing species provided by HIPIMS.

Furthermore, the penalty due to the lower deposition rate of HIPIMS is expected to be significantly reduced with combined HIPIMS/UBM sputtering. However, the contribution, the extent of the HIPIMS utilisation in such combined processes, needs to be well understood and carefully considered. The answer to the question: "how much HIPIMS is needed in the process for the production of high quality coating" is not straightforward. The answer to this question has implications also on the physical vapour deposition (PVD) system manufacturers as well as HIPIMS power supply manufacturers who shall consider the design and the specifications of the next generation of systems enabled to deliver the combined technology.

The aim of this research is to shed more light on the effect of combining HIPIMS with UBM sputtering in one process by studying the ionisation degree in the plasma, coating microstructure and the deposition rate. TiN has been chosen as a model coating, which presents a simpler case to study the above mentioned effects in the HIPIMS/UBM combination. The authors however, believe that the conclusions of this study will be transferable to other more sophisticated coatings too.

## 2. Experimental details

### 2.1. Deposition of TiN coatings

TiN coatings were deposited in an industrial size PVD coating machine (chamber volume – 1 $m^3$, HAUZER 1000 – 4 HTC, Hauzer Techno Coating, The Netherlands) enabled with HIPIMS technology at Sheffield Hallam University. The original system was equipped with four dc-unbalanced magnetrons with target area of 1200 $cm^2$ each. In the modified version of the HTC 1000 – 4 system, two of the magnetrons were connected to HIPIMS power supplies allowing operation selectively either in UBM or in HIPIMS mode (Fig. 1). The HMP2/1 generators manufactured by Hüttinger Electronic Sp. z o.o., Poland were used to energise the HIPIMS magnetrons. The power supply was capable of supplying power pulses with duration in the range 0–200 μs at a frequency of 0–100 Hz (10 ms) equivalent to a duty cycle of 2%. It was capable of delivering peak currents of up to 3000 A and at a voltage of 2000 V. In this study, the HIPIMS power supplies were operated in a non-synchronised mode. Arcing energy was minimised by arc suppression design that allowed switch off of the power supply in the event of maximum current. The unbalancing effect was achieved by external magnetic field generated by electromagnetic coils surrounding the cathodes which were arranged in such a way to achieve close field magnetic configuration. Schematic cross section of the vacuum chamber is shown in Fig. 1. All cathodes were furnished with 99.99% pure Ti targets manufactured by GfE, Germany. The coatings were deposited on mirror polished (1 μm diamond paste) 30 mm diameter, 6 mm thick coupons from hardened M2 high-speed steel (HRC 62), 25 × 25 × 0.2 mm, bright annealed 304 stainless steel coupons and 20 × 10 × 0.2 mm, silicon wafer samples. Prior to the deposition, the substrates were cleaned in an automated cleaning line comprising a series of alkali solutions and de-ionised water baths. Subsequently, they were subjected to vacuum drying. The base pressure for all the coatings was 0.006 Pa. Four different cathode combinations were exploited as follows: 4 cathodes in conventional dc-UBM mode to deposit pure UBM coating, 1HIPIMS + 3UBM and 2HIPIMS + 2UBM cathodes to deposit combined HIPIMS/UBM coatings and 2HIPIMS cathodes to deposit pure HIPIMS coatings. During the conventional UBM sputtering the targets were operated with average power density of about 0.006 kW $cm^{-2}$ whereas high peak power density of about 0.180 kW $cm^{-2}$ was applied during HIPIMS, which results in equal average power in the range of 7–9 kW applied on all the four magnetrons.

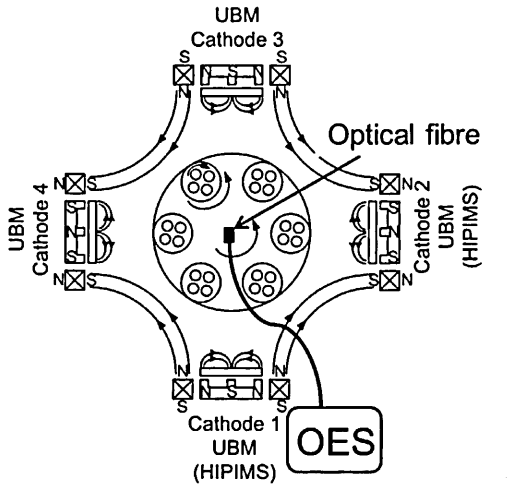


**Fig. 1.** Schematic of industrial size sputtering machine equipped with HIPIMS/UBM sources and optical emission spectrometer setup.

The substrate pre-treatment was done by bombarding the substrate with highly ionised mixture of $Ti^+/Ar^+$ plasma generated from a HIPIMS discharge maintained on the Ti target in an Ar atmosphere. Fundamentals and technical details of the metal ion etching procedure using HIPIMS are given in the literature [1,2,5]. The coating deposition was carried out in a reactive $Ar^+N_2$ atmosphere at 400 °C. To maintain a stable bias voltage in both surface pre-treatment and coating deposition processes, a specialised HIPIMS compatible bias power supply model HBP (Hüttinger Electronic Sp. z o.o.) was used [16].

### 2.2. Characterisation techniques

Various surface analysis techniques were employed to characterise the microstructure, texture and residual stress in the coatings. Optical emission spectroscopy (OES) measurements have been done to analyse the plasma in order to examine the influence of various combinations of HIPIMS and UBM plasma generation. OES spectra of TiN plasma were recorded by HORIBA Jobin Ivon Triax 320 monochromator with quartz optical fibre and collimator in time-averaged mode in vacuo. The quartz fibre capable of transmitting in the ultraviolet spectral region was kept in the substrate region during the measurements to analyse the plasma

**Table 1**
List of emission lines used.

| Species | Oscillator strength ($f_{ik}$) | Wavelength (nm) | Upper excitation energy (eV) | Lower excitation energy (eV) |
|---|---|---|---|---|
| $Ti^{1+}$ | 0.0035 | 367.968 | 4.05 | 1.58 |
| $Ti^0$ | 0.0053 | 364.6196 | 3.4 | 0 |
| $Ar^0$ | 0.24 | 763.511 | 13.2 | 12.3 |
| $N_2^0$ $C^3\prod_u$–$B^3\prod_g$; (0–2)[a] | – | 380.49 | 11.18 | 7.92 |
| $N_2^{1+}$ $B^2\Sigma_u^+$–$X^2\Sigma_g^+$; (0–0)[a] | – | 391.4 | 3.31 | 0.14 |

[a] Spectroscopic notation of the excited and ground state energy bands of $N_2^0$ and $N_2^{1+}$ species.

near the substrate as illustrated in Fig. 1. The orifice of the quartz fibre was facing downward to be able to see the mixed plasma and not only certain target areas as targets were on opposing sides. Table 1 lists the emission lines used in this study. The chosen Ti species lines have similar wavelengths, similar upper excitation energies and similar oscillator strengths. Further the Ti neutral is a transition to the ground sate. Considering the intensity ratio of these lines is ideal for a qualitative statement on the effect of HIPIMS utilisation on the ionisation of metal. The intensity ratios of $Ti^{1+}$, $Ar^0$ and $N_2^0$ to intensity ratios of all Ti species ($Ti^{1+} + Ti^0$) in the plasma are considered to extract information about the 'weighted emission intensity' of $Ti^{1+}$, $Ar^0$ and $N_2^0$. To improve the accuracy of the estimates, the oscillator strengths for $Ti^0$, $Ar^0$ and $Ti^{1+}$ were used in the calculation, assuming that the line intensity $I \sim f_{ik} * n$, where $f_{ik}$ is the oscillator strength and n is the density of species. The following relations were used to estimate the 'weighted emission intensity' of $Ti^{1+}$, $Ar^0$ and $N_2^0$.

$$\left\{Ti^{1+}\right\} = \frac{\frac{Ti^{1+}}{f_{ik}^{Ti^{1+}}}}{\left(\frac{Ti^{1+}}{f_{ik}^{Ti^{1+}}} + \frac{Ti^0}{f_{ik}^{Ti^0}}\right)} \quad (1)$$

$$\left\{Ar^0\right\} = \frac{\frac{Ar^0}{f_{ik}^{Ar^0}}}{\left(\frac{Ti^{1+}}{f_{ik}^{Ti^{1+}}} + \frac{Ti^0}{f_{ik}^{Ti^0}}\right)} \quad (2)$$

$$\left\{N_2^0\right\} = \frac{N_2^0}{\left(\frac{Ti^{1+}}{f_{ik}^{Ti^{1+}}} + \frac{Ti^0}{f_{ik}^{Ti^0}}\right)} \quad (3)$$

where $Ti^{1+}$, $Ti^0$, $Ar^0$ and $N_2^0$ are the emission line intensities of $Ti^{1+}$ ions, $Ti^0$ neutrals, $Ar^0$ neutrals and $N_2^0$ neutrals respectively. $f_{ik}^{Ar^0}$, $f_{ik}^{Ti^0}$ and $f_{ik}^{Ti^{1+}}$ are the oscillator strengths of $Ar^0$, $Ti^0$ and $Ti^{1+}$ respectively. Due to the use of oscillator strength, the 'weighted emission intensity' is proportional to the density of species in the plasma. However, the coefficient of proportionality could not be measured. Therefore the 'weighted emission intensity' is only a qualitative measure of the density of species. The excitation energies for Ar and $N_2$ are significantly higher than $Ti^0$ and $Ti^{1+}$ and as such the ratios are dependent on the electron temperature. Calculating these ratios for $N_2^{1+}$ which has similar excitation energy as $Ti^0$ and $Ti^{1+}$ yielded similar trends as the ones observed for $N_2^0$ (not shown). This was confirmed when changing the deposition process, unbalancing coil current and nitrogen flow. This indicates that the main effect observed was that of the change in density and the influence of electron temperature is secondary.

X-ray diffraction (XRD) technique was utilised (Philips X'Pert MPD) for the texture, T* (Bragg–Brentano, BB) and stress, σ (glancing angle (GA) geometry) calculations. Texture coefficient (T*) was calculated using the following equation [17]:

$$T* = \left[I_{(hkl)}/R_{(hkl)}\right] / \left[\left(n^{-1}\sum{}^0{}_n I_{(hkl)}/R_{(hkl)}\right)\right] \quad (4)$$

where $I_{(hkl)}$ and $R_{(hkl)}$ are the intensities from the (hkl) reflections in the specimen and a random powder respectively and n is the number of reflections considered. The residual stress was determined by X-ray omega diffractometer using $\sin^2\Psi$ method [17]. Stress (σ) was calculated from the slope of the least-squares fit of the plot of $a_\Psi$ versus $\sin^2\Psi$ and using the following expression [17]:

$$\sigma = (\text{Slope E})/[a_0(1+\nu)]. \quad (5)$$

Stress dependence of the lattice parameter $a_\Psi$ related by the following equation [17]:

$$a_\Psi = \sigma a_0\left(\frac{1+\nu}{E}\sin^2\Psi - \frac{2\nu}{E}\right) + a_0 \quad (6)$$

where $\Psi = \theta - \gamma$ (Bragg angle (θ) − angle of incidence (γ) of the X-ray beam relative to the specimen surface), $a_0$ is the unstressed lattice parameter, E is the elastic modulus determined in this study by nano-indentation test and ν is the Poisson's ratio (in this study = 0.3). A nano hardness tester (CSM Instruments SA) with a Berkovich indenter was used to evaluate the elastic modulus using Oliver and Pharr method. The applied load for all of the elastic modulus measurements was 10 mN. A scanning electron microscope (FEI NOVA-NanoSEM 200) was used for microstructure imaging and thickness measurements. TiN coated silicon fracture was used for this purpose. Surface roughness measurement of the coatings was done using a profilometer. The energy dispersive X-ray spectroscopy (EDX) analysis of the films has been carried out using a scanning electron microscope (FEI NOVA-NanoSEM 200) equipped with an EDX detector. Stoichiometric TiN film deposited by chemical vapour deposition (CVD) and characterised by Rutherford back scattering (RBS) techniques was used to calibrate the EDX module.

## 3. Results and discussion

### 3.1. OES measurements

#### 3.1.1. Effect of different HIPIMS/UBM source combination

The effect of various HIPIMS/UBM source combinations on $\{Ti^{1+}\}$ and $\{N_2^0\}$ is illustrated in Fig. 2. All the measurements were carried out with coil current ($I_{coil}$): 3 A, bias voltage ($U_b$): 0 V and working pressure: 0.3 Pa.

The $\{Ti^{1+}\}$ starts at a low value of 0.13 for the pure UBM process and rises continuously as more HIPIMS cathodes are energised; reaching a maximum of 0.75 for the pure HIPIMS process. This increase is related to the increased production of $Ti^{1+}$ ions in the high peak power HIPIMS process. The pure HIPIMS process generates a factor of ~7.5 higher metal ionisation ratio than the pure UBM process.

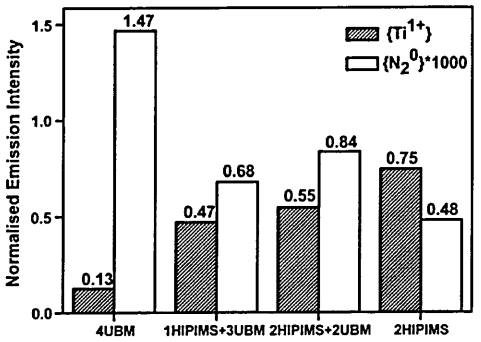


Fig. 2. $\{Ti^{1+}\}$ and $\{N_2^0\}$ calculated by using the respective intensity ratios as a function of source combination. $\{N_2^0\}$ is multiplied by 1000 for better visibility.

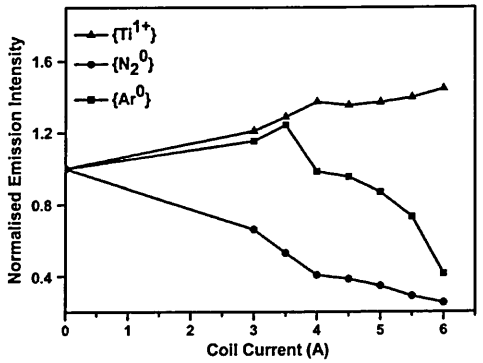


Fig. 3. Effect of coil current on $\{Ti^{1+}\}$, $\{N_2^0\}$ and $\{Ar^0\}$. Normalisation factor for $\{Ti^{1+}\}$, $\{N_2^0\}$ and $\{Ar^0\}$ was 1.83, 1197.65 and 55.92 respectively.

The $\{N_2^0\}$ is high for the pure UBM process and reduces when HIPIMS is involved. Emission from $N_2^{1+}$ at 391.4 nm (not shown) was observed to follow the trend for $N_2^0$. The amount of nitrogen in the working atmosphere was constant given that the partial pressure of $N_2$ was controlled to be constant and the resulting variation in flow rates was <10% between all cases. Additionally, according to the EDX studies (not shown), the film composition was similar (stoichiometric) within the error of the measurement. Combining these and the plasma observations, we deduce that the lower $\{N_2^0\}$ in the plasma could be attributed to ionisation and subsequent dissociation of the molecular gas due to the HIPIMS process generating high density of electrons that are responsible for the above processes [18]. Such observations are consistent with studies of discharge composition found in pure HIPIMS sputtering of Ti in Ar and $N_2$ atmosphere [2], where the content of dissociated nitrogen ions was found to be higher than that of molecular nitrogen. In summary, the implementation of HIPIMS in this process has led to highly activated conditions of deposition, in particular dissociation of nitrogen and ionisation of Ti. In principle these results show that all the combinations where HIPIMS is involved such as 1HIPIMS + 3UBM, 2HIPIMS + 2UBM and 2HIPIMS provide favourable conditions for depositing films with stoichiometric composition. Therefore the optimum combination of sources should be selected accounting also for the effect on coating microstructure and compressive stress.

*3.1.2. Effect of unbalancing and closed field confinement*

In order to illustrate the effect of unbalancing coil current on the chemistry of the ion flux generated, the 2HIPIMS + 2UBM cathode combination has been considered. This combination appears to be the best one in this research as it provides a large bias voltage range where relatively low stress highly dense coatings can be produced as explained in Sections 3.3 and 3.5. The degree of magnetic unbalancing of the cathode and the strength of closed field confinement in the system were varied using the electromagnetic coil current. In this system the coil current increases the degree of magnetic unbalancing of the magnetron and increases the closed field confinement whilst reducing the width of the race track. The bias voltage ($U_b$) and working pressure were 0 V and 0.3 Pa respectively during these measurements.

Fig. 3 shows $\{Ar^0\}$, $\{N_2^0\}$ and $\{Ti^{1+}\}$ in relation to the applied coil current. The $\{Ar^0\}$ rises for coil currents up to 3.5 A. This can be attributed to the increase of the effective excitation volume for argon (Ar) due to an enhanced electron transport away from the cathode. For coil currents of 4–6 A, the $Ar^0$ ratio reduces significantly. This may be caused by increasing ionisation of Ar and rarefaction due to narrowing of the racetrack and the resulting increase in power density. The $\{Ti^{1+}\}$ also increases with increasing coil current. The $\{N_2^0\}$ decreases monotonically with coil current. This behaviour may be due to prevalent dissociation (see Section 3.1.1) rather than excitation processes for nitrogen, which in this case is fuelled by a local enhancement of plasma density near the target on account of reduced racetrack width and target power density. In comparison, Ar has a smaller ionisation cross section that requires higher plasma density to shift the balance from excitation to ionisation and the shift in balance and corresponding drop in intensity is only observed for coil currents above 4 A.

*3.1.3. Effect of target poisoning*

OES measurements with increasing nitrogen flow from 0 to 180 sccm (total pressure from 0.24 Pa to 0.36 Pa) were done to understand the effect of target poisoning with 2HIPIMS + 2UBM cathode combination. The bias voltage ($U_b$) and coil current ($I_{coil}$) were kept at 0 V and 3 A respectively during these measurements.

Fig. 4 shows peak discharge current, $Ti^0$, $Ti^{1+}$ intensities and $\{Ti^{1+}\}$ and $\{N_2^0\}$ as a function of $N_2$ flow. The trend is very similar to the classical poisoning case observed for magnetron sputtering (reduction of the amount of metallic species with increasing reactive gas flow rate). It was found that the intensity of $Ti^0$ and $Ti^{1+}$ decreases rapidly with increasing $N_2$ flow, which can be attributed to the development of the target poisoning effect. It is well understood that during reactive sputtering a thin layer of TiN is formed due to the chemisorption or physisorption of neutral $N_2$ molecules on the target and the target bombardment by molecular or atomic nitrogen ions. As a consequence, the deposition rate of TiN (not shown in Fig. 5) will reduce with increasing nitrogen flow rate. $Ti^0$ and $Ti^{1+}$ emission intensities are diminished due to lower sputtering yield of TiN and the involvement of more nitrogen ions in the sputtering process compared to the non-reactive sputtering case where Ar ions are used [19]. The effective gas ionisation rate is increased as observed from the increase in the peak discharge current [Fig. 4]. The increase in current may be attributed partially to the enhanced probability of ionisation of the process gas through the addition of $N_2$ which has a higher collisional cross section than Ar and Ti. As Magnus et al. [20] point out, $N^{1+}$ ions may play an important role in being able to extract secondary electrons from a TiN-covered target surface along with $Ar^{1+}$, $N_2^{1+}$ and $Ti^{2+}$. The rich variety of reaction pathways for $N_2$ predispose the production of high fluxes of $N^{1+}$ ions detected near the substrate [2], indicating an extensive build up of $N^{1+}$ ions in the dense plasma region near the target as well. Increasing $N_2$ partial pressure would increase the probability of collisions thus producing $N^{1+}$ at higher rate even though the electron temperature is reduced as observed from Ti line ratios (not shown). Thus it appears that in HIPIMS, the creation of an additional ion that is able to induce secondary emission outweighs the reduction of the secondary emission

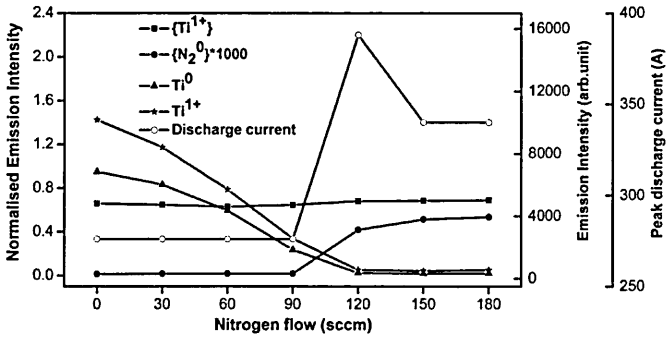


Fig. 4. Effect of $N_2$ flow on peak discharge current, $\{Ti^{1+}\}$, $\{N_2^0\}$ and $\{Ar^0\}$ and emission intensity of $Ti^{1+}$ & $Ti^0$ species. $\{N_2^0\}$ is multiplied by 1000 for better visibility.

yield that results from covering a Ti target surface with a TiN compound during poisoning. Above 120 sccm of $N_2$ flow, the target poisoning is complete and the intensities of $Ti^0$ and $Ti^{1+}$ are constant. The $\{N_2^0\}$ is below the detection limit for nitrogen flows up to 90 sccm as the nitrogen is completely absorbed while reacting with titanium. For flows between 90 and 120 sccm, the $\{N_2^0\}$ rises sharply, as excess nitrogen is introduced. The $\{Ti^{1+}\}$ remains stable for all nitrogen flows in both poisoned and sub-stoichiometric regimes due to the constant peak power. A small reduction near the stoichiometric point can be attributed to fluctuations in peak power near the point where metal-rich plasma is replaced by gas-rich plasma.

### 3.2. Effect of HIPIMS utilisation on deposition rate

The TiN coatings deposited on silicon substrate were used for the thickness measurements. The coated silicon samples were fractured and investigated under a scanning electron microscope. All the HIPIMS/UBM combined processes were carried out with bias voltage ($U_b$) − 50 V, coil current ($I_{coil}$) − 3 A and working pressure − 0.3 Pa. For pure UBM coating, bias voltage ($U_b$), coil current ($I_{coil}$) and working pressure were − 75 V, 6 A and 0.3 Pa respectively. The deposition time was 4 h for all the coatings. Fig. 5 shows the TiN coating thickness as a function of the degree of HIPIMS utilisation. For completeness, a 4HIPIMS case derived by extrapolating the results from the 2HIPIMS experiment is also added. Deposition rate loss due to increased HIPIMS utilisation is found to be 1.37% for 1HIPIMS + 3UBM, 13.7% for 2HIPIMS + 2UBM, 60.7% for 2HIPIMS (due to the reduced number of targets) and only 21.3% for 4HIPIMS (extrapolated value). These experiments clearly demonstrate that combined HIPIMS + UBM processes bear a high potential for improved productivity. Furthermore, if followed, this approach might lead to a reasonable reduction of hardware costs as high quality coatings could be produced with smaller number of HIPIMS sources involved in the process provided that they deliver the necessary high plasma ionisation.

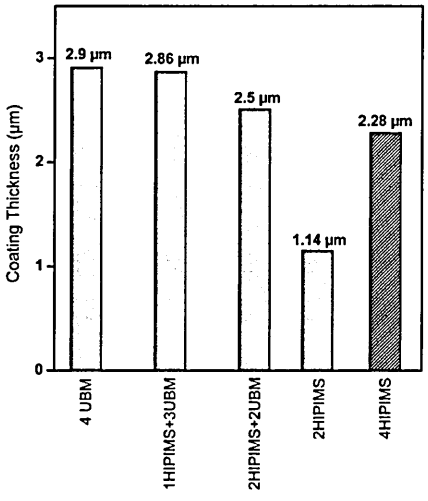


Fig. 5. Coating thickness as a function of source combination: Pure UBM, 1HIPIMS + 3UBM, 2HIPIMS + 2UBM, 2HIPIMS, 4HIPIMS (extrapolated result). Deposition time − 4 h.

### 3.3. Microstructure analysis

Cross-sectional SEM studies were carried out on TiN coatings deposited on Si substrates with various HIPIMS/UBM combinations to reveal the coating microstructure. These experiments were done to demonstrate the microstructure 'structural densification' achieved by the incorporation of HIPIMS in the process. Therefore coatings deposited with different combinations of bias voltage, coil current and working pressure are considered and listed in Table 2. The average surface roughness ($R_a$) values of the coatings are listed in Table 3.

Fig. 6(a–e) shows SEM cross section images of TiN coatings deposited with various HIPIMS/UBM cathode combinations with different process parameters. The microstructure was columnar for all the coatings but with distinct differences as the HIPIMS contribution in the process increased. Coarse microstructure with pronounced open column boundaries and rough coating top surface was observed for both the pure UBM [Fig. 6(a)] and the UBM dominated 1HIPIMS + 3UBM coatings [Fig. 6(b)] which is a clear indication for insufficient ion bombardment leading to inter-columnar fracture mechanism. The lower $\{Ti^{1+}\}$ [0.13 and 0.47] in the plasma as shown by the OES measurements for both the cases supports this claim. The $R_a$ for pure UBM and 1HIPIMS + 3UBM coatings was 0.05 µm and 0.043 µm respectively. It is interesting to note that in the case of 1HIPIMS + 3UBM, even for a small reduction in the bias voltage and coil current from $U_b = -75$ V to $U_b = -50$ V and $I_{coil} = 3$ A to $I_{coil} = 0$ A respectively, the structure of 1HIPIMS + 3UBM, shown in Fig. 6(b) converts to fully open highly under dense structure with sharp column tops [Fig. 6(e)] which resembles the structure of pure UBM coating deposited at floating potential [21]. One can conclude that when HIPIMS is strongly "diluted" in UBM or operated in "weak" ionisation conditions it will produce inferior structures and therefore inferior performance. Of course the structure in such cases can be densified by applying higher bias voltages which however, is at the expense of increased compressive stress in the coating.

**Table 2**
List of experiments considered to demonstrate microstructure evolution.

| Fig. no. | Source combination | Bias voltage ($U_b$) (V) | Coil current ($I_{coil}$) (A) | Working pressure (Pa) |
|---|---|---|---|---|
| 6(a) | 4UBM | −75 | 6 | 0.33 |
| 6(b) | 1HIPIMS + 3UBM | −75 | 3 | 0.30 |
| 6(c) | 2HIPIMS + 2UBM | −50 | 3 | 0.30 |
| 6(d) | 2HIPIMS | −50 | 3 | 0.30 |
| 6(e) | 1HIPIMS + 3UBM | −50 | 0 | 0.30 |

In contrast when HIPIMS or HIPIMS/UBM combinations maintaining conditions of sufficiently high metal ionisation [{$Ti^{1+}$} for 2HIPIMS + 2UBM & pure HIPIMS: 0.55 & 0.75 respectively] are used, highly dense and very smooth coatings are produced [Fig. 6(c & d)]. The fracture morphology is smooth, glassier, with column width increasing with HIPIMS contribution in the deposition process. The $R_a$ for 2HIPIMS + 2UBM and pure HIPIMS coatings was 0.04 μm and 0.037 respectively. The low $R_a$ values 2HIPIMS + 2UBM and pure HIPIMS coatings confirm that these coatings are relatively smoother compared to pure UBM and 1HIPIMS + 3UBM coatings. The wide columnar structure with very smooth column tops as in Fig. 6(d) was first described for HIPIMS deposited CrN and explained by the high ad atom mobility and re-sputtering effect due to the high metal ion fracture and energy in the condensing flux [22]. The glassy morphology is believed to form via trans-columnar fracture mechanism, which results from the equal strength of the material at the column boundaries and within the column. Previous research using atomic resolution TEM has shown that HIPIMS can produce TiN coatings with almost bulk material density with atomically tight grain boundaries and columns bonded on atomic level thus creating the "equal strength" structure [2].

### 3.4. Texture evolution

The texture evolution of different combined HIPIMS/UBM TiN coatings analysed by X-ray diffraction (θ–2θ, BB geometry) is shown in Fig. 7. For 1HIPIMS + 3UBM, 2HIPIMS + 2UBM and pure HIPIMS combinations, the working pressure was 0.3 Pa and the coil current was 3 A. It was found that the 1HIPIMS + 3UBM coating exhibited strong [111] texture which switched to strong [200] with increasing number of HIPIMS cathodes involved in the process. Many studies have shown that the most important parameters defining nitride coating texture are molecular or atomic nitrogen, ionised or neutral metal species and the ion-to neutral flux ratio [2,23,24]. For HIPIMS-deposited TiN it was demonstrated that increase of the peak discharge current above a specific threshold value produced a texture switch from (111) to (200) due to increased amount of atomic nitrogen and $Ti^{1+}$ ions [18].

According to Ehiasarian et al. [2] (111) oriented grain growth is promoted when mostly Ti atoms and $N_2$ molecules are involved in the deposition process which is evident from 1HIPIMS + 3UBM process in this study. Moreover (200) oriented grain growth is promoted under deposition conditions in which the incident particles are primarily $Ti^{1+}$ ions and atomic nitrogen typical for the pure HIPIMS process. It has been shown that HIPIMS plasmas were found to be a highly efficient source of atomic nitrogen and metal ions capable of producing fluxes with $N^{1+}$: $N_2^{1+}$ >1 and $Ti^{1+}$: $Ti^0$ >1 [2]. Thus this study revealed that the texture can be manipulated by the amount of HIPIMS utilisation in the process as this changes the plasma chemistry and ionisation degree as shown by the OES analyses discussed in Section 3.1.1.

It is interesting to note that the switch in texture is observed at relatively low power densities of 0.180 kW $cm^{-2}$ compared to laboratory-scale HIPIMS studies [18] with 0.3 kW $cm^{-2}$. This could be attributed to the large plasma volume in industrial scale sources which is more efficient in dissociating the gas. The closed field configuration and unbalancing of the cathode are also responsible for enhancing the activation of plasma near the substrate. The exact correlation is subject to further studies. The results reported here however, are in a good agreement with those published elsewhere in the literature [2,11].

**Table 3**
Surface roughness of TiN coatings deposited by combined HIPIMS/UBM sources.

| Source combination | Average surface roughness (μm) |
|---|---|
| Pure UBM (4 UBM) | 0.05 |
| 1HIPIMS + 3UBM | 0.043 |
| 2HIPIMS + 2UBM | 0.04 |
| Pure HIPIMS (2HIPIMS) | 0.037 |

### 3.5. Residual stress measurement

Magnetron sputtered coatings experience compressive stress when deposited in conditions of high energy ion bombardment of the surface which creates lattice defects [25,26]. This is particularly critical and higher for HIPIMS due to higher energetics in this process [2,12]. GA XRD was done to calculate the compressive stress generated by high energy ion bombardment. The behaviour of the residual stress (σ) as a function of the substrate bias voltage was studied for the following three configurations: 1HIPIMS + 3UBM, 2HIPIMS + 2UBM and 2HIPIMS and the results are summarised in Fig. 8. For all the three source combinations the working pressure was 0.3 Pa and the coil current was 3 A for the 1HIPIMS + 3HIPIMS and 2HIPIMS + 2UBM combinations. It was 0 A in the case of 2HIPIMS (pure HIPIMS) coatings.

The advantage of HIPIMS compared to UBM is that the bombarding flux in HIPIMS is strongly dominated by metal ions. The presence of metal ions of the same descent as these of the condensing metal creates better conditions for recombination of the ion bombardment induced lattice defects, therefore lower stress, provided that the ion energy (bias voltage) stays below a material specific threshold limit. In contrast, when bombarding predominantly with gas ($Ar^{1+}$) ions as in the UBM case, the lattice defect density mainly increases with ion energy due to gas entrapment.

Analysis of the slope of the stress (σ)–bias voltage curves in Fig. 8 shows that the steepest slope is achieved by the 1HIPIMS + 3UBM process where the metal ion content in the plasma is the smallest. This is the worst scenario, as in this case mostly neutrals take part in the growth process bombarded mainly by gas ions, whereas the re-combination effect is not that pronounced due to the relatively small number of metal ions. This combination leads to a steep increase of stress with bias voltage. The very low stress, $\sigma = -0.22$ GPa measured for the coating deposited at low bias, ($U_b = -50$ V) is due to the formation of a very open columnar structure as shown in Fig. 6(e) where stress relaxation takes place during the coating growth via crack and voids formation mechanisms. Further details on the stress generation in PVD coatings can be found in Ref. [27]. The open columnar structure however, is not recommendable for practical applications. Therefore, for the 1HIPIMS + 3UBM combination, conditions leading to even lower

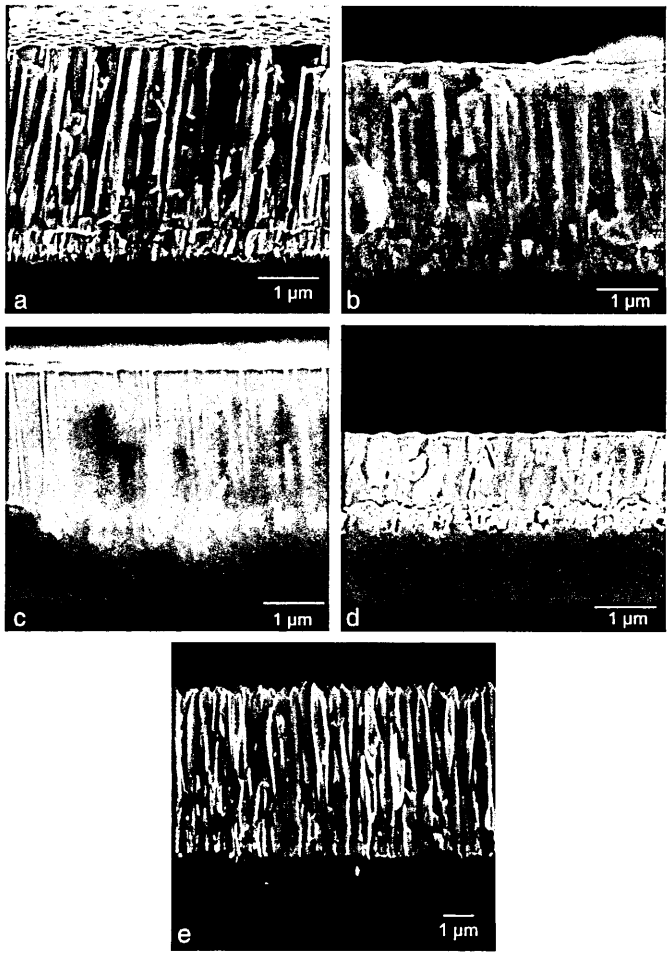


**Fig. 6.** Effect of bias voltage on the microstructure of TiN coatings deposited with different source combinations: (a) Pure UBM, $U_b = -75$ V, (b) 1HIPIMS + 3UBM, $U_b = -75$ V, (c) 2HIPIMS + 2UBM, $U_b = -50$ V, (d) Pure HIPIMS, $U_b = -50$ V, and (e) 1HIPIMS + 3UBM, $U_b = -50$ V.

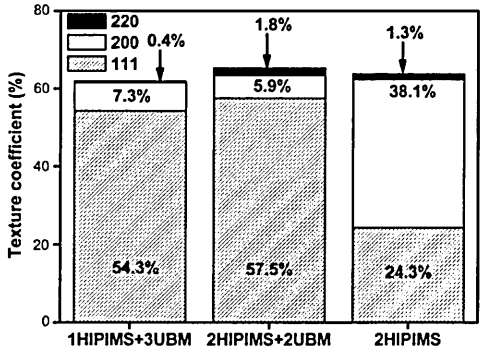


**Fig. 7.** Texture coefficient as a function of source combination.

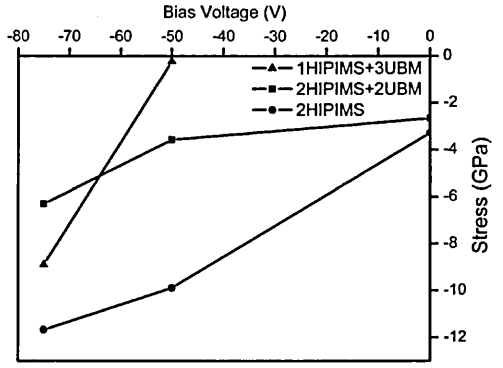


**Fig. 8.** Effect of bias voltage on the residual stress of TiN coatings deposited with different source combinations.

ion bombardment during coating growth as provided at 0 V bias voltage were not included in the experiment.

Fore pure HIPIMS coatings, the stress increases with bias voltage, however, at a lower rate compared to the 1HIPIMS + 3UBM process due to the presence of a large amount of film forming metal ions, as shown by the OES analysis in Section 3.1.1. Coatings with lower stress ($\sigma = -3.28$ GPa) can be deposited with this technique by applying lower bias voltages or even deposited at floating potential without deteriorating the coating structure.

The 2HIPIMS + 2UBM source combination appears to be the best one in this research as this provides a large bias voltage range where relatively low stress ($\sigma = -3.5$ GPa), highly dense, Fig. 6(c), coatings can be produced. This is believed to be due to the optimal $\{Ti^{1+}\}$, 0.55 achieved with the process. Furthermore the 2HIPIMS + 2UBM combination is advantageous as the large bias voltage window allows for better process and therefore better tuning of coating properties.

## 4. Conclusions

Combining high power impulse magnetron sputtering with dc-unbalanced magnetron sputtering in one deposition process in a multiple source deposition system such as Hauzer 1000/4 is an effective approach which allows manipulation of the ionisation degree in the plasma therefore widens the process window for coating structure, texture, residual stress and properties control. The OES measurements revealed that the $\{Ti^{1+}\}$ in the deposition flux was found to be increased with increasing number of HIPIMS sources involved in the process as follows: pure UBM: 0.13; 1HIPIMS + 3UBM: 0.47; 2HIPIMS + 2UBM: 0.55 and 2HIPIMS (pure HIPIMS): 0.75. This observation shows combined HIPIMS/UBM processes generate more metal ions than neutral metal atoms compared to pure UBM process. The thickness measurements by SEM showed that combining HIPIMS with UBM is seen as an effective tool for improving the productivity of the deposition process. Deposition rate losses due to utilisation of HIPIMS were found to be as follows: 1.37% for 1HIPIMS + 3UBM process; 13.7% for 2HIPIMS + 2UBM process and 21.3% for pure HIPIMS process when extrapolated to four HIPIMS sources. The residual stress in TiN coatings can be varied in a wide range from −0.22 GPa to −11.67 GPa and film texture can be altered from strong (111) to random to (200). High dense coatings can be produced by intelligent selection of the degree of HIPIMS utilisation, the strength of the electromagnetic field produced by the unbalancing coils of the machine as well as the bias voltage applied to the substrate. The combination of 2HIPIMS + 2UBM appears to be the most advantageous in this research as this provides a large bias voltage range where relatively low stress ($\sigma = -3.5$ GPa) and highly dense (Fig. 6c) coatings can be produced at reasonably high deposition rates. This is believed to be due to the optimal $\{Ti^{1+}\}$, 0.55 achieved with the process.

## References


[1] A.P. Ehiasarian, J.G. Wen, I. Petrov, Interface microstructure engineering by high power impulse magnetron sputtering for the enhancement of adhesion, J. Appl. Phys. 101 (5) (2007) 54301.

[2] A.P. Ehiasarian, A. Vetushka, Y. Aranda Gonazalvo, G. Safran, L. Szekely, P.B. Barna, Influence of high power impulse magnetron sputtering plasma ionization on the microstructure of TiN thin films, J. Appl. Phys. 109 (2011) 104314.

[3] A.P. Ehiasarian, in: R. Wei (Ed.), Plasma Surface Engineering Research and its Practical Applications, Research Signpost, Trivandrum, India, 2008, p. 35.

[4] W.-D. Münz, A.P. Ehiasarian, P.Eh. Hovsepian, EP20020011204, 21 May 2001.

[5] U. Helmersson, M. Lattemann, J. Bohlmark, A.P. Ehiasarian, J.T. Gudmundsson, Ionized physical vapor deposition (IPVD): a review of technology and applications, Thin Solid Films 13 (1–2) (2006) 1.

[6] J.M. Lafferty, Vacuum Arcs—Theory and Application, John Wiley & Sons, New York, 1980.

[7] A.P. Ehiasarian, HIPIMS With Low Magnetic Field Strength, GB2437730, 2006 May 02.

[8] W.-D. Münz, HIPIMS: The new PVD technology, Vak. Forsch. Prax. 20 (S1) (2008) 27.

[9] A.P. Ehiasarian, R. Bugyi, Industrial Size high power impulse magnetron sputtering, 47th SVC Annual Technical Conference Proceedings, USA, 24–29 April 2004, p. 486.

[10] J. Bohlmark, M. Lattemann, H. Stranning, T. Selinder, J. Carlsson, U. Helmersson, Reactive film growth of TiN by using high power impulse magnetron sputtering (HIPIMS), 49th SVC Annual Technical Conference Proceedings, USA, April 22-27 2006, p. 334.

[11] M. Lattemann, U. Helmersson, J.E. Greene, Fully dense, non-faceted 111-textured high power impulse magnetron sputtering TiN films grown in the absence of substrate heating and bias, Thin Solid Films 518 (2010) 5978.

[12] R. Machunze, A.P. Ehiasarian, F.D. Tichelaar, G.C.A.M. Janssen, Stress and texture in HIPIMS TiN thin films, Thin Solid Films 518 (2009) 1561.

[13] Y.P. Purandare, A.P. Ehiasarian, P.Eh. Hovsepian, Deposition of nanoscale multilayer CrN/NbN physical vapour deposition coatings by high power impulse magnetron sputtering, J. Vac. Sci. Technol. A 26 (2) (2008) 288.

[14] J. Paulitsch, P.H. Mayrhofer, W.-D. Münz, M. Schenkel, Structure and mechanical properties of CrN/TiN multilayer coatings prepared by a combined HIPIMS/UBMS deposition technique, Thin Solid Films 517 (3) (2008) 1239.

[15] P.Eh. Hovsepian, A.P. Ehiasarian, Y.P. Purandare, R. Braun, I.M. Ross, Effect of high ion irradiation on the structure, properties and high temperature tribology of nanoscale CrAlYN/CrN multilayer coating deposited by HIPIMS–HIPIMS technique, Plasma Process. Polym. 6 (S1) (2009) S118.

[16] A.P. Ehiasarian, R. Tietema, A. Klimczak, R. Bugyi, P. Eh. Hovsepian, D. Doerwald, GB0607269.8, 11 Apr. 2006.

[17] D.S. Rickerby, A.M. Jones, B.A. Bellamy, X-ray diffraction studies of physically vapour deposited coatings, Surf. Coat. Technol. 37 (1989) 111.

[18] A.P. Ehiasarian, A. Vetushka, A. Hecimovic, S. Konstantindis, Ion composition produced by high power impulse magnetron sputtering discharges near the substrate, J. Appl. Phys. 104 (2008) 083305.

[19] L. Combadiere, J. Machet, Study and control of both target-poisoning mechanisms and reactive phenomenon in reactive planar magnetron cathodic sputtering of TiN, Surf. Coat. Technol. 82 (1996) 145.

[20] F. Magnus, O.B. Sveinsson, S. Olafsson, J.T. Gudmundsson, Current–voltage–time characteristics of the reactive Ar/N2 high power impulse, J. Appl. Phys. 110 (2011) 083306.

[21] G. Håkanssan, J.E. Sundgren, D. McIntire, J.E. Greene, W.D. Münz, Microstructure and physical properties of polycrystalline metastable $Ti^{0.5}Al^{0.5}N$ alloys grown by d.c. magnetron sputter deposition, Thin Solid Films 153 (1987) 55.

[22] A.P. Ehiasarian, W.-D. Münz, L. Hultman, U. Helmersson, CrN deposition by reactive high-power density pulsed magnetron sputtering, 45th SVC Annual Technical Conference Proceedings, USA, April 13–18 2002, p. 328.

[23] D. Gall, S. Kodambaka, M.A. Wall, I. Petrov, J.E. Greene, Pathways of atomistic processes on TiN (001) and (111) surfaces during film growth: an ab initio study, J. Appl. Phys. 93 (2003) 9086.

[24] C.S. Shin, D. Gall, Y.W. Kim, N. Hellgren, I. Petrov, J.E. Greene, Development of preferred orientation in polycrystalline NaCl-structure δ-TaN layers grown by reactive magnetron sputtering: role of low-energy ion surface interactions, J. Appl. Phys. 92 (2002) 5084.

[25] J.A. Thornton, D.W. Hoffman, Stress-related effects in thin films, Thin Solid Films 171 (1989) 5.

[26] C.A. Davis, A simple model for the formation of compressive stress in thin films by ion bombardment, Thin Solid Films 226 (1993) 30.

[27] G.C.A.M. Janssen, J.-D. Kamminga, Stress in hard metal films, Appl. Phys. Lett. 85 (2004) 3086.